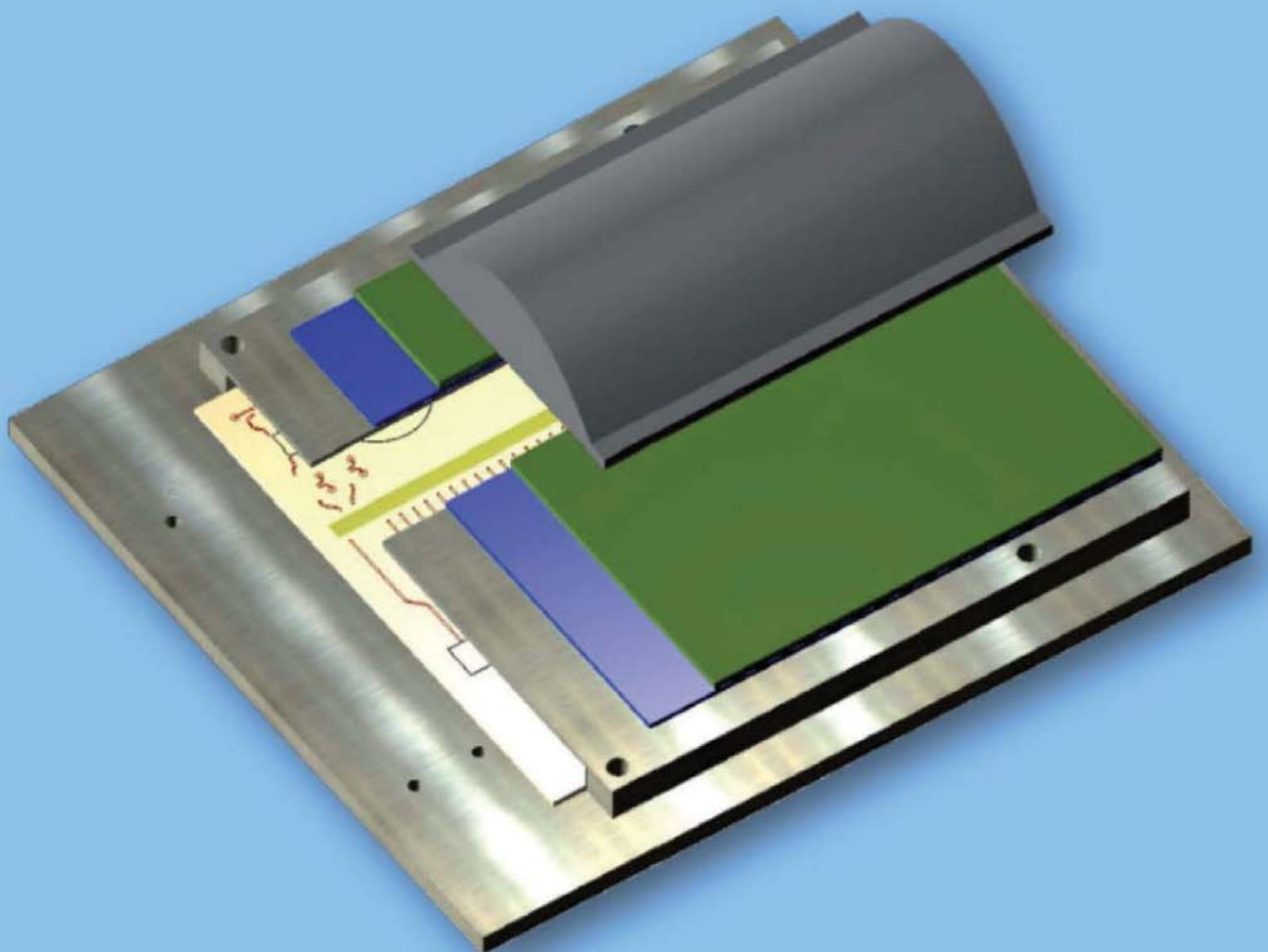


**Peter Feil**

# **Broadband mm-Wave Sensors for Industrial and Security Applications**

---



**Cuvillier Verlag Göttingen**



Broadband mm-Wave Sensors  
for Industrial and Security Applications





ulm university universität  
**uulm**

# **Broadband mm-Wave Sensors for Industrial and Security Applications**

## **DISSERTATION**

zur Erlangung des akademischen Grades eines

## **DOKTOR-INGENIEURS (Dr.-Ing.)**

der Fakultät für Ingenieurwissenschaften  
und Informatik der Universität Ulm

von

**Peter Feil  
aus München**

Gutachter: Prof. Dr.-Ing. Wolfgang Menzel  
Prof. Paul-Alain Rolland  
Amtierender Dekan: Prof. Dr.-Ing. Klaus Dietmayer

Ulm, 22. Juni 2012



Bibliografische Information der Deutschen Nationalbibliothek  
Die Deutsche Nationalbibliothek verzeichnet diese Publikation in der  
Deutschen Nationalbibliografie; detaillierte bibliografische Daten sind  
im Internet über <http://dnb.d-nb.de> abrufbar.

1. Aufl. - Göttingen: Cuvillier, 2013  
Zugl.: Ulm, Univ., Diss., 2012

978-3-95404-334-7

© CUVILLIER VERLAG, Göttingen 2013  
Nonnenstieg 8, 37075 Göttingen  
Telefon: 0551-54724-0  
Telefax: 0551-54724-21  
[www.cuvillier.de](http://www.cuvillier.de)

Alle Rechte vorbehalten. Ohne ausdrückliche Genehmigung  
des Verlages ist es nicht gestattet, das Buch oder Teile  
daraus auf fotomechanischem Weg (Fotokopie, Mikrokopie)  
zu vervielfältigen.

1. Auflage, 2013  
Gedruckt auf säurefreiem Papier

978-3-95404-334-7



This thesis has resulted from my employment as a research assistant at the Institute of Microwave Techniques at the University of Ulm. Parts of the work have been carried out in cooperation with the Laboratoire d'Electronique, Antennes et Télécommunications at the University of Nice.

I highly acknowledge Prof. Dr. Wolfgang Menzel enabling me to work on this very interesting topic and always providing a dedicated supervision and support.

I would particularly like to thank Prof. Claire Migliaccio for the kind cooperation and for offering the possibility to investigate an interesting and important field of application. Working together was a great pleasure.

Additionally I am grateful to Prof. Paul-Alain Rolland for acting as a second reviewer and taking the way to Ulm for the examination.

I would also like to thank all of my colleagues at the Institute of Microwave Techniques. The pleasant and amicable atmosphere was always a great motivation and the basis of many valuable friendships. My special thanks go to Dr. Frank Bögelsack for his support throughout the entire work and especially for proof-reading the thesis. The delightful discussions within but also beside the technical domain are unforgotten.

The fabrication of the mm-wave hardware would not have been possible without the competence of the technical staff members within the Institute of Microwave Techniques, at the department of PCB technology and the mechanical workshop. All of them I owe my thanks for their work.

Finally, I would like thank my partner Sabine, my family and all of my friends, who went along with me during the last years and encouraged me especially during the completion of the dissertation.

Ulm, June 2012

Peter Feil





# Contents

<b>1</b>	<b>Introduction</b>	<b>1</b>
<b>2</b>	<b>Fundamentals of Radar Principles and Signal Processing</b>	<b>5</b>
2.1	Radar Principles . . . . .	6
2.1.1	Coherent Pulse Radars . . . . .	6
2.1.2	Analytical Description of the Radar Channel . . . . .	7
2.1.3	Pulse Compression . . . . .	8
2.2	Theory of FM-CW Radars . . . . .	10
2.2.1	Mathematical Description of FM-CW Radars . . . . .	12
2.2.2	Comparison to SF-CW radars . . . . .	14
2.3	Fundamentals of Spectral Estimation . . . . .	15
2.3.1	Processing of Time Limited Datasets . . . . .	16
2.3.2	Model-Based Spectral Estimation . . . . .	21
2.3.3	Spectral Estimation of Deterministic Signals . . . . .	23
2.3.4	Enhancing the Resolution using Linear Prediction . . . . .	24
2.3.5	Eigenanalysis-based Techniques . . . . .	27
2.4	Wideband Calibration of FM-CW Sensors . . . . .	28
2.4.1	Calibration of the Sensor Ringing or Offset . . . . .	29
2.4.2	Correction of the Signal Dispersion . . . . .	29
2.5	Doppler Processing and Velocity Measurement . . . . .	32
2.5.1	Resolving Range Doppler Ambiguities by Triangular Modulation . . . . .	33
2.5.2	Phase Processing of Pulse Trains . . . . .	34
2.6	Digital Beamforming . . . . .	37
2.6.1	Narrow Band Data Model . . . . .	38
2.6.2	Conventional Beamformers . . . . .	39
2.6.3	Correlation Matrix in Beamforming Applications . . . . .	41
2.6.4	Adaptive Beam Formers . . . . .	42
2.6.5	Two-Dimensional Imaging . . . . .	48
2.6.6	Broadband True Time Delay Beamformer . . . . .	49
<b>3</b>	<b>Broadband FM-CW Sensor at 78 GHz</b>	<b>53</b>
3.1	Overview and Operating Modes . . . . .	53



3.2	Processing Technology and Interconnects . . . . .	55
3.2.1	Microstrip Line-to-Waveguide Transition . . . . .	56
3.2.2	Planar mm-Wave Components . . . . .	59
3.3	FM-CW Synthesiser . . . . .	60
3.3.1	Modelling and Performance of Direct Digital Synthesisers . . . . .	61
3.3.2	Phase-Locked Loop Design . . . . .	63
3.4	Analogue DC and Baseband Electronics . . . . .	65
3.4.1	Intermediate Frequency Filtering Stage . . . . .	66
3.5	Comprehensive FM-CW Model and Simulation Results . . . . .	68
3.6	Performance Evaluation . . . . .	73
3.7	Advanced Operating Modes . . . . .	76
3.7.1	Heterodyne Reception with Periodically Modulated LO . . . . .	76
3.7.2	Leakage Phase Noise Suppression . . . . .	77
3.7.3	Phase Noise Cancellation Using a Dual Channel Mixer . . . . .	79
<b>4</b>	<b>Imaging Sensor with Switched Transmit Antenna Array</b> . . . . .	<b>81</b>
4.1	Switching Network and Patch Array . . . . .	82
4.2	Cylindrical Lens Design and Farfield Characteristics . . . . .	83
4.3	Coarray-based Beamforming for not Fully Populated Arrays . . . . .	90
4.4	Measurement Results Obtained with the Switched DBF Sensor . . . . .	92
4.4.1	Measurement of Point Scatterers . . . . .	92
4.4.2	Measurement of a Complex Environment . . . . .	95
4.5	Imaging of Moving Targets using a Switched Sensor Array . . . . .	98
4.5.1	Optimised Switching Sequence for Reduced Doppler Sensitivity . . . . .	99
4.5.2	ESPRIT-based Subarray Approach for Doppler Mitigation . . . . .	103
<b>5</b>	<b>Applications Investigated with the Developed Sensors</b> . . . . .	<b>105</b>
5.1	Runway Surveillance . . . . .	105
5.1.1	Antenna Concept . . . . .	105
5.1.2	Signal Processing . . . . .	110
5.1.3	Experimental Results . . . . .	111
5.2	MM-Wave Synthetic Aperture Radar . . . . .	115
5.2.1	SAR Demonstrator Setup . . . . .	115
5.2.2	Modes of Operation and Signal Processing . . . . .	116
5.2.3	Performance Evaluation in Stripmap Mode at 77 GHz . . . . .	116
5.2.4	Spotlight Operation at 24 GHz . . . . .	119
5.2.5	Three Dimensional Combined SAR and DBF Processing at 24 GHz and 77 GHz . . . . .	120
5.2.6	Further Applications . . . . .	126



<b>6</b>	<b>Summary and Conclusion</b>	<b>127</b>
<b>A</b>	<b>Appendix</b>	<b>129</b>
A.1	Noise Modelling Using Rice's Second Model . . . . .	129
A.2	Single Sideband Phase Noise Spectrum . . . . .	129
A.3	Phase Noise Cancellation Factor . . . . .	130
A.4	Correlation Sequence and Matrix . . . . .	131
	<b>Bibliography</b>	<b>135</b>





## List of Symbols and Abbreviations

As far as possible, symbols are chosen in accordance to DIN 1304. In case of multiple usage of a symbol the meaning is given by the context. Well known operators and functions are not stated here.

The page numbers point to the first appearance of a symbol or abbreviation.

### Symbols

$x^*$	Complex conjugate of $x$ . . . . .	9
$\mathbf{x}^H$	Complex conjugate transpose (hermitian) of $\mathbf{x}$ . . . . .	40
$\hat{x}$	Estimate of $x$ . . . . .	17
$s_1 \star s_2$	Convolution of the signals $s_1$ and $s_2$ . . . . .	9
$\mathbf{A}$	Array manifold . . . . .	39
$\mathcal{E}\{x\}$	Expectation value of the random variable $x$ . . . . .	16
$F$	Noise figure . . . . .	7
$\mathcal{F}\{s(t)\}$	Fourier transform of signal $s(t)$ . . . . .	15
$\Delta f$	Frequency resolution . . . . .	8
$\Delta F$	RF bandwidth of the radar waveform . . . . .	8
$\mathcal{H}$	Hilbert transform . . . . .	28
$k_B$	Boltzmann constant, $k_B \approx 1.38 \cdot 10^{-23} \frac{\text{J}}{\text{K}}$ . . . . .	8
$P_{ss}(f)$	Power spectral density of signal $s(t)$ . . . . .	15
$r_{ss}(t)$	Autocorrelation function of signal $s(t)$ . . . . .	9
$\mathbf{R}_{xx}$	Autocorrelation matrix . . . . .	41
$S$	Slope of linear frequency modulation . . . . .	9
$t$	Time or slow time (in case of Doppler processing) . . . . .	32
$\mathbf{w}, \mathbf{W}$	Beamforming weights . . . . .	37
$\theta$	Angle in DBF/imaging plane . . . . .	37
$\sigma$	Radar Cross Section (RCS) . . . . .	7
$\tau$	Fast (intra pulse) time . . . . .	12
$\phi$	Instantaneous phase in time domain . . . . .	12
$\Phi$	Phase in frequency domain . . . . .	34
$\varphi$	Angle perpendicular to DBF/imaging plane . . . . .	85



## List of Symbols and Abbreviations

---

### Abbreviations

ADC	Analogue-to-Digital Converter . . . . .	10
AM	Amplitude Modulation . . . . .	13
BPSK	Binary Phase Shift Keying . . . . .	54
CFAR	Constant False Alarm Rate . . . . .	16
DBF	Digital Beam Forming . . . . .	1
DDS	Direct Digital Synthesiser . . . . .	54
DFT	Discrete Fourier Transform . . . . .	24
DRA	Direct Reading Attenuator . . . . .	73
DTFS	Discrete Time Fourier Series . . . . .	23
FM-CW	Frequency Modulated Continuous Wave . . . . .	2
FOD	Foreign Object Debris . . . . .	1
FT	Fourier Transform . . . . .	49
FFT	Fast Fourier Transform . . . . .	19
IF	Intermediate Frequency . . . . .	7
IFT	Inverse Fourier Transform . . . . .	49
I/Q	In-phase/Quadrature . . . . .	6
LO	Local Oscillator . . . . .	6
MEMS	Micro Electro Mechanical System . . . . .	3
MMIC	Monolithic Microwave Integrated Circuit . . . . .	55
MSL	Microstrip Line . . . . .	53
OFDM	Orthogonal Frequency Division Multiplexing . . . . .	9
PCB	Printed Circuit Board . . . . .	55
PLL	Phase-Locked Loop . . . . .	54
PM	Phase Modulation . . . . .	13
PSD	Power Spectral Density . . . . .	15
PTFE	Polytetrafluoroethylene . . . . .	82
RCS	Radar Cross Section . . . . .	7
RF	Radio Frequency . . . . .	6
RWG	Rectangular Waveguide . . . . .	53
SAR	Synthetic Aperture Radar . . . . .	2
SCNR	Signal-to-Clutter-and-Noise Ratio . . . . .	122
SiGe	Silicon Germanium . . . . .	3
SI-WG	Substrate Integrated Waveguide . . . . .	57



**Abbreviations**

SNR	Signal-to-Noise Ratio . . . . .	7
TBP	Time Bandwidth Product . . . . .	8
VCO	Voltage Controlled Oscillator . . . . .	6
XCO	Crystal Controlled (Quartz) Oscillator . . . . .	61



# 1 Introduction

Since many decades radar (RAdio Detection And Ranging) is used for the remote sensing of objects at far ranges and under adverse conditions like dust, snow or rain. Even though the initial idea dates back to 1904 [1], operational systems have been addressed starting from 1934 due to the potential military applications. Especially during the last 50 years a rapid development has occurred [2], that affected every single aspect of a radar sensor. While the operating frequency was pushed to higher bands, the signal generation changed from magnetron based approaches over waveguide circuits containing Gunn or IMPATT diodes to monolithic integrated and even multifunctional devices. Taking benefit from the general development of semiconductor devices in other fields, radar technology became affordable also in civil applications. Among those applications one can find space, air and ground based surveillance systems as well as industrial level gauging or simple motion sensors.

Within the last 30 years commercial mm-wave technology was mainly driven by the automotive industry. Having started at 24 GHz, the suppliers in Europe are now forced to switch to the 76–81 GHz frequency band due to administrative regulations. As a consequence, great efforts have been done in developing mm-wave components suitable for low cost mass production. Nowadays, chip sets or even single chip frontends are available, mainly based on GaAs or SiGe technology. Even though these devices are intended for automotive sensors, the technology is also available for fields with low volume and even niche applications. As an example the surveillance in harsh environments [3], the measurement of aircraft wake vortices [4, 5, 6], or the detection of foreign object debris (FOD) on airports [7] shall be mentioned.

With respect to radar signal processing, the availability of cost effective, high speed computers, analogue digital converters, and signal processors enables the transition of processing tasks from the analogue to the digital domain. Thereby, not only the radar processing itself, but also the antenna technology is concerned. Mechanically steered antennas and passive or active electronically steered antenna arrays are more and more replaced by digital beamforming (DBF) using multichannel sensors.

The application of such techniques has been demonstrated at a frequency of 24 GHz e.g. in [8, 9, 10], but there are several reasons to use higher frequencies. Aside from the before mentioned regulatory constraints, the bandwidth available

at 79 GHz is much larger. Additionally, a higher antenna gain and narrower beamwidth can be achieved while maintaining the sensor dimensions. This fact makes this frequency range even more attractive for applications requiring a high resolution. However, when changing over to such high frequencies, several issues arise with respect to fabrication precision and cost.

The work described in this thesis deals with the development of a wideband sensor at 79 GHz suited to address many potential applications within different areas like industrial and security sensing. The main design goals are

- frequency modulated continuous wave (FM-CW) operation covering at least 5 GHz bandwidth,
- frontend with a single transmit and two receive channels,
- implementation of experimental options, e.g. for phase noise cancellation,
- switched antenna array extension for DBF operation,
- use of low cost printed circuit board technology and standard precision manufacturing.

Apart from the actual sensor design, the prediction of a system's performance has become an important issue to reduce the commercial risk of a product development. Especially at mm-wave frequencies the sensitivity of an FM-CW sensor is limited by the noise of the signal source. In [8] a computationally efficient approach is proposed to predict the influence of phase noise. The model described there includes some simplifications to accomplish a signal representation in terms of the instantaneous frequency. In order to overcome these simplifications, an instantaneous phase model will be derived in this work enhancing the accuracy without increasing the complexity.

Additionally, signal processing techniques will be developed coping with the large bandwidth and mitigating the effects of dynamic scenarios in conjunction with a switched antenna configuration. Finally, different sensor configurations will be validated in various exemplary applications such as the detection of FOD or environmental monitoring using synthetic aperture radar (SAR).

The thesis is organised in five chapters. After this introduction the fundamentals of the FM-CW radar are introduced in Chapter 2. Thereby, the basic means of intra pulse modulation and compression are treated as well as the signal processing in terms of range, Doppler shift, and digital beamforming. In Chapter 3 simulation and design aspects of the 79 GHz FM-CW frontend are presented together with an evaluation of the sensor performance. A description of the switched antenna array extension is found in Chapter 4. Due to the

---

configuration of this array the generic DBF algorithms require some additional considerations, that are also addressed in this context. Simulation and measurement results demonstrate the capabilities of the switched array. Chapter 5 summarises some of the applications that have been investigated with the developed sensor hardware. The detection of FOD is described using, in a first step, mechanically steered sensors. The following part presents the results obtained with a SAR demonstrator setup, including typical operating modes such as stripmap SAR and spotlight SAR, but also three dimensional sensing by exploiting SAR and DBF. The conclusion in Chapter 6 gives a final summary of the work and discusses future developments enabled by new technologies such as MEMS or SiGe.



## 2 Fundamentals of Radar Principles and Signal Processing

By definition [11] radar (RADio Detection And Ranging) uses the transmission and reception of electromagnetic waves to detect objects and extract their properties such as range and velocity. For example, the round trip delay of radio frequency pulses gives a measure of the target's distance. Fig. 2.1 shows the block diagram of a generic radar system consisting of waveform generator, receiver, and signal processing.

The shape of the pulses and the kind of reception help classifying radar systems. In the most simple case the transmitted waveform is a (rectangular) pulse without any intrinsic modulation. The duration or spatial extent of this pulse determines the range resolution. However, as shown later in this chapter, the maximum range of the radar is limited by the energy per pulse. Consequently, improving the resolution, while maintaining the peak power, reduces the maximum range. A common method to achieve a better resolution without affecting the maximum range is called pulse compression [11]. The exact meaning of this term will be discussed later. Basically, pulse compression is a technique to stretch the transmitted pulse in the time domain and to compress it during reception. This enables reducing the peak power that has to be provided by the transmitter.

Additionally, a distinction is drawn between coherent and non coherent radars.

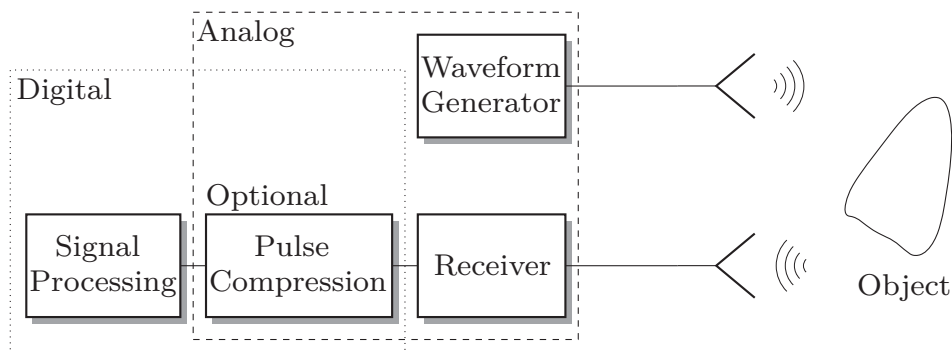


**Fig. 2.1:** Basic block diagram of a generic radar system.

In coherent radars the same oscillator or at least synchronous oscillators are used for waveform generation and down-conversion in the receiver, providing the phase relation between the transmitted and received pulses. It will be shown that this information is crucial for advanced processing methods such as digital beamforming (DBF). As this work deals with that kind of techniques, the further explanations will be restricted to coherent architectures.

## 2.1 Radar Principles

This sub-chapter gives a brief description of coherent pulse radars and introduces the principle of pulse compression and its relation to FM-CW (frequency modulated continuous wave) radars. As the latter one was used within this work, a detailed mathematical description follows together with considerations regarding signal processing.

### 2.1.1 Coherent Pulse Radars

The general principle of coherent pulse radars is shown in Fig. 2.2. The waveform is generated by modulating the output signal of an RF source (VCO, voltage controlled oscillator), and the same source serves as local oscillator (LO) for the receiver. By using two mixers with LO signals shifted by  $90^\circ$ , an in-phase and a quadrature channel is available at the output (I/Q receiver). By means

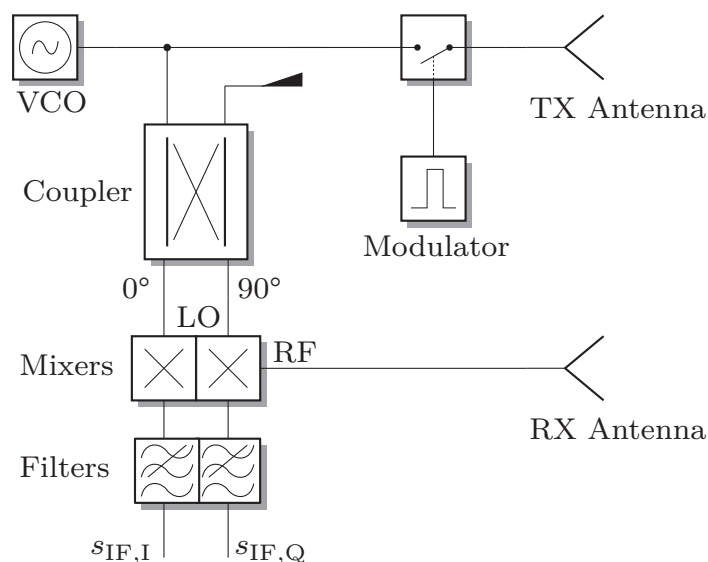


**Fig. 2.2:** Block diagram of a coherent pulse radar.

of this additional information the phase shift between the transmitted and received RF pulse can be measured at the intermediate frequency (IF) outputs ( $s_{\text{IF},\text{I}}$  and  $s_{\text{IF},\text{Q}}$ ) and used for further processing.

### 2.1.2 Analytical Description of the Radar Channel

Between transmitter and receiver the radar signal experiences a significant attenuation, mainly due to free space propagation. The relationship between transmitted and received power is known as the radar equation [12] and shall be shortly derived in the following. Assume a target located at a distance  $R$  in the farfield of the transmitting antenna. Using the transmitted power  $P_{\text{TX}}$  and the antenna gain  $G_{\text{TX}}$  the power density  $S_{\text{TX}}(R)$  at the target is

$$S_{\text{TX}}(R) = \frac{P_{\text{TX}}G_{\text{TX}}}{4\pi R^2}. \quad (2.1)$$

A common way to describe the reflectivity of a target is in terms of the so-called radar cross section (RCS)  $\sigma$ . It is assumed that the power impinging on this hypothetical area  $\sigma$  is scattered uniformly to all directions. Hence, the power density at the location of the radar sensor caused by the scattered signal is

$$S_{\text{RX}}(R) = \frac{S_{\text{TX}}\sigma}{4\pi R^2} = \frac{P_{\text{TX}}G_{\text{TX}}\sigma}{(4\pi)^2 R^4}. \quad (2.2)$$

The effective area of the receiving antenna

$$A_{\text{ant}} = G_{\text{RX}} \frac{\lambda^2}{4\pi} \quad (2.3)$$

gives the relation between the incident power density and the power at the antenna output. Incorporating also the atmospheric attenuation  $\alpha_{\text{atm}}$  which has a considerable influence especially at certain frequencies in the mm-wave range, the radar equation results in

$$P_{\text{RX}}(R) = \frac{P_{\text{TX}}G_{\text{TX}}G_{\text{RX}}\sigma\lambda^2}{(4\pi)^3 R^4} \cdot 10^{\frac{2\alpha_{\text{atm}} \cdot R}{10}}. \quad (2.4)$$

In all radar systems the sensitivity, and consequently the ability to detect small targets, depends on the signal-to-noise ratio (SNR) after reception and pulse compression. The signal power can be calculated with the radar equation (2.4) whereas the noise power is given by the standard noise figure  $F_{\text{RX}}$  of the receiver:

$$P_{\text{noise}} = k_B [T_{\text{ant}} + (F_{\text{RX}} - 1)T_0] \Delta f_{\text{IF}} \quad (2.5)$$

with  $k_B$  being the Boltzmann constant. For an antenna pointing to an environment with the temperature  $T_0 = 290$  K, the equation can be simplified to

$$P_{\text{noise}} = k_B T_0 F_{\text{RX}} \Delta f_{\text{IF}}. \quad (2.6)$$

The bandwidth  $\Delta f_{\text{IF}}$  relevant for the noise power calculation depends on the RF bandwidth  $\Delta F$  and scales with the time-bandwidth product ( $\text{TBP} = T \Delta F$ ) of the transmitted pulse [11]:

$$\Delta f_{\text{IF}} = \frac{\Delta F}{\text{TBP}} = \frac{\Delta F}{T \Delta F} = \frac{1}{T} \quad (2.7)$$

Solving (2.4) for the maximum range at a given SNR yields

$$R_{\text{max}} = \sqrt[4]{\frac{P_{\text{TX}} T G_{\text{TX}} G_{\text{RX}} \sigma}{(4\pi)^3 k_B T_0 F_{\text{RX}} \text{SNR}}}. \quad (2.8)$$

In order to obtain a closed solution the atmospheric attenuation has been neglected. If this is not possible, e.g. for long range radars, the maximum range can be determined numerically.

### 2.1.3 Pulse Compression

In pulse radars the resolution in general is determined by the length or spatial extent of the transmitted pulse. If a better resolution and therefore a shorter pulse is required, the energy per pulse is reduced, if the peak power is kept constant. At the same time the signal-to-noise ratio decreases. A way to overcome this problem is using pulse modulation on transmit and pulse compression in the receiver.

#### Generic Description of Pulse Compression

The considerations in this section are following [11]. Complex analytical signals shall be used for the analysis. They allow the representation of arbitrary modulation schemes such as amplitude, phase, or frequency modulation in a consistent way. A generic modulated pulse can be expressed mathematically as

$$s_{\text{TX}}(\tau) = s_{\text{mod}}(\tau) e^{j\omega_0 \tau}, \quad (2.9)$$

where  $e^{j\omega_0 \tau}$  represents the carrier and  $s_{\text{mod}}(\tau)$  the modulation signal. In the most simple case, the received pulse is a copy of the transmitted pulse delayed by  $\Delta T = \frac{2R}{c_0}$  and weighted with a (in general complex) scalar value  $A$ . After down-conversion the baseband signal is

$$\tilde{s}_{\text{mod}}(\tau) = A s_{\text{mod}}(\tau - \Delta T). \quad (2.10)$$

Pulse compression is done by correlating the received baseband signal with the transmitted template:

$$\begin{aligned}
r_{s\tilde{s}}(\tau) &= A s_{\text{mod}}^*(-\tau) \star s_{\text{mod}}(\tau - \Delta T) \\
&= A \underbrace{s_{\text{mod}}^*(-\tau) \star s_{\text{mod}}(\tau)}_{\text{autocorrelation function } r_{ss}(\tau)} \star \delta(\tau - \Delta T) = A r_{ss}(\tau - \Delta T) \quad (2.11)
\end{aligned}$$

According to (2.11) the response at the output of the pulse compression is the time-shifted autocorrelation function of the modulation signal. Hence, it is obvious, that the choice of the modulation signal strongly affects resolution and range sidelobes of the radar.

For radars without pulse compression the resolution is restricted to the temporal extent  $T$  of the transmitted (rectangular) pulse with a respective bandwidth  $\Delta F = \frac{1}{T}$ . Pulse compression techniques enable the use of waveforms occupying the same bandwidth but being considerably stretched in the time domain. The ability to compress such waveforms is given by their time-bandwidth product.

Common modulation schemes [12] are (non-)linear FM, pseudo random sequences, and, recently, even OFDM signals [13, 14]. Among these possibilities, linear FM radars play an important role as pulse compression can be partly shifted to the analogue domain. A discussion is given in the following section.

### Application of Pulse Compression to Linear Frequency Modulated Pulses

A linear frequency-modulated transmit signal can be written as

$$s_{\text{TX}}(\tau) = s_{\text{mod}}(\tau) e^{j\omega_0 \tau} = e^{j\pi S \tau^2} e^{j\omega_0 \tau}, \quad (2.12)$$

where  $S$  denotes the slope of the frequency modulation in Hz/s. All considerations can be done in the baseband by omitting the carrier signal  $e^{j\omega_0 \tau}$ .

Due to free space propagation the modulation at the receiver input is delayed by  $\Delta T = \frac{2R}{c_0}$ :

$$\tilde{s}_{\text{mod}}(\tau) = s_{\text{mod}}(\tau - \Delta T) = e^{j\pi S (\tau - \Delta T)^2} \quad (2.13)$$

Again pulse compression is done by correlating the received pulse with the transmitted one:

$$\begin{aligned}
 r_{s\tilde{s}}(\tau) &= s_{\text{mod}}^*(-\tau) \star \tilde{s}_{\text{mod}}(\tau) \\
 &= \int_{-\infty}^{\infty} s_{\text{mod}}^*(-\tau') \tilde{s}_{\text{mod}}(\tau - \tau') d\tau' = \int_{-\infty}^{\infty} s_{\text{mod}}^*(\tau') \tilde{s}_{\text{mod}}(\tau + \tau') d\tau' \\
 &= \int_{-\infty}^{\infty} \tilde{s}_{\text{mod}}(\tau') s_{\text{mod}}^*(\tau' - \tau) d\tau' \\
 &= \int_{-\infty}^{\infty} \tilde{s}_{\text{mod}}(\tau') e^{-j\pi S(\tau^2 - 2\tau\tau' + \tau'^2)} d\tau' \\
 &= e^{-j\pi S\tau^2} \int_{-\infty}^{\infty} \tilde{s}_{\text{mod}}(\tau') \underbrace{e^{-j\pi S\tau'^2}}_{\text{Dechirp}} \underbrace{e^{-j2\pi(-S)\tau\tau'}}_{\text{Fourier transform}} d\tau' \quad (2.14)
 \end{aligned}$$

Formally, in case of a linear frequency modulation the task of pulse compression can be split into a “dechirp” operation and a Fourier transform. After the dechirp the signal bandwidth is greatly reduced. Hence, an analogue implementation of this part is preferable, as the sampling rate of the ADC can be much lower. A possible solution is feeding the receiver with a chirped local oscillator signal. This is exactly what is done in FM-CW radars as described in Section 2.2.

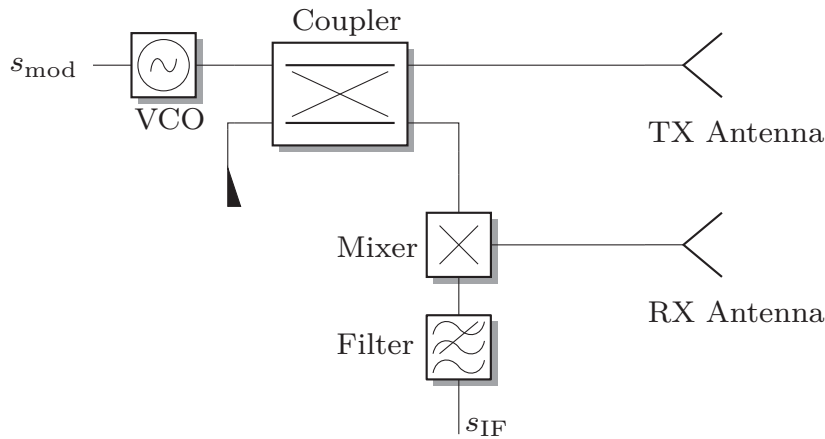
## 2.2 Theory of FM-CW Radars

Fig. 2.3 shows a simplified block diagram of a frequency modulated continuous wave (FM-CW) radar. A voltage controlled oscillator (VCO) is used to generate a frequency modulated transmit signal. Neglecting dispersion, the received signal is simply an attenuated and delayed copy of the transmitted signal. Due to the frequency modulation there is a frequency offset between the VCO output and the receiver input. Using a linear modulation scheme as shown in Fig. 2.4 this frequency offset is constant. Hence, the output signal of the mixer is a harmonic signal. Using the definitions in Fig. 2.4 the slope of the linear frequency modulation is

$$S = \frac{\Delta F}{T} \quad (2.15)$$

and the intermediate frequency results in

$$f_{\text{IF}} = S \cdot \Delta T = S \cdot 2 \frac{R}{c_0}, \quad (2.16)$$



**Fig. 2.3:** Simplified block diagram of an FM-CW radar.

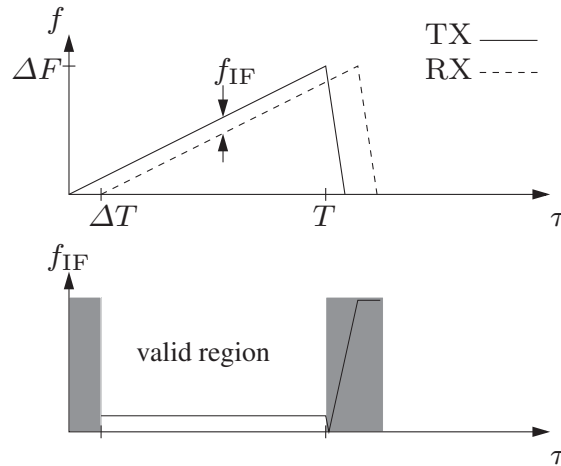


**Fig. 2.4:** Instantaneous frequency of transmitted (TX), received (RX) and intermediate frequency (IF) signal.

where  $\Delta T$  is the round trip delay between sensor and target. Solving (2.16) for the target distance  $R$  yields

$$R = \frac{f_{\text{IF}} c_0}{2S}. \quad (2.17)$$

According to (2.17)  $R$  is directly proportional to the intermediate frequency  $f_{\text{IF}}$ . Thus, for FM-CW radars the measurement of time delays is equivalent to a frequency measurement. For a larger number of targets the complete spectrum of the IF signal has to be estimated. Some possible methods are addressed in Section 2.3.

### 2.2.1 Mathematical Description of FM-CW Radars

The frequency domain description in the last paragraph neglects effects such as dispersion and modulation nonlinearities. Especially wideband FM-CW sensors are affected by these imperfections as they degrade the target response (point spread function) in terms of range resolution and sidelobes. To address as many effects as possible, a comprehensive model has to be set up in the time domain.

The instantaneous angular frequency at the output of a signal source with linear frequency modulation can be written as

$$\omega(\tau) = \omega_0 + 2\pi S\tau + e_{\text{mod}}(\tau), \quad (2.18)$$

where  $e_{\text{mod}}(\tau)$  contains the deviation from a perfectly linear modulation which will always occur in technical implementations. Considering also the phase noise  $\phi_n(\tau)$  of the source, the instantaneous phase of the signal is

$$\begin{aligned} \phi_{\text{SRC}}(\tau) &= \int_{\tau'=0}^{\tau} (\omega_0 + 2\pi S\tau' + e_{\text{mod}}(\tau')) d\tau' + \phi_n(\tau) \\ &= \omega_0\tau + \pi S\tau^2 + \int_{\tau'=0}^{\tau} e_{\text{mod}}(\tau') d\tau' + \phi_n(\tau) \\ &= \omega_0\tau + \pi S\tau^2 + \phi_e(\tau) + \phi_n(\tau). \end{aligned} \quad (2.19)$$

Taking into account the over-all frequency response of the transmit path

$$H_{\text{TX}}(\omega) = A_{\text{TX}}(\omega)e^{j\phi_{\text{TX}}(\omega)}, \quad (2.20)$$

the signal transmitted by the antenna is

$$\begin{aligned} s_{\text{TX}}(\tau) &= A_{\text{TX}}(\omega(\tau)) \cos[\phi_{\text{SRC}}(\tau) + \phi_{\text{TX}}(\omega(\tau))] \\ &= A_{\text{TX}}(\omega(\tau)) \cos[\omega_0\tau + \pi S\tau^2 + \phi_e(\tau) + \phi_n(\tau) + \phi_{\text{TX}}(\omega(\tau))] \end{aligned} \quad (2.21)$$

with the instantaneous angular frequency  $\omega$  linked to  $\tau$  according to (2.18).

The received signal is an attenuated copy of the transmitted signal, delayed by one round trip delay  $\Delta T = 2\frac{R}{c_0}$  between sensor and target.

However, for a complete description also the frequency response of the receive path

$$H_{\text{RX}}(\omega) = A_{\text{RX}}(\omega) \cdot e^{j\phi_{\text{RX}}(\omega)} \quad (2.22)$$

has to be considered. Hence:

$$s_{\text{RX}} = A_{\text{RX}}(\omega(\tau - \Delta T)) A_{\text{TX}}(\omega(\tau - \Delta T)) \cdot \cos[\phi_{\text{SRC}}(\tau - \Delta T) + \phi_{\text{TX}}(\omega(\tau - \Delta T)) + \phi_{\text{RX}}(\omega(\tau - \Delta T))] \quad (2.23)$$

For the modelling of the receiver a simplification is used. It is assumed that the frequency response of the mixer with respect to the local oscillator frequency does *not* depend on the actual intermediate frequency. Using this assumption the output signal of the receiver is

$$s_{\text{IF}}(\tau) = s_{\text{RX}}(\tau) \cdot A_{\text{MXR}}(\omega(\tau)) \cos[\phi_{\text{SRC}}(\tau) + \phi_{\text{MXR}}(\omega(\tau))], \quad (2.24)$$

where  $s_{\text{RX}}(\tau)$  is the receiver input signal,  $A_{\text{MXR}}(\omega)$  the conversion loss as a function of the LO frequency, and  $\phi_{\text{MXR}}(\omega)$  the phase shift introduced by the mixer. Equation (2.24) can be rewritten as

$$s_{\text{IF}}(\tau) = A_{\text{RX}}(\omega(\tau - \Delta T)) A_{\text{TX}}(\omega(\tau - \Delta T)) A_{\text{MXR}}(\omega(\tau)) \cdot \cos[\phi_{\text{SRC}}(\tau - \Delta T) + \phi_{\text{TX}}(\omega(\tau - \Delta T))] \cdot \cos[\phi_{\text{SRC}}(\tau) + \phi_{\text{MXR}}(\omega(\tau))]. \quad (2.25)$$

Expanding (2.25) and omitting the high frequency signal components suppressed by the low pass behaviour of the IF section yields

$$s_{\text{IF}}(\tau) = A_{\text{RX}}(\omega(\tau - \Delta T)) A_{\text{TX}}(\omega(\tau - \Delta T)) A_{\text{MXR}}(\omega(\tau)) \cdot \left. \begin{aligned} & \cos[2\pi S \Delta T \tau + \omega_0 \Delta T - \pi S \Delta T^2 \\ & + \phi_e(\tau) - \phi_e(\tau - \Delta T) \\ & + \phi_{\text{MXR}}(\omega(\tau)) - \phi_{\text{TX}}(\omega(\tau - \Delta T))] \end{aligned} \right\} \begin{array}{l} \text{AM} \\ \text{sinusoid} \\ \text{PM} \end{array} + \phi_n(\tau) - \phi_n(\tau - \Delta T) \quad \text{phase noise} \quad (2.26)$$

Neglecting the frequency responses and the modulation nonlinearity in (2.26), the output signal of the receiver is a sinusoid, the frequency of which is directly related to the target distance.

Some interesting features can be derived from (2.26). All the system imperfections lead to a modulation of the desired sinusoidal signal in amplitude and phase. With respect to the modulation nonlinearity it can be seen that the influence almost cancels out for short delays  $\Delta T$  and low frequency components of  $\phi_e(\tau)$ . The same is true for the phase noise  $\phi_n(\tau)$  and is known as an effect called phase noise cancellation. A detailed discussion is given in Section A.3 on page 130.

### 2.2.2 Comparison to SF-CW radars

The comparison of an FM-CW radar with an SF-CW (Stepped Frequency Continuous Wave) radar provides a different view on the meaning of the IF signal. This insight is important for the derivation of calibration methods (Sec. 2.4) and true time delay beamforming (Sec. 2.3).

SF-CW radars are closely related to FM-CW radars. Instead of a linear frequency modulation a stepped modulation is used (Fig. 2.5). The output

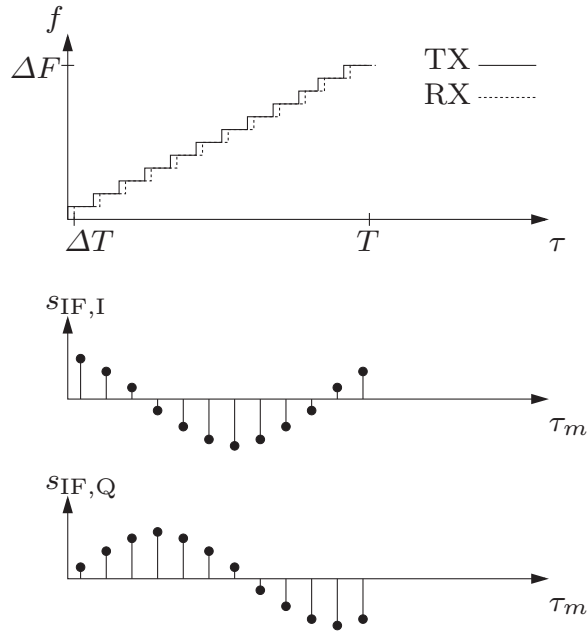


**Fig. 2.5:** Instantaneous frequency of transmitted (TX) and received (RX) signal (top); I- and Q-channel output of the mixer (centre and bottom).

signals of the I- and Q-channel of the receiver are sampled at the discrete times  $\tau_m$ . In order to mitigate settling effects, the delay between each frequency step and the respective sampling has to be larger than the maximum propagation delay. The mathematical description for the in-phase channel follows (2.26) with the modification  $\omega(\tau_m - \Delta T) = \omega(\tau_m)$  and omitting the constant phase term  $-\pi S \Delta T^2$  and the linearity related part:

$$\begin{aligned}
 s_{IF,I}(\tau_m) = & A_{RX}(\omega(\tau_m)) A_{TX}(\omega(\tau_m)) A_{MXR}(\omega(\tau_m)) \cdot \text{amplitude} \\
 & \cos[\omega(\tau_m) \cdot \Delta T] \text{ phase difference} \\
 & + \phi_{LO}(\omega(\tau_m)) - \phi_{TX}(\omega(\tau_m)) \\
 & + \phi_n(\tau_m) - \phi_n(\tau_m - \Delta T)] \text{ phase noise} \quad (2.27)
 \end{aligned}$$

The output signal of the quadrature channel is obtained in a similar way. As there is no frequency offset between the transmitted and received signal, the mixer output is determined by the amplitude of the received signal, the phase difference introduced by the round trip delay, and the frequency responses of transmit and receive path. Provided an I/Q-mixer is used, the real and imaginary part can be obtained for each frequency step. By comparing the setup with a vector network analyser it is obvious, that the measured data give the overall complex frequency response of the radar channel at the instantaneous frequency  $\omega(\tau_m) = \omega_0 + 2\pi \cdot S \cdot \tau_m$ . Hence, the pulse response can be calculated using the inverse Fourier transform.

The same considerations can be made for an FM-CW setup, if the frequency offset  $f_{IF} = S \cdot \Delta T$  is sufficiently small and the approximation  $\omega(\tau - \Delta T) \approx \omega(\tau)$  is allowed. Typically no I/Q receivers are used in FM-CW radars. So only the real part of the complex frequency response is measured. As the pulse response of the radar channel is a causal and real valued signal, the imaginary part can be calculated using the Hilbert transform [15, 16].

This interpretation of the baseband signal may lead to some confusion as the samples of the IF-time domain signal are linked to the frequency response of the radar channel in the RF-frequency domain. In the following considerations the prefix “IF” or “RF” will be used, whenever the terms “frequency domain” and “time domain” are ambiguous.

## 2.3 Fundamentals of Spectral Estimation

The extraction of the range profile in FM-CW radars can be done by any kind of spectral estimation. Depending on the application a trade-off has to be found between resolution, computational effort, and noise shaping. In the following some aspects of stochastic signals are covered more in detail, as they become important for some of the the digital beamforming methods in Section 2.6.

A very good overview of spectral estimation techniques can be found in [17]. The choice of the estimator strongly depends on the nature of the respective signal. Basically, there are two classes of signals, stochastic signals such as noise and deterministic signals, that may be described as a superposition of sinusoids. A generic approach for investigating the properties of an unknown signal is the estimation of its power spectral density (PSD).

Formally the PSD of the signal  $s(t)$  is obtained by the Fourier transform of its autocorrelation function

$$P_{ss}(f) = \mathcal{F}\{s^*(-t) \star s(t)\} = \mathcal{F}\{r_{ss}(t)\} = |\mathcal{F}\{s(t)\}|^2, \quad (2.28)$$

where  $r_{ss}(t)$  is the autocorrelation function of the stochastic process or the deterministic signal. If this autocorrelation function is known for all times  $t$ ,

the squared magnitude of the Fourier transform of  $s(t)$  is exactly the same as the Fourier transform of the autocorrelation function. This relation is known as the Wiener-Khintchine theorem.

However, two difficulties arise for both stochastic and deterministic signals. Firstly, the autocorrelation function can only be estimated, as in practical implementations the signal is observed over a limited time. This leads to an inaccurate estimate of the noise spectral density and the well-known leakage effect in the spectrum [18]. Secondly, only one possible sample of the underlying random process is available for stochastic signals. Hence, the Fourier transform only gives a so-called “sample spectrum”, as it yields a different result for each observation of the process [17]. This means that the actual PSD is the expectation of the sample spectra which is calculated as

$$P_{ss}(f) = \mathcal{E} \left\{ |\mathcal{F}\{s(t)\}|^2 \right\}. \quad (2.29)$$

For ergodic processes the expectation value is obtained using time averages or ensemble averages. Time averaging is preferable in most situations, as typically only one observation of the random process is available.

### 2.3.1 Processing of Time Limited Datasets

In signal processing data usually appear as sampled and time-limited blocks of data, e.g. the baseband signal of an FM-CW radar, which is observed during one pulse period  $T$  and sampled using an ADC. If the signal is known to be a superposition of sinusoids, well-known techniques such as the Fourier series or the Fourier transform may be applied. Albeit suffering from leakage and sidelobes (see page 19), amplitude and phase of the sinusoids are obtained by evaluating the Fourier spectrum at its peaks. Additionally, the frequency resolution can be traded off against the sidelobe level using appropriate windowing. However, the spectral density of the noise contained in the signal cannot be estimated due to the above mentioned reasons.

The knowledge of the noise level can be important, e.g. for the automatic constant false alarm rate detection (CFAR) of signals in noise (see Section 5.1). Two kinds of methods for the PSD estimation of noisy signals are found in literature [17], based on periodograms and using correlograms.

The term “periodogram based estimators” summarises methods to smooth the fluctuations of the sample spectrum:

$$\tilde{P}_{ss}(f) = \frac{T_s}{N} \left| \sum_{n=0}^{N-1} s(n) \cdot e^{-j2\pi f \cdot nT_s} \right|^2 \quad (2.30)$$

The periodogram introduced by Daniell [17] smooths the spectrum by averaging adjacent frequency values, which leads to

$$\hat{P}(f_i) = \frac{1}{2P+1} \sum_{n=i-P}^{i+P} \tilde{P}_{ss}(f_n). \quad (2.31)$$

Another approach is to partition the measured data into  $P$  overlapping or non-overlapping segments of length  $D$ . For each block the sample spectrum  $\tilde{P}_{ss}^{(p)}(f)$  is calculated. Thereby, a weighting function may be applied to each block, to control the sidelobe response.

Finally, the PSD estimate is obtained by an averaging of these sample spectra:

$$\hat{P}(f) = \frac{1}{P} \sum_{p=0}^{P-1} \tilde{P}_{ss}^{(p)}(f) \quad (2.32)$$

Well-known examples using this technique are the Bartlett periodogram and the Welch periodogram. The Bartlett periodogram uses non-overlapping segments and a rectangular window, whereas the Welch type permits overlapping and weighting of the segments. Figure 2.6 shows two sinusoidal signals (200 Hz and 300 Hz) embedded in heavy white noise. The overlapping data segments needed for the Welch periodogram are indicated by hatched rectangles of different colour. Considering only one sample spectrum  $\tilde{P}_{ss}^{(p)}(f)$  there are many random spikes, the amplitudes of which are in the order of the weaker signal at 300 Hz. Additionally the flat spectrum of the white noise is not represented well. After the averaging of the sample spectra the two sinusoids can be clearly identified and the noise shaping is improved considerably.

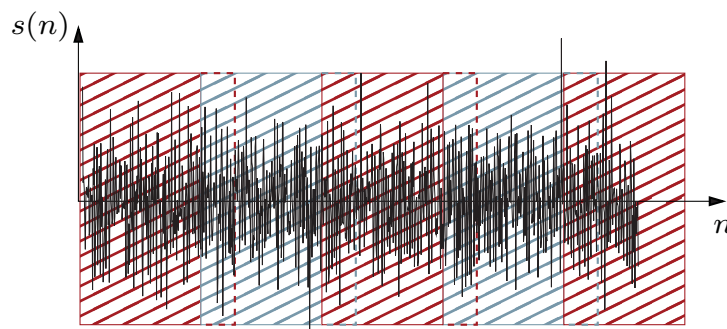


**Fig. 2.6:** Time domain signal of two sinusoids embedded in heavy white noise. The overlapping data segments, processed when calculating the Welch periodogram, are indicated as hatched boxes of different colour.

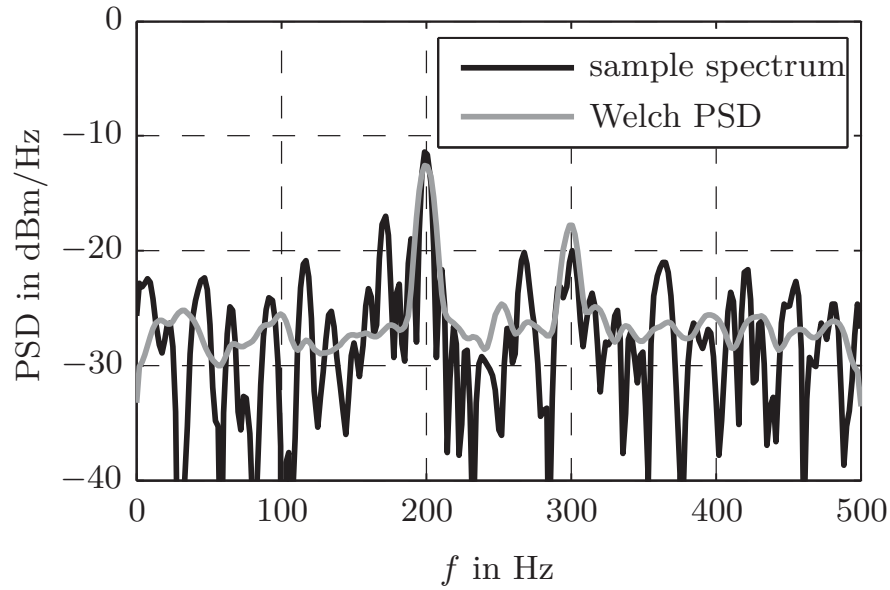


**Fig. 2.7:** Sample spectrum and Welch PSD of two sinusoids embedded in white noise.

Correlogram-based PSD estimators replace the infinite autocorrelation sequence by a finite estimate. That means the exact PSD for time discrete signals

$$P_{ss}(f) = T_s \sum_{m=-\infty}^{\infty} r_{ss}(m) e^{-j2\pi f m T_s} \quad (2.33)$$

is approximated with

$$\hat{P}_{ss}(f) = T_s \sum_{m=-L}^L \hat{r}_{ss}(m) e^{-j2\pi f m T_s}. \quad (2.34)$$

For a data sequence  $s(n)$ , which is known for  $n = 0 \dots N - 1$ , the positive lags of the autocorrelation sequence can be estimated by

$$\hat{r}_{ss}(m) = \frac{1}{(N - m)} \sum_{n=0}^{N-m-1} s(n + m) s^*(n). \quad (2.35)$$

In Section A.4 on page 131 this will be shown to be an unbiased estimate of the actual autocorrelation sequence. For negative indices the calculation has to be modified to

$$\begin{aligned}
 \hat{r}_{ss}(m) &= \frac{1}{(N+m)} \sum_{n=-m}^{N-1} s(n+m)s^*(n) \\
 &= \frac{1}{N-|m|} \sum_{n=0}^{N-|m|-1} s(n)s^*(n+|m|).
 \end{aligned} \tag{2.36}$$

As the negative lags of  $\hat{r}_{ss}(m)$  are simply the complex conjugates of the positive ones, it is sufficient to calculate either of the above equations. This kind of estimation is called statistically consistent, because both the bias and the variance of the estimate tend to zero for large numbers of  $N$ . However, it is remarkable that for limited datasets the estimation uncertainty increases with increasing  $|m|$ . This is due to the fact that the number of data samples available for averaging decreases. Hence, it is advantageous to introduce an appropriate weighting that emphasises autocorrelation lags with lower estimation uncertainty. This leads to the alternative estimator

$$\hat{r}_{ss}(m) = \hat{r}_{ss}^*(-m) = \frac{1}{N} \sum_{n=0}^{N-m-1} s(n+m)s^*(n). \tag{2.37}$$

Effectively, equation (2.37) is obtained by weighting (2.35) with a triangular window. This leads to an obvious bias, but the estimator is still statistically consistent, because this bias vanishes for an infinite number of samples  $N$ .

### Windowing and Frequency Resolution

The Fourier analysis of time-limited or windowed datasets implies that the considered signals are periodic with the window length  $T$ . If this is not the case, truncation effects at the window boundaries lead to broadband sidelobes in the frequency domain. A way to mitigate this effect is using a weighting or windowing prior to the Fourier transform, typically implemented as fast Fourier transform (FFT). Many types of such windows can be found in literature, all of them being designed to provide a certain trade-off between frequency resolution and sidelobe level or shape.

In Fig. 2.8 the spectrum of a rectangular window is shown in comparison with two Chebyshev windows with a sidelobe suppression of 40 dB or 80 dB, respectively.

There are a lot of different definitions of the term frequency resolution such as the 3 dB or the 6 dB width of the spectral response. A definition frequently used in radar applications is the distance between the maximum and the closest

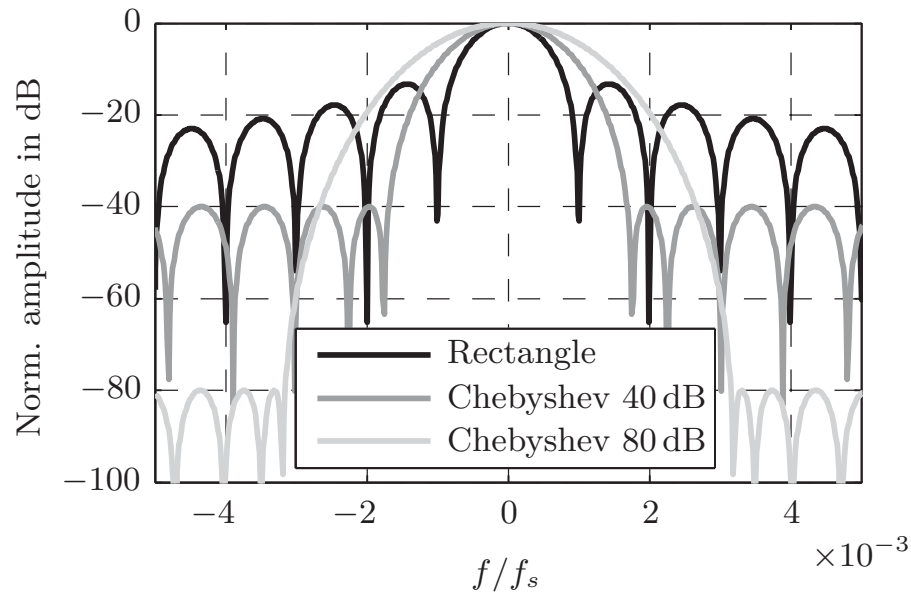


**Fig. 2.8:** Spectra vs. normalised frequency of a rectangular window and two Chebyshev windows with 40 dB and 80 dB sidelobe suppression; the length of the window is  $N = 1000$  in all cases.

minimum. Using this measure it is clearly seen that a suppression of sidelobes leads to a decreased frequency resolution.

As another consequence the signal power is spread over a wider frequency range (equivalent noise bandwidth, ENBW), consequently leading to a processing loss or lower SNR [17]. Sidelobe suppression, frequency resolution and processing loss for the windows investigated above are summarised in Table 2.1. The processing loss stated in Table 2.1 can only be achieved for signal frequen-

Window	Sidelobe Level	Frequ. Resolution	Processing Loss
Rectangular	$< -13.3$ dB	$1/T$	0 dB
Chebyshev	-40 dB	$1.75/T$	1.32 dB
Chebyshev	-80 dB	$3.19/T$	2.41 dB

**Tab. 2.1:** Performance parameters of a rectangular window and two different Chebyshev windows; the frequency resolution is defined as the distance between the maximum and the closest minimum of a window's spectrum.

cies exactly matching the frequency of an FFT basis function. Otherwise an additional loss (scalping loss [19]) has to be considered. However, a dense

frequency spacing of the FFT basis functions is accomplished by means of zero padding [17].

### 2.3.2 Model-Based Spectral Estimation

Parametric signal models help to overcome the limitations arising from the estimation of the autocorrelation sequence. The idea is to fit the parameters of a signal model in a way that the statistical properties of the model output and the observed signal match as good as possible. A well-known approach is using so-called autoregressive moving average (ARMA) models. Basically, this kind of models are digital filters fed by white noise (cf. Fig. 2.9).

Two special cases can be derived from the general ARMA model. Setting all forward coefficients  $b_i = 0$  gives a pure autoregressive (AR) model, while  $a_i = 0$  leads to a moving average (MA) model. AR models are most suited in cases where the PSD contains sharp peaks (all-pole model), whereas a smooth continuous PSD with discrete zeros may be described with an MA model.

A common task in signal processing is detecting the parameters of sinusoidal signals embedded in white noise. Therefore, AR models, due to their all-pole nature, are of the greatest importance among the above mentioned possibilities. Additionally, ARMA models require the solution of a nonlinear problem to determine their coefficients [17], whereas the parameters of AR models can be obtained solving a linear problem. The procedure related to AR models will be shortly outlined in the next sections. Details are found e.g. in [18].

Let  $n(k)$  be the input white noise of an AR model. Hence, the output  $x(k)$  of the model can be expressed in terms of the difference equation

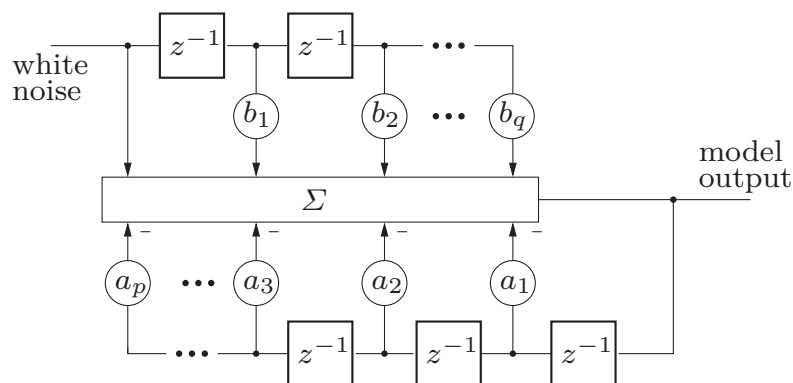


**Fig. 2.9:** Autoregressive moving average (ARMA) model of a random process;  $z^{-1}$  denotes a time delay of one sampling period.

$$x(k) = n(k) - \sum_{\nu=1}^N a_{\nu} \cdot x(k - \nu), \quad (2.38)$$

with  $a_{\nu}$  being the coefficients of the AR model. The autocorrelation sequence of the signal  $x(k)$  is

$$\begin{aligned} r_{xx}(\kappa) &= \mathcal{E}\{x^*(k) \cdot [n(k + \kappa) - \sum_{\nu=1}^N a_{\nu} x(k + \kappa - \nu)]\} \\ &= r_{xn}(\kappa) - \sum_{\nu=1}^N a_{\nu} r_{xx}(\kappa - \nu) \\ &= r_{nx}^*(-\kappa) - \sum_{\nu=1}^N a_{\nu} r_{xx}(\kappa - \nu). \end{aligned} \quad (2.39)$$

With the impulse response  $h_{\text{AR}}(k)$  of the AR model and the power  $\sigma_n^2$  of the white noise signal  $n(k)$ , the following equation holds:

$$\begin{aligned} r_{nx}(\kappa) &= n^*(-\kappa) \star x(\kappa) = n^*(-\kappa) \star n(\kappa) \star h_{\text{AR}}(\kappa) \\ &= \sigma_n^2 \delta(\kappa) \star h_{\text{AR}}(\kappa) \\ &= \sigma_n^2 h_{\text{AR}}(\kappa) \end{aligned} \quad (2.40)$$

As the impulse response of the AR model is causal:

$$r_{nx}(-\kappa) = \sigma_n^2 h_{\text{AR}}(-\kappa) = 0 \text{ for all } \kappa > 0 \quad (2.41)$$

and  $h(0) = 1$  is true according to (2.38), the correlation lags  $r_{xx}(\kappa)$  are

$$\begin{aligned} r_{xx}(\kappa) &= \sigma_n^2 && \text{for } \kappa = 0, \\ r_{xx}(\kappa) &= - \sum_{\nu=1}^N a_{\nu} r_{xx}(\kappa - \nu) && \text{for } \kappa > 0. \end{aligned} \quad (2.42)$$

This yields the matrix expression

$$\mathbf{R}_{xx} \cdot \mathbf{a} = -\mathbf{r}_{xx}, \quad (2.43)$$

where  $\mathbf{R}_{xx}$  is the correlation matrix introduced in Section A.4 on page 131, using the symmetry of the autocorrelation sequence  $r_{xx}(-\kappa) = r_{xx}^*(\kappa)$ . The vectors

$\mathbf{a}$  and  $\mathbf{r}_{xx}$  contain the coefficients of the  $N$ th order AR model and the first  $N$  lags of the autocorrelation sequence, respectively.

The direct solution of this equation is given by the inversion of the autocorrelation matrix

$$\mathbf{a} = -\mathbf{R}_{xx}^{-1} \mathbf{r}_{xx}, \quad (2.44)$$

which is typically referred to as the Yule-Walker equation. As  $\mathbf{R}_{xx}$  is a Toeplitz matrix, its inversion can be done computationally efficient using the Levinson-Durbin recursion [18]. This approach is of special importance when linear prediction is concerned (cf. Section 2.3.4), which will be shown later on to be closely related to AR models.

### 2.3.3 Spectral Estimation of Deterministic Signals

The above considerations deal with arbitrary, unknown signals with intrinsic randomness. Therefore, the estimation of the PSD requires the averaging of several observations of the signal. Deterministic signals are well-defined for any time. This enables an equivalent and unique representation of such signals with an infinite number of (orthogonal) basis function e.g. using the Fourier transform [20]

$$S(\omega) = \int_{-\infty}^{\infty} s(t) e^{-j\omega t} dt. \quad (2.45)$$

For a signal with a known periodicity of  $T = \frac{1}{2\pi\omega_0}$  the continuous Fourier spectrum amounts to a line spectrum

$$S(k \cdot \omega_0) = c_k \delta(\omega - k\omega_0) = \delta(\omega - k\omega_0) \frac{1}{T} \int_0^T s(t) e^{-jk\omega_0 t} dt, \quad (2.46)$$

with  $c_k$  being the coefficients of the complex Fourier series.

In digital signal processing typically data sampled with  $f_s = \frac{1}{T_s}$  are considered in time limited blocks of length  $T = N \cdot T_s$ . Implying the periodicity  $T$  of the signal leads to the discrete time Fourier series (DTFS) [17]:

$$S(k \cdot \omega_0) = \delta(\omega - k\omega_0) \frac{1}{N} \sum_{n=0}^{N-1} s(n T_s) e^{-j2\pi \frac{kn}{N}} \quad (2.47)$$

The DTFS is often referred to as discrete Fourier transform (DFT), even if this would imply an infinite summation. A computationally efficient implementation of the DFT is the well-known fast Fourier transform [20] (FFT).

The implicit assumption of a periodic repetition of the block data leads to the so-called “leakage effect”, if the signal is not periodic in  $T$ . A common technique to trade-off the spectral leakage against resolution is the weighting of the block data with a suitable window functions. A discussion and comparison of the different kinds of window functions can be found in many textbooks [18, 17, 20].

### 2.3.4 Enhancing the Resolution using Linear Prediction

Linear prediction is a technique well-known from voice coding [21]. The underlying deterministic signal model is closely related to AR models for random processes. The difference is that for the linear prediction of deterministic signals the model input is also deterministic (e.g. a Dirac pulse or pulse train) instead of white noise. For the following considerations the model input is assumed to be a Dirac pulse. Hence, for all times greater than zero the time delay stages in the model hold the last  $N$  output samples, that means, that the next output sample is generated as a linear combination of its preceding samples. Consequently, the predictor filter is an  $N$ th order finite impulse response filter as shown in Fig. 2.10. In this viewgraph the predictor filter is fed with the original data and the pre-

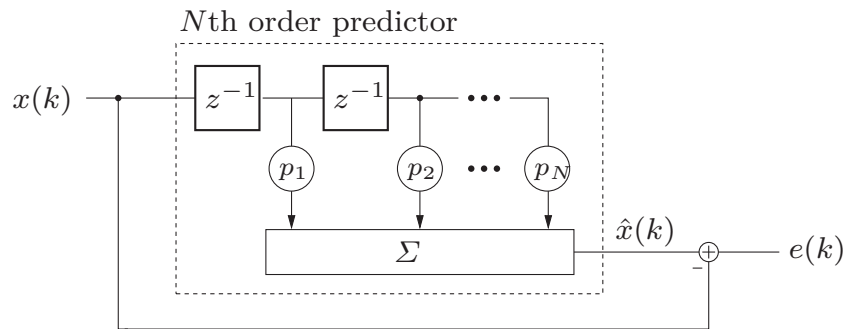


**Fig. 2.10:** Prediction error filter consisting of the  $N$ th order linear predictor and a comparison of the predicted signal  $\hat{x}(k)$  and the actual signal  $x(k)$ ; the output signal of the filter is the prediction error  $e(k)$ .

dicted samples are compared with the actual ones. Thus the resulting overall filter is called prediction error filter. Following [18, 17] the optimum predictor coefficients  $p_\nu$  are obtained by minimising the variance of the predictor error [18] or the output power of the prediction error filter, respectively. Again, the

derivation is just outlined, as the details can be found in the references stated above.

According to Fig. 2.10 the prediction error is

$$e(k) = x(k) - \sum_{\nu=1}^N p_{\nu} \cdot x(k - \nu). \quad (2.48)$$

It is helpful to define the auxiliary vectors

$$\mathbf{x}(k^-) = \begin{bmatrix} x(k-1) \\ x(k-2) \\ \vdots \\ x(k-N) \end{bmatrix} \quad \text{and} \quad \bar{\mathbf{p}} = \begin{bmatrix} p_1^* \\ p_2^* \\ \vdots \\ p_N^* \end{bmatrix}, \quad (2.49)$$

with  $\overline{(\cdot)}$  denoting the elementwise complex conjugate. Using these abbreviations the noise variance to be minimised is

$$\begin{aligned} \sigma_e^2 &= \mathcal{E}\{e(k) e^*(k)\} \\ &= \mathcal{E}\{[x(k) - \bar{\mathbf{p}}^H \mathbf{x}(k^-)] \cdot [x^*(k) - \mathbf{x}^H(k^-) \bar{\mathbf{p}}]\} \\ &= \sigma_x^2 - \bar{\mathbf{p}}^H \mathcal{E}\{\mathbf{x}(k^-) x^*(k)\} - \mathcal{E}\{x(k) \mathbf{x}^H(k^-)\} \bar{\mathbf{p}} \\ &\quad + \bar{\mathbf{p}}^H \mathcal{E}\{\mathbf{x}(k^-) \mathbf{x}^H(k^-)\} \bar{\mathbf{p}}. \end{aligned} \quad (2.50)$$

The elementwise complex conjugate of the autocorrelation matrix of  $x(k)$  is

$$\bar{\mathbf{R}}_{xx} = \mathcal{E}\{\mathbf{x}(k^-) \cdot \mathbf{x}^H(k^-)\}. \quad (2.51)$$

In the same way

$$\bar{\mathbf{r}}_{xx} = \mathcal{E}\{x^*(k) \cdot \mathbf{x}(k^-)\} \quad (2.52)$$

can be derived. Finally taking the complex conjugate of both sides of (2.50) gives the closed matrix formulation of the minimisation problem

$$\sigma_e^2(\mathbf{p}) = \mathbf{p}^H \mathbf{R}_{xx} \mathbf{p} - \mathbf{p}^H \bar{\mathbf{r}}_{xx} - \mathbf{r}_{xx}^H \mathbf{p} + \sigma_x^2 \stackrel{!}{=} \min. \quad (2.53)$$

The direct solution of this complex quadratic matrix equation is obtained by taking the first derivative with respect to  $\mathbf{p}$

$$\frac{d\sigma_e^2(\mathbf{p})}{d\mathbf{p}} = 2\mathbf{R}_{xx} \mathbf{p} - 2\bar{\mathbf{r}}_{xx} \stackrel{!}{=} \mathbf{0}, \quad (2.54)$$

yielding the well-known Wiener-Hopf equation [18]:

$$\mathbf{p} = \mathbf{R}_{xx}^{-1} \mathbf{r}_{xx} \quad (2.55)$$

The concept of linear prediction can be used to extrapolate a finite signal using a so-called synthesis filter. This filter basically is an AR model with  $\mathbf{a} = -\mathbf{p}$ . Again the time delay stages hold the last  $N$  known samples of  $x(k)$  whereas the input of the synthesis filter is zero. The prediction filter in the feedback path now recursively generates new output samples. The statistical properties of these synthetic samples are related to the properties of the known data in that sense, that the  $N$  first autocorrelation lags are equal.

In order to obtain a stable synthesis filter, the prediction error filter has to be a minimum phase filter. That means that its zeros have to be located inside the unit circle in the complex domain. This will be the case if the autocorrelation sequence needed for the calculation of  $\mathbf{p}$  is exactly known. Practical applications usually deal with limited datasets. That means, that the correlation matrix has to be estimated. Some estimation techniques are summarised in the Appendix A.4 on page 131 and rely on a different assumption regarding the signal outside the known interval. Solving the Wiener-Hopf equation based on these estimates either leads to systematical errors in the calculation of the filter coefficients (windowed estimate, so-called Yule-Walker method) or an eventually unstable synthesis filter (non-windowed case or covariance method).

### Burg's Method

As Burg's method is the most frequently used algorithm to obtain AR coefficients, it shall be mentioned shortly. Details can be found e.g. in [18] and [17].

Autocorrelation matrices always have a hermitian structure. Hence, instead of solving the Wiener-Hopf equation by a direct inversion it is also possible to use the more efficient Levinson-Durbin recursion [18]. When replacing the transversal prediction error filter depicted in Fig. 2.10 with the equivalent lattice structure, it can be shown that for each iteration of the Levinson-Durbin recursion one additional stage or order of this lattice filter is obtained, while the previous stages remain unchanged. However, the above mentioned problems in case of correlation estimates still remain.

Burg's method exploits the fact, that the lattice structure provides the forward prediction error *and* the backward prediction error. It is explained e.g. in [18] that a stable synthesis filter is ensured in any case by jointly minimising those two errors.

As an example the time domain data of an FM-CW measurement have been extrapolated using a linear predictor obtained by Burg's method. Figure 2.11 shows the impact of linear prediction on the signal in time and frequency domain.

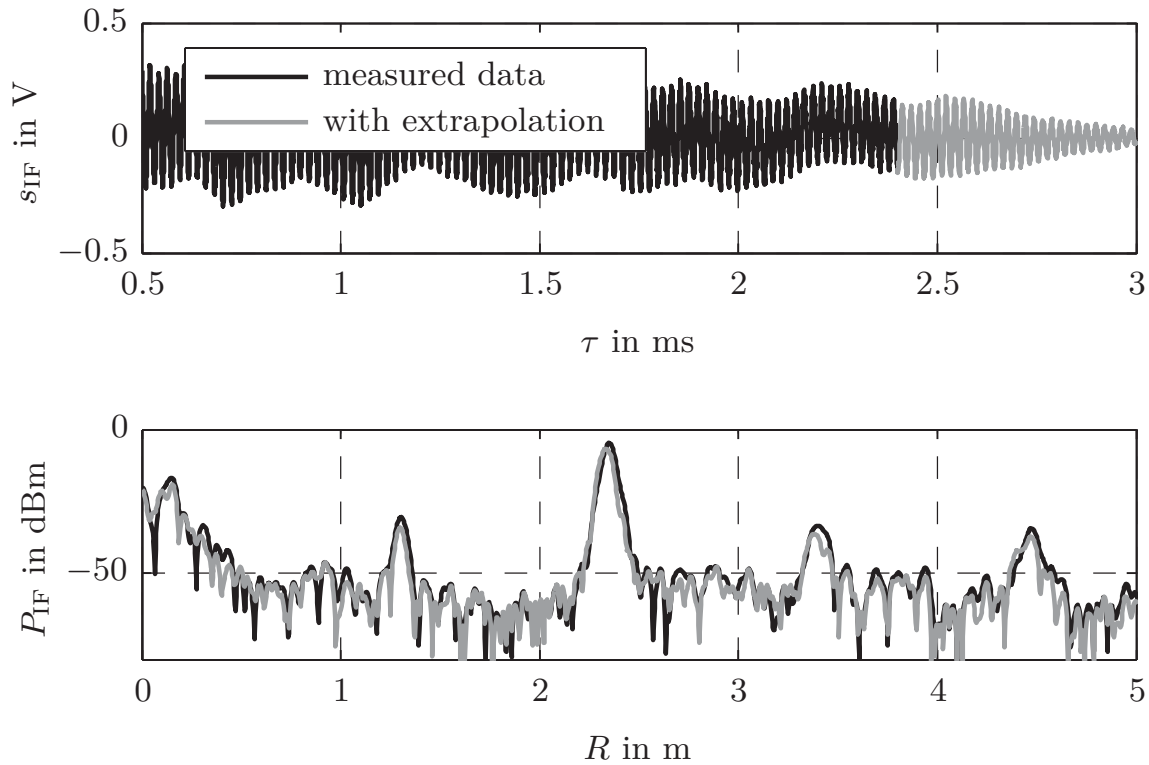


**Fig. 2.11:** IF time domain signal of an FM-CW radar (top) and respective range profile (bottom) for measured and extrapolated data.

The time domain signal is continuously extrapolated. Furtheron it decays, which indicates that the prediction filter is stable. As the overall observation time of the signal is extended, an improved resolution can be recognised in the spectrum.

### 2.3.5 Eigenanalysis-based Techniques

In addition to model-based spectral estimation methods, there are approaches that rely on the eigen-structure of the autocorrelation matrix. Later on it will be demonstrated that the direction of arrival (DOA) finding problem is closely related to spectral estimation. Especially if it comes to uniform linear arrays (ULAs), the above mentioned techniques are directly applicable. However, some of the eigenanalysis based algorithms are also useful for arbitrary arrays or non-uniform sampling. In order to incorporate these cases, a more general formulation of the problem is required. Hence, eigenanalysis based techniques are introduced in conjunction with digital beamforming in Section 2.6.

## 2.4 Wideband Calibration of FM-CW Sensors

In the strict sense the modulation terms in the mathematical representation of an FM-CW radar's IF signal (2.26) are depending on the round trip delay  $\Delta T$ . As the intermediate frequency is typically very small compared to the sweep bandwidth, the approximations

$$\begin{aligned} H_{\text{TX}}(\omega(\tau)) &\sim H_{\text{TX}}(\omega(\tau - \Delta T)), \\ H_{\text{RX}}(\omega(\tau)) &\sim H_{\text{RX}}(\omega(\tau - \Delta T)) \end{aligned} \quad (2.56)$$

are allowed in most cases. For the following considerations it is convenient to use the analytic signal  $s_{\text{IF}}^a(t)$  for which the relation

$$s_{\text{IF}}(\tau) = \text{Re}\{s_{\text{IF}}^a(\tau)\} \quad (2.57)$$

is true. In the practical implementation the Hilbert transform

$$s_{\text{IF}}^a(\tau) = \mathcal{H}\{s_{\text{IF}}(\tau)\} \quad (2.58)$$

is used to derive the analytical signal from a real valued signal. Basically, the IF signal of FM-CW radars is perturbed by two effects. The first one is the dispersion as covered in (2.26). Especially at close ranges there is an additional effect called "ringing". This term summarises all undesired signals caused by internal coupling or reflections e.g. at waveguide flanges or antennas.

Incorporating both effects in (2.26) while neglecting noise and constant phase terms yields

$$s_{\text{IF}}^a(\tau) = A(\omega(\tau))e^{\phi(\omega(\tau))} e^{j2\pi S\Delta T} + e^{\phi(\omega(\tau))} + s_0(\tau), \quad (2.59)$$

where  $A(\omega(\tau))e^{\phi(\omega(\tau))}$  describes dispersion and  $s_0(\tau)$  represents the sensor ringing. Once those terms are known it is possible to compensate for all dispersive and ringing effects while maintaining the harmonic term representing the actual target:

$$s_{\text{IF,cal}} = \text{Re} \left\{ \frac{s_{\text{IF}}^a(\tau) - s_0(\tau)}{A(\omega(\tau))e^{\phi(\omega(\tau))}} \right\} \quad (2.60)$$

The determination of the unknown terms can be done by means of calibration, similar to a vector network analyser [15, 22]. In order to obtain these calibration coefficients, several steps are necessary for both offset and dispersion calibration [23]:

- acquisition of calibration measurement,

- optional: time domain extrapolation of the data,
- isolation of the calibration object with an appropriate filter,
- calculation of the coefficients.

The next two sections provide a more detailed view on the calibration procedure.

### 2.4.1 Calibration of the Sensor Ringing or Offset

In a first step the ringing or sensor offset is obtained by letting the sensor radiate into a non-reflecting environment (cf. Fig. 2.12). In the optimum case this might

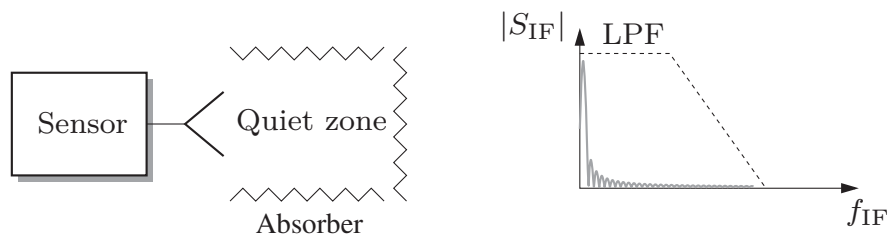


**Fig. 2.12:** Setup for calibrating the sensor offset (left); IF spectrum and frequency response of the lowpass filter used for range gating (right).

be an anechoic chamber. However, as the ringing mainly occurs at very short distances and consequently low IF frequencies, it can be isolated by means of low pass filtering. Depending on the environment this filter may require a high order and low cut off frequency. Therefore, settling effects can influence the precision of the calibration. It was found to be advantageous to extrapolate the measured data in both directions prior to filtering using linear prediction (cf. Section 2.3.4).

A second aspect that has to be considered is the frequency response of the filter. To achieve a perfect cancellation when applying the calibration, the filter must not affect the amplitude or phase for the frequencies of interest. Butterworth filters provide a flat response but due to causality they cannot have a zero phase. The solution is to process the data forward and backward [24], which in consequence doubles the filter order and equalises the phase.

### 2.4.2 Correction of the Signal Dispersion

The calibration measurement required for the compensation of dispersive effects is done in a similar way. As shown in Fig. 2.13 a target with a large radar

cross section is positioned in free space with a sufficient distance to any other reflective object. In addition, a range gating should be applied to isolate the

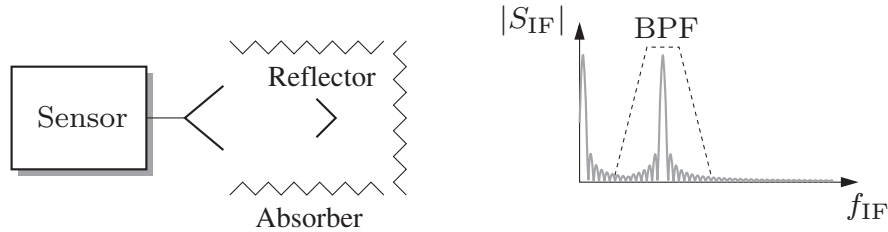


**Fig. 2.13:** Setup for calibrating the sensor dispersion (left); IF spectrum and frequency response of the bandpass filter used for range gating (right).

contribution of the calibration object. Again, this is done by digitally bandpass filtering the IF signal, where the use of zero phase filters is mandatory due to the before mentioned reasons.

Figure 2.15 shows the effect of both offset and dispersion calibration on a measured range profile acquired with an FM-CW sensor operating from 74 GHz to 81 GHz. The effect of offset calibration can be observed in the time domain as well as in the range or frequency domain. The low frequency signal contents caused by the sensor ringing are suppressed by 40 dB. Using this kind of calibration close targets can be detected that would otherwise have been covered by the ringing.

Regarding dispersion the uncalibrated measurement shows an asymmetric point spread function and a sidelobe level higher than the window function used in the experiment would imply (Chebyshev window with 60 dB sidelobe suppression). By calibration both aspects are clearly improved.

Even though the calibration coefficients are obtained using the approximation  $\omega(\tau) \simeq \omega(\tau - \Delta T)$  it has been shown that they are applicable for a large range of distances  $R$  or time delays  $\Delta T$ , respectively.

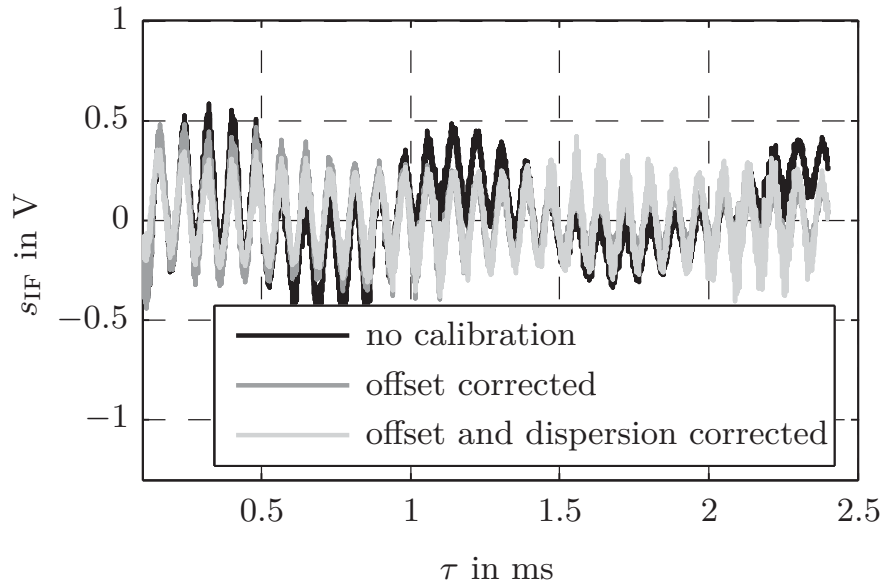


**Fig. 2.14:** Time domain signals obtained by using the different calibration schemes.

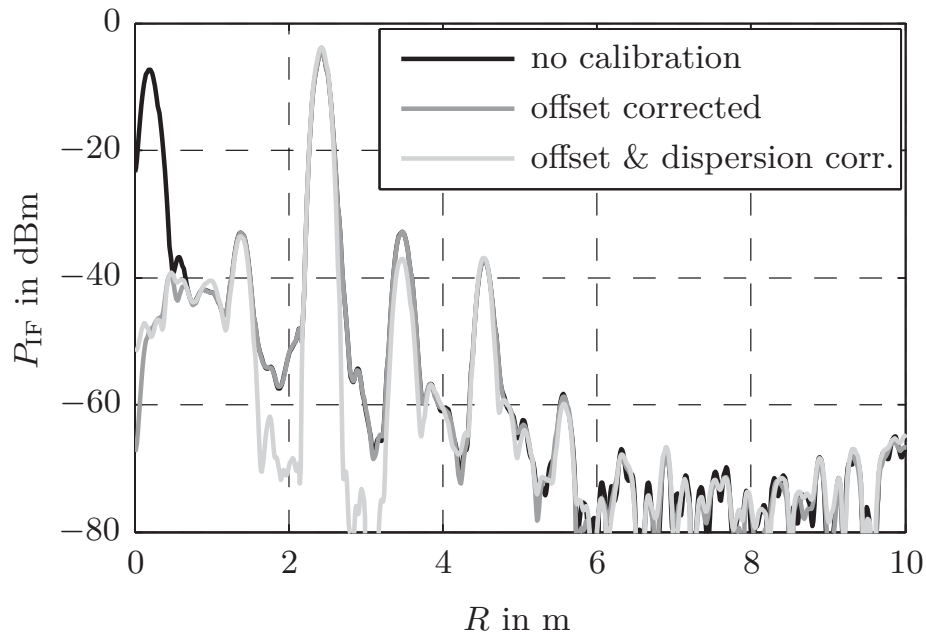


**Fig. 2.15:** Range profiles obtained by using the different calibration schemes.

## 2.5 Doppler Processing and Velocity Measurement

In addition to the range, velocity or Doppler shift is the second target feature that can be obtained by radar measurements. In general, any Doppler shift of the received signal also leads to a change of the frequency at the output of the receiver. As this frequency is also used for determining the range, there is an ambiguity that has to be resolved.

For the mathematical analysis two different time bases have to be distinguished:

- “fast” time  $\tau$ , which is related to the start of each pulse,
- “slow” time  $t$ , which is the absolute timebase.

Considering the target motion, the round trip delay becomes time dependent:

$$\Delta\tilde{T}(t) = \Delta T + 2\frac{vt}{c_0} \quad (2.61)$$

Incorporating this term in (2.26) and neglecting phase noise and dispersive effects results in the following baseband description for a moving target:

$$\begin{aligned} s_{\text{IF}}(t, \tau) &= A \cdot \cos\left(2\pi S \Delta\tilde{T}(t) \cdot \tau + \omega_0 \Delta\tilde{T}(t) - \pi S \Delta\tilde{T}^2(t)\right) \\ &= A \cdot \cos\left(2\pi\left(S \Delta T + \underbrace{2S \frac{v \cdot t}{c_0}}_{\text{frequ. migration}}\right)\tau + \underbrace{2\omega_0 \frac{v \cdot t}{c_0}}_{\text{Doppler shift}}\right. \\ &\quad \left. + \omega_0 \Delta T - \pi S \Delta T^2 - 2\pi S \Delta T \frac{v \cdot t}{c_0} - 4\pi S \frac{v^2}{c_0^2} t^2\right) \end{aligned} \quad (2.62)$$

As expected the target motion leads to a Doppler shift. In addition the frequency of the baseband signal is migrating over the slow time  $t$ , as the target distance changes with time. However, it is presumed that the target remains within the same range cell during the whole measurement. Hence, the latter effect is negligible. The same is true for most of the constant or slowly changing phase terms. As a result (2.62) can be simplified:

$$s_{\text{IF}}(t, \tau) \approx A \cdot \cos\left(2\pi S \Delta T \tau + 2\omega_0 \frac{v \cdot t}{c_0} + \omega_0 \Delta T - \pi S \Delta T^2\right) \quad (2.63)$$

The ambiguity of range and Doppler shift can be resolved by changing the parameters  $S$  and  $t$  and solving the resulting system of equations for  $R$  and  $v$ .

Many different techniques are known from literature. The choice depends on system requirements such as:

- multi-target capability,
- measurement of Doppler spectrum,
- maximum Doppler shift,
- minimum Doppler shift or Doppler resolution.

In the following sections an overview of different methods is given and their properties and limitations are discussed.

### 2.5.1 Resolving Range Doppler Ambiguities by Triangular Modulation

A typical approach to resolve range and Doppler shift is using a triangular frequency modulation (cf. Fig. 2.16). Due to the Doppler shift  $f_d = 2 \cdot f_0 \frac{v}{c_0}$  the observed intermediate frequencies are different during the positive or negative slope:

$$f_{IF,1A} = \frac{2 \cdot S_1}{c_0} R - f_d = f_r - f_d n, \quad (2.64)$$

$$f_{IF,1B} = \frac{2 \cdot S_1}{c_0} R + f_d = f_r + f_d \quad (2.65)$$

Once these frequencies are measured, the range and Doppler related contributions  $f_r$  and  $f_d$  are obtained by solving the linear system of equations.

In case of two targets it may be difficult to assign the measured frequencies to the respective targets. Therefore, the solution is ambiguous. Figure 2.17 shows a graphical representation of this ambiguity. Each line represents possible combinations of range and Doppler for the respective measurements. In case of one target all the four lines are intersecting in one single point. This means, that the second pulse is adding redundant information. In a two target scenario, intersections occur where no targets are located. Hence, the additional information due to the second pulse is required to identify ghost targets and resolve the

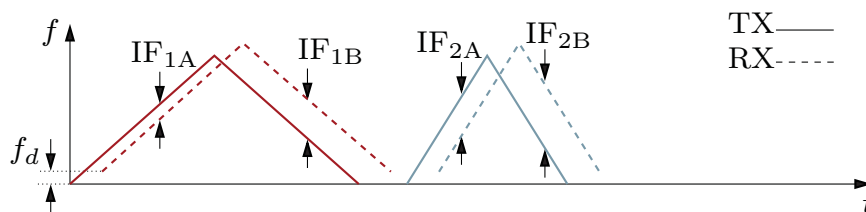


**Fig. 2.16:** Triangular modulation scheme for resolving range Doppler ambiguities.

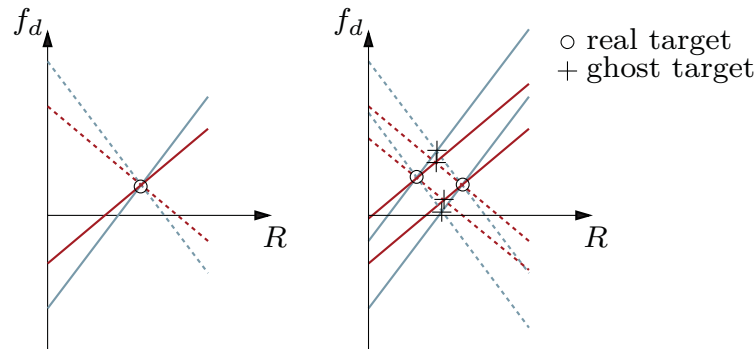


**Fig. 2.17:** Ambiguity of range and Doppler for one target (left) and two targets (right); the colours are in accordance to Fig. 2.16, solid lines are related to the positive slope and dashed lines to the negative slope of the triangular frequency modulation.

ambiguity. Generally spoken, at least one triangular FM-CW pulse per target has to be processed to obtain all the range and Doppler information without ambiguities or ghost targets.

### 2.5.2 Phase Processing of Pulse Trains

In the last section the slope  $S$  of the frequency modulation has been changed to resolve the range Doppler ambiguity. Thereby, only the frequency of the IF signal has been considered. This works well in situations where the Doppler shift can be resolved by the FM-CW range processing. For very small target velocities this may not be possible. Alternatively, two measurements can be acquired at different times  $t_1$  and  $t_2$  using the same slope  $S$  (cf. Fig. 2.18). According to (2.63) the phase observed in the baseband changes, if a Doppler shift is present. This phase shift relates to the velocity like

$$\Delta\Phi = \Phi_2 - \Phi_1 = 2\omega_0 \frac{v}{c_0} (t_2 - t_1). \quad (2.66)$$

The waveforms may be transmitted either sequentially or even intertwined [25, 26]. In the latter case, practical implementations use time domain multiplexing between two linear frequency modulated pulses or SF-CW signal generation with appropriate frequency steps (cf. Fig. 2.5)

The phase processing approach can be further extended using a pulse train of multiple FM-CW waveforms (cf. Fig. 2.20).

For slowly moving targets the slow time  $t$  in (2.63) is assumed to be constant during a single FM-CW pulse. Furtheron  $\Delta T$  does not change significantly

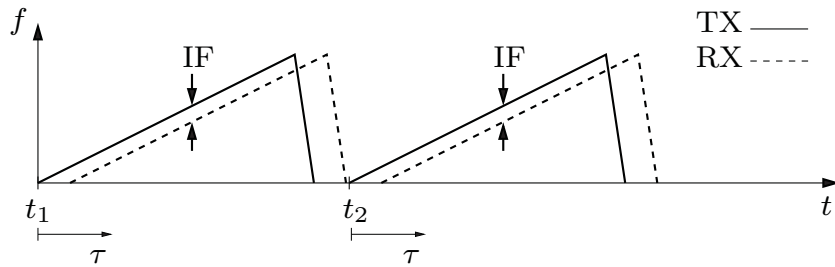


**Fig. 2.18:** Acquisition of two subsequent FM-CW pulses for Doppler processing.

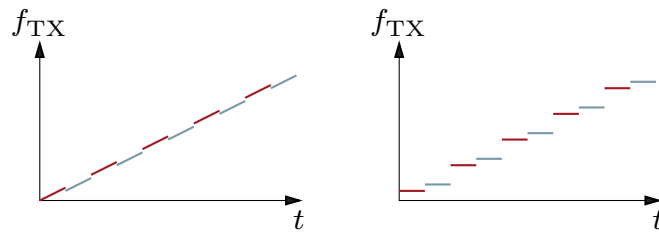


**Fig. 2.19:** Intertwined acquisition of two FM-CW pulses for Doppler processing; the multiplexed red and blue sections result in two slightly time-shifted waveforms.

during the complete pulse train. Consequently, the intermediate frequency is the same for each pulse. However, with respect to the slow time  $t$  a linear phase slope can be observed, that is only related to the target Doppler.

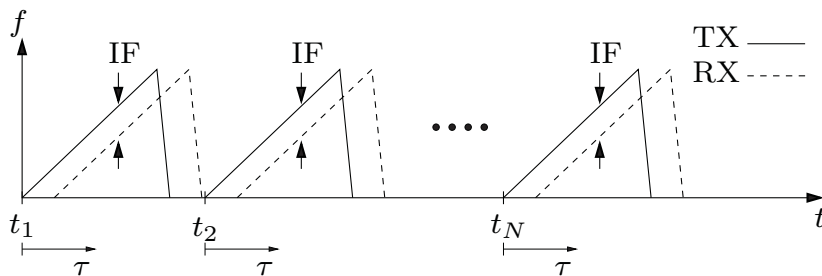


**Fig. 2.20:** Acquisition of multiple equal FM-CW pulses for the calculation of the two dimensional range Doppler spectrum.

As the Doppler signal is sampled for each radar pulse at  $t_n = n \cdot T_{s,d}$ , the maximum unambiguous Doppler frequency or target velocity is determined according to Nyquist's theorem:

$$v_{\max} = \frac{f_{d,\max} c_0}{2 f_0} = \frac{c_0}{4 \cdot T_{s,d} f_0} \quad (2.67)$$

The resolution of the Doppler shift  $\Delta f_d$  or the target velocity  $\Delta v$  is related to the inverse of the overall observation time  $N T_{s,d}$ :

$$\Delta v = \frac{\Delta f_d c_0}{2 f_0} = \frac{c_0}{2 N T_{s,d} f_0} \quad (2.68)$$

A two dimensional range Doppler spectrum is obtained by a Fourier transform with respect to fast time  $\tau$  (range) and slow time  $t$  (Doppler). Figure 2.21 shows the simulation of a scenario with four targets with different ranges and velocities.

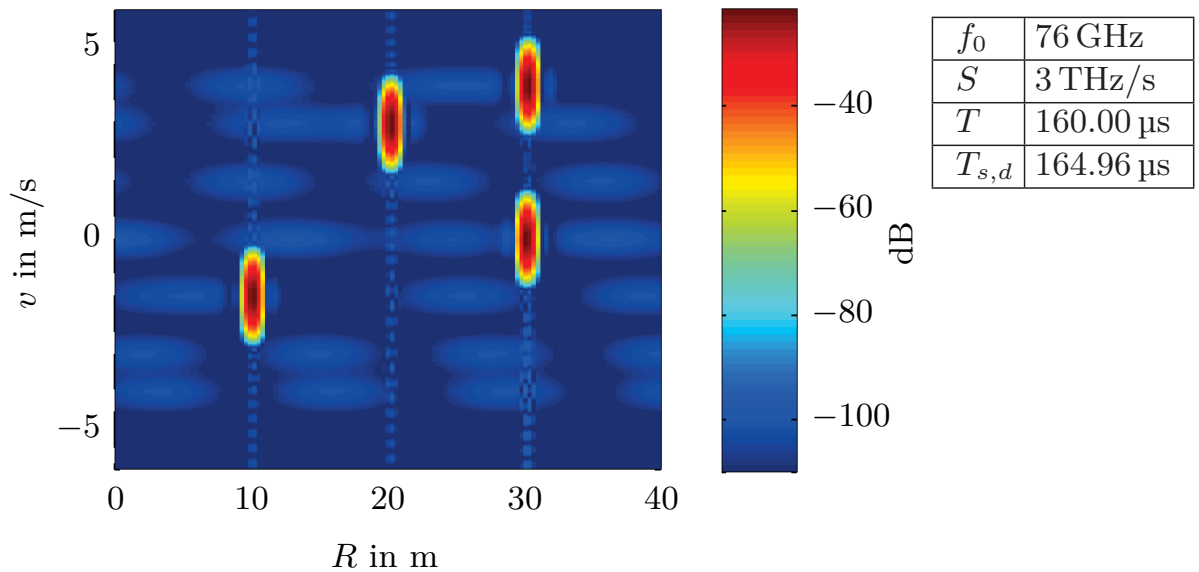


**Fig. 2.21:** Example of a two dimensional range Doppler spectrum (left); parameters used for the simulation (right).

## 2.6 Digital Beamforming

Generally, beamforming is the task of finding a suitable weighting and superposition of spatially distributed receivers to synthesise a desired pattern for the overall array [27]. Depending on the application, certain side conditions such as angular resolution, sidelobe attenuation or interferer suppression may be important. The basic building blocks of a beamforming receiver system are depicted in Fig. 2.22. Antennas sample the incident electric field  $E_{\text{in}}$  at given locations. Receivers and down converters provide voltages  $x_m$  that are proportional to this field. After an analogue-to-digital conversion (ADC) a numerical representation of these voltages is available for the further processing. Using a vector notation for the signals  $x_m$  and the angle dependent weighting factors  $w_m^*$ , the beamforming process can be written as

$$\mathbf{y}(\theta_n) = \mathbf{w}^H(\theta_n) \mathbf{x}, \quad (2.69)$$

where the superscript  $H$  represents the complex conjugate transpose (hermitian) of a vector or matrix. Incorporating the so-called steering vectors  $\mathbf{w}$  for all angles of interest into one single matrix  $\mathbf{W}$  leads to the even more compact notation

$$\mathbf{y} = \begin{bmatrix} w_1(\theta_1) & w_1(\theta_2) & \dots & w_1(\theta_N) \\ w_2(\theta_1) & w_2(\theta_2) & \dots & w_2(\theta_N) \\ \vdots & \vdots & \vdots & \vdots \\ w_M(\theta_1) & w_M(\theta_2) & \dots & w_M(\theta_N) \end{bmatrix}^H \mathbf{x} = \mathbf{W}^H \mathbf{x}. \quad (2.70)$$

As a result, the  $n$ th element of the vector  $\mathbf{y}$  is the response of the beamformer for the respective angle  $\theta_n$ .

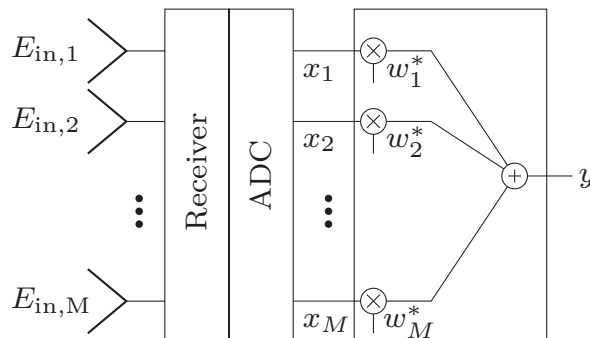


**Fig. 2.22:** General block diagram of a beamforming system.

All important beamforming techniques are based on signal models [28]. In the next section a data model is derived that serves as a basis for all of the approaches described afterwards.

### 2.6.1 Narrow Band Data Model

In most of the literature on digital beamforming [28, 29, 30] a narrow band model is used to mathematically describe the relationship between a source distribution and the response at the output of a sensor array. This kind of model exploits the fact, that for narrow band systems a time delay can be expressed in terms of a phase shift. Assume an arbitrary sensor array consisting of  $M$  receivers located at the positions  $\mathbf{r}_m = (r_{m,x} \ r_{m,y})^T$  and a number  $N$  of plane waves impinging on this array (Fig. 2.23). These waves may originate from either active sources or by reflecting the signal of a radar transmitter. The direction of arrival (DOA) and the propagation constant are described using the wave number vector

$$\mathbf{k}_n = -\frac{2\pi}{\lambda} \cdot \begin{bmatrix} \cos \theta_n \\ \sin \theta_n \end{bmatrix}^T. \quad (2.71)$$

According to Fig. 2.23 the incident electric field at the point  $\mathbf{r}_m$  induced by a wave with the complex amplitude  $s_n$  and the wave number vector  $\mathbf{k}_n$  is

$$E_{\text{in}} = s_n \cdot e^{j(\omega t - \mathbf{k}_n \cdot \mathbf{r}_m)}. \quad (2.72)$$

As signal processing is usually done in the baseband, the term  $\omega t$  is dropped during the down-conversion process. Due to linearity, the output signal of the  $m$ th receiver is given by the superposition of all sources  $s_n(\theta_n)$

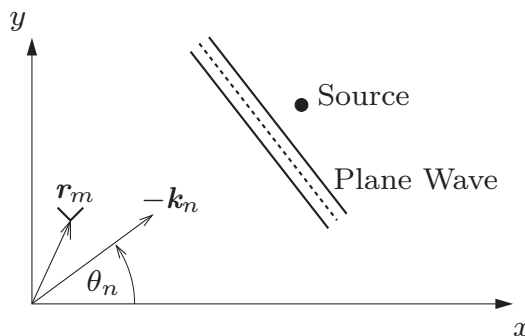


**Fig. 2.23:** Geometrical definition of source, receiver location  $\mathbf{r}_m$ , and wave number vector  $\mathbf{k}_n$ .

$$x_m = \sum_{n=1}^N g_m(\theta_n) e^{-jk_n \cdot r_m} s_n(\theta_n) = \sum_{n=1}^N a_m(\theta_n) s_n(\theta_n), \quad (2.73)$$

where  $g_m(\theta_n)$  is a weighting factor describing the directivity of the receiver.

Considering all sources and receivers leads to the following matrix equation, commonly referred to as narrowband data model or array manifold [28]:

$$\mathbf{x} = \begin{bmatrix} a_1(\theta_1) & a_1(\theta_2) & \dots & a_1(\theta_N) \\ a_2(\theta_1) & a_2(\theta_2) & \dots & a_2(\theta_N) \\ \vdots & \vdots & \vdots & \vdots \\ a_M(\theta_1) & a_M(\theta_2) & \dots & a_M(\theta_N) \end{bmatrix} \begin{bmatrix} s_1(\theta_1) \\ s_2(\theta_2) \\ \vdots \\ s_N(\theta_N) \end{bmatrix} = \mathbf{A} \mathbf{s} \quad (2.74)$$

Analysing the structure of the matrix  $\mathbf{A}$ , one can see that the  $n$ th row of the matrix contains the response of the array to a plane wave incident from the DOA  $\theta_n$ .

This approach using a limited number of discrete sources can be generalised to handle arbitrary and even continuous source distributions  $\mathbf{s}(\theta)$  by setting up  $\mathbf{A}$  for all angles of interest.

In the strict sense the above model is only valid for single frequency continuous wave (CW) systems. For range resolution in radars a modulation of the carrier signal is mandatory. However, for sufficiently narrowband signals the model is still applicable, as long as the maximum extent of the array measured in wavelengths is smaller than the inverse relative bandwidth of the signal [28]:

$$L_{\text{array}}/\lambda_0 < f_0/B_{\text{signal}} \quad (2.75)$$

In other words the array extents must not be resolved by the radar waveform. This condition can be relaxed if the field of view is limited. This is because the projection of the array on the propagation vector of the considered waves is the relevant figure. Possible extensions for wideband systems will be given in Section 2.6.6.

## 2.6.2 Conventional Beamformers

Data independent beamformers (also known as conventional or Bartlett beamformers) exploit only the underlying data model without incorporating properties of the actual measured data (e.g. the correlation matrix). For each angle

of interest a so-called beam steering vector is determined, containing the beamforming weights  $w_n^*$ . To maximise the sensitivity of the array towards an angle  $\theta$ , the weights have to be chosen as [28]

$$\mathbf{w}(\theta) = \frac{\mathbf{a}(\theta)}{\sqrt{\mathbf{a}^H(\theta) \mathbf{a}(\theta)}}. \quad (2.76)$$

For convenience, it is common practise to state the vector  $\mathbf{w}(\theta)$  even if the beamformer uses the complex conjugate of this vector (cf. Fig. 2.22). Keeping in mind that the output of the beamformer is

$$\mathbf{y} = \mathbf{W}^H \mathbf{x} = \mathbf{W}^H \mathbf{A} \mathbf{s} \quad \text{or} \quad y(\theta) = \frac{\mathbf{a}^H(\theta)}{\sqrt{\mathbf{a}^H(\theta) \mathbf{a}(\theta)}} \mathbf{A} \mathbf{s}, \quad (2.77)$$

it is obvious that the beam steering vector is a matched filter, as the columns of  $\mathbf{W}$  are composed of the normalised columns of  $\mathbf{A}$ . To give an intuitive explanation, the multiplication with the complex conjugate transpose  $\mathbf{a}_n^H(\theta)$  equalises the phase shifts for a DOA of  $\theta$ . Hence, the contributions of all elements add up in phase. The normalisation by the denominator in (2.76) ensures a unity response for all angles.

The derivation of the steering matrix  $\mathbf{W}$  in case of a uniform linear array (ULA) gives an interesting insight into the properties of a conventional beamformer. For simplicity isotropic antennas are used in the example. The positions of the  $M$  antennas are  $\mathbf{r}_m = [(m-1)d \ 0]^T$  within a coordinate system as in Fig. 2.23, where  $d$  is the spacing between the elements. According to (2.73) the data model is

$$\mathbf{a}_{\text{ULA}}(\theta_n) = \left[ 1 \quad e^{jk_0 d \cos \theta_n} \quad \dots \quad e^{jk_0 m d \cos \theta_n} \right]^T. \quad (2.78)$$

Thereby, it is convenient to introduce the spatial angular frequency  $u = k_0 \cos \theta$  that is directly related to the angle of incidence and yields a more compact notation:

$$\mathbf{a}_{\text{ULA}}(\theta_n) = \left[ 1 \quad e^{ju(\theta_n)d} \quad \dots \quad e^{jm u(\theta_n)d} \right]^T \quad (2.79)$$

Thus, the response of an ULA to incident plane waves is a superposition of harmonic functions, the frequencies of which depend on the angles of incidence. Hence, the conventional beamformer is the vector notation of a discrete Fourier transform that may be implemented as an FFT. According to Section 39 the resolution of the spatial angular frequency  $\Delta u$  is given by the array size  $L_{\text{array}} = n d$  as

$$\Delta u = 2\pi \cdot \frac{1}{L_{\text{array}}}. \quad (2.80)$$

Using the nonlinear relation between spatial frequency and angle of incidence

$$|\Delta u| = k_0 |\sin \theta \cdot \Delta \theta| = 2\pi \cdot \frac{|\sin \theta \cdot \Delta \theta|}{\lambda} \quad (2.81)$$

yields an angular resolution in radians of

$$|\Delta \theta| = \frac{\lambda}{L_{\text{array}} \cdot |\sin \theta|}. \quad (2.82)$$

That means that the angular resolution depends on the size of the array measured in wavelength and the steering angle. The optimum performance is obtained in case of a boresight beam ( $|\sin \theta| = 1$ ) and degrades for off-axis angles. A factor of 2 is reached for an off-boresight angle of  $60^\circ$ , which is often used as the maximum steering angle. The relation stated above is valid for a uniform weighting of the antenna elements. In case of windowing the same modifications apply as for spectral estimation (cf. Section 39).

As another consequence of the duality time/frequency and space/angle, any other spectral estimation method is suited as beamformer or DOA estimator. Two well-known candidates from this field (originally developed as DOA estimators) are MUSIC [29] and ESPRIT [30].

### 2.6.3 Correlation Matrix in Beamforming Applications

Most of the advanced spectral estimation techniques rely on the statistical properties of the array output signals, namely the correlation matrix. It should be mentioned that in literature the terms covariance and correlation are often used synonymously. In the strict sense this is only allowed if the mean value of all data is known to be zero. Obviously, this is not the case if the output signal of an ULA is considered for a plane wave impinging from boresight direction. Consequently, the term correlation is preferred in this work.

As shown in Appendix A.4 on page 131 the autocorrelation matrix is approximated by estimating the expectation:

$$\mathbf{R} = \mathcal{E} \left\{ \mathbf{x}\mathbf{x}^H \right\} \quad (2.83)$$

This implies an averaging of linear independent samples of  $\mathbf{x}\mathbf{x}^H$ .

In the context of beamforming, DOA and radar applications have to be distinguished. DOA estimators typically aim to locate uncorrelated sources in the angular domain. Hence,  $\mathbf{R}$  can be obtained by averaging in the time domain:

$$\mathbf{R} = \mathcal{E} \left\{ \mathbf{x}(t)\mathbf{x}(t)^H \right\} \quad (2.84)$$

In radar systems the angular spectrum has to be estimated for each range resolution cell, but after the range processing only one single complex value is available per range and channel. Hence, temporal averaging is no longer applicable. Even if the received waveforms would be used *before* range processing, this approach would fail, as the impinging signals are highly correlated.

The solution is to divide the physical array into identical but translated sub-arrays and perform the averaging in the spatial domain. Consequently, this process is called spatial smoothing [28]. Having in mind that incoming plane waves lead to an array response consisting of complex harmonic signals in the spatial domain (cf. (2.79)), this approach is quite natural as it is used for harmonic signals in the time domain as well (cf. Appendix A.4 on page 131). However, this fact is rarely stressed in literature, even though it limits the radar based application of many algorithms to an array arrangement that allows spatial smoothing such as ULAs or at least arrays having a fully populated coarray. The coarray concept will be explained in Section 4.3 and used for the estimation of the autocorrelation matrix in case of an ULA with one element not being available.

### 2.6.4 Adaptive Beam Formers

The Bartlett beamformer described in the last section is data independent. That means it requires only the a priori knowledge of the sensor setup and does not exploit the properties of the received signals. This is computationally efficient, as the beamforming weights do not have to be recalculated for each measurement. There is no restriction with respect to the target scenario. As a consequence the  $M$  angular resolution cells obtainable with an  $M$  element sensor correspond to equally spaced spatial frequencies between  $-\frac{2\pi}{\lambda}$  and  $\frac{2\pi}{\lambda}$ . This is not the optimal approach for scenarios with a limited number of point scatterers. In this case data dependent or adaptive beamforming techniques can improve the resolution significantly.

#### Minimum Variance Beamformer

A well-known adaptive DOA estimator is the minimum variance beamformer proposed by Capon [31]. The idea is to minimise the overall output power of the beamformer while maintaining a unity response in case a point source is located at a certain angle of arrival (AOA). This leads to an adaptive and optimum suppression of all signals impinging from any direction beside the angle of interest.

The power at the output of a general beamformer (2.70) is expressed in terms of the variance which is obtained by the expectation

$$P(\theta) = \mathcal{E} \left\{ |y(\theta)|^2 \right\} = \mathcal{E} \left\{ \mathbf{w}^H(\theta) \mathbf{x} \mathbf{x}^H \mathbf{w}(\theta) \right\} = \mathbf{w}^H(\theta) \mathbf{R} \mathbf{w}(\theta), \quad (2.85)$$

where  $\mathbf{R}$  is the correlation matrix of the array output signals which is usually replaced by its estimate  $\hat{\mathbf{R}}$ . Hence, the mathematical formulation of the optimisation problem is:

$$\begin{aligned} & \text{minimise} && \mathbf{w}^H(\theta) \hat{\mathbf{R}} \mathbf{w}(\theta), \\ & \text{subject to} && \mathbf{w}(\theta)^H \mathbf{a}(\theta) = 1 \end{aligned} \quad (2.86)$$

Such kind of problems (optimisation subject to side conditions) can be solved using Lagrange multipliers [32]. The basic idea is to incorporate a scalar constraint into the function to be minimised. For the given situation this yields the so-called Lagrangian

$$L(\mathbf{w}, \lambda) = \mathbf{w}^H \mathbf{R} \mathbf{w} + \lambda \left( \mathbf{w}^H \mathbf{a} - 1 \right), \quad (2.87)$$

that has to be minimised with respect to  $\mathbf{w}$  and  $\lambda$ . Due to the quadratic form of (2.87) the minimum is found with

$$\frac{dL(\mathbf{w}, \lambda)}{d\mathbf{w}} = 2\mathbf{R}\mathbf{w} + \lambda\mathbf{a} \stackrel{!}{=} \mathbf{0}. \quad (2.88)$$

Solving (2.88) for  $\mathbf{w}$  yields

$$\mathbf{w} = -\frac{\lambda \mathbf{R}^{-1} \mathbf{a}}{2}. \quad (2.89)$$

The yet unknown Lagrange multiplier  $\lambda$  has to be chosen such that the constraint  $\mathbf{w}^H \mathbf{a} = 1$  is fulfilled:

$$\lambda = \frac{-2}{\mathbf{a}^H \mathbf{R}^{-1} \mathbf{a}} \quad (2.90)$$

Finally, substituting (2.90) in (2.89) yields the weights of the Capon beamformer

$$\mathbf{w}_{\text{Capon}}(\theta) = \frac{\hat{\mathbf{R}}^{-1} \mathbf{a}(\theta)}{\mathbf{a}^H(\theta) \hat{\mathbf{R}}^{-1} \mathbf{a}(\theta)}. \quad (2.91)$$

In many applications it is desired to derive the angular spectrum of the signals impinging on the array. Instead of applying the beamforming weights to the

array output signals, the minimum variance angular spectrum is obtained more simply by substituting (2.91) into (2.85):

$$P(\theta) = \frac{1}{\mathbf{a}^H(\theta)\mathbf{R}^{-1}\mathbf{a}(\theta)} \quad (2.92)$$

There are also many extensions of the Capon's method [33, 34, 35, 36] taking into account variations or uncertainties of the array response.

It shall be noted that the calculation of adaptive beamforming weights is not only limited to a single unity gain constraint as shown above. Moreover, it is possible to use Lagrange multipliers to force the array sensitivity to zero for certain AOA, e.g. to suppress interferences caused by other sensors or jammers.

## MUSIC

The MUSIC algorithm (MUltiple Signal Classification) was proposed by Schmidt [29] and exploits the internal structure of the correlation matrix using an eigenvalue decomposition. When considering additive noise (2.74) has to be extended to

$$\mathbf{x} = \mathbf{A} \mathbf{s} + \mathbf{n} . \quad (2.93)$$

Thus, the correlation matrix is

$$\begin{aligned} \mathbf{R}_{xx} &= \mathcal{E} \left\{ \mathbf{x}\mathbf{x}^H \right\} \\ &= \mathbf{A} \mathcal{E} \left\{ \mathbf{s}\mathbf{s}^H \right\} \mathbf{A}^H + \mathcal{E} \left\{ \mathbf{n}\mathbf{n}^H \right\} \\ &= \mathbf{A}\mathbf{R}_{ss}\mathbf{A}^H + \sigma^2\mathbf{I} \\ &= \mathbf{R}'_{xx} + \mathbf{R}_{nn} , \end{aligned} \quad (2.94)$$

where  $\sigma^2$  is the variance of the added noise.

If  $M$  is the number of array elements, the matrix  $\mathbf{R}'_{xx}$  has the dimension  $M \times M$ . For a number of targets  $D < M$ , only  $D$  elements of  $\mathbf{s}$  are not zero. It is obvious, that in this case the matrix  $\mathbf{R}'_{xx}$  is rank-deficient. That means, that only  $D$  out of  $M$  eigenvalues are non-zero.

In [21] a very handy way is given to derive the signal and noise related eigenvalues of  $\mathbf{R}_{xx}$ . Consider the eigendecomposition

$$\mathbf{R}'_{xx} = \sum_{k=1}^M \lambda_k \mathbf{e}_k^H \mathbf{e}_k = \sum_{k=1}^D \lambda_k \mathbf{e}_k^H \mathbf{e}_k , \quad (2.95)$$

where  $\lambda_k$  are the eigenvalues and  $\mathbf{e}_k$  the corresponding eigenvectors of  $\mathbf{R}'_{xx}$ . The upper limit of the sum can be  $D$ , as the eigenvalues  $\lambda_{D+1\dots M}$  are all zero.

As  $\mathbf{e}_k$  is a set of  $M$  orthonormal vectors the unity matrix in (2.94) can be expressed as

$$\mathbf{R}_{nn} = \sigma^2 \mathbf{I} = \sigma^2 \mathbf{E}^H \mathbf{E} = \sigma^2 \sum_{k=1}^M \mathbf{e}_k^H \mathbf{e}_k. \quad (2.96)$$

Substituting (2.95) and (2.96) into (2.94) yields

$$\begin{aligned} \mathbf{R}_{xx} &= \sum_{k=1}^D \lambda_k \mathbf{e}_k^H \mathbf{e}_k + \sigma^2 \sum_{k=1}^M \mathbf{e}_k^H \mathbf{e}_k \\ &= \sum_{k=1}^D (\lambda_k + \sigma^2) \mathbf{e}_k^H \mathbf{e}_k + \sigma^2 \sum_{k=D+1}^M \mathbf{e}_k^H \mathbf{e}_k, \end{aligned} \quad (2.97)$$

which is the complete eigendecomposition of  $\mathbf{R}_{xx}$ . One can see that the  $M - D$  smallest eigenvalues are all equal to  $\lambda_{\min} = \sigma^2$  and are therefore called noise eigenvalues. The corresponding eigenvectors span the so-called noise subspace, whereas the remaining eigenvectors span the signal subspace.

The signal subspace contains all the column vectors of the array manifold  $\mathbf{A}$  contributing to the noise free output signal  $\mathbf{x} = \mathbf{A}\mathbf{s}$ . Thus, the DOAs  $\theta_{1\dots D}$  are obtained by identifying those column vectors  $\mathbf{a}(\theta_{1\dots D})$  situated within the signal subspace. Figure 2.24 visualises a three dimensional vector space together with a two dimensional signal subspace spanned by the two signal eigenvectors. The

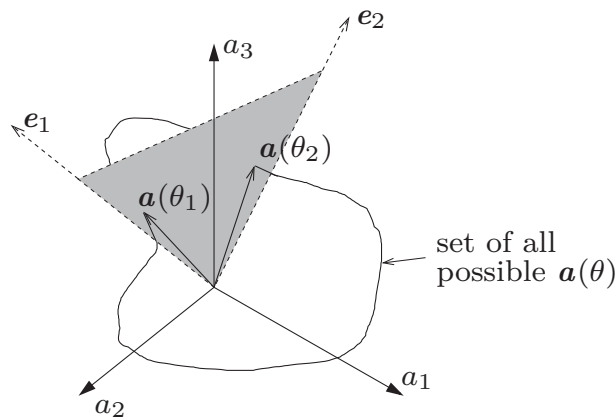


**Fig. 2.24:** Intersection of the array manifold  $\mathbf{a}(\theta)$  and the signal subspace.

set of all possible  $\mathbf{a}(\theta)$  (the array manifold) is depicted as a solid curve within the three dimensions. The intersections of the array manifold and the signal subspace give the  $\mathbf{a}(\theta_k)$  related to the targets' DOA.

Let  $\mathbf{E}_n$  be a matrix containing all noise eigenvectors. An angular pseudospectrum can be derived using the expression

$$P_{\text{MUSIC}}(\theta) = \frac{1}{\mathbf{a}^H(\theta)\mathbf{E}_n\mathbf{E}_n^H\mathbf{a}(\theta)}. \quad (2.98)$$

The denominator of (2.98) is the projection of the array manifold into the noise subspace. This projection is zero for the exact DOAs. Hence, the pseudospectrum tends towards infinity at these angles.

In reality the noise eigenvalues are typically not equal. Hence, a method has to be found to determine the dimensions of the subspaces. A widely used approach is to define a threshold based on the smallest eigenvalue and to limit the maximum dimension of the signal subspace at the same time.

However, when applying the MUSIC algorithm to measured data spurious peaks can occur in the pseudospectrum due to uncertainties in the estimation of the correlation matrix and the dimension of the signal subspace. In a slightly modified version of the MUSIC pseudospectrum, an additional weighting is introduced [37, 17]:

$$P_{\text{MUSIC}}(\theta) = \frac{1}{\sum_{k=D+1}^M |\mathbf{a}^H(\theta)\mathbf{e}_{n,k}|^2 / \lambda_k} \quad (2.99)$$

In the summation term, the projections onto the noise eigenvectors are weighted with the respective eigenvalue. This mitigates spurious peaks in the angular spectrum that are caused by eigenvectors that are wrongly considered being within the noise subspace. Hence, the influence of uncertainties with respect to the data model or the estimation of the correlation matrix and the actual number of targets is less critical.

## ESPRIT

The ESPRIT algorithm (Estimation of Signal Parameters via Rotational Invariance Technique) [38, 30] also exploits the eigenstructure of correlation matrices. In contrast to MUSIC it relies on two identical arrays related to each other by a linear displacement. The advantage is, that the actual array geometry has not to be known. Thus, no calibration of the array manifold is necessary as long as the arrays behave identically. Only the length and the direction of the displacement is required to be known.

The modelling of the received signal is done in a similar way as for MUSIC. The only difference is that there are two sets of output signals, one for each subarray:

$$\begin{aligned} \mathbf{x} &= \mathbf{A}\mathbf{s} + \mathbf{n}_x && \text{first subarray} \\ \tilde{\mathbf{x}} &= \mathbf{A}\Phi\mathbf{s} + \mathbf{n}_{\tilde{x}} && \text{second subarray} \end{aligned} \quad (2.100)$$

The matrix  $\Phi$  is diagonal and holds the complex scaling coefficients

$$\Phi_k = e^{j\omega_0 \Delta \cos(\theta_k)/c_0},$$

where  $\theta$  is the angle of incidence for the  $k$ th element of  $\mathbf{s}$  and  $\Delta$  the length of the displacement between the two arrays. Following the considerations in the last section, the auto- and crosscorrelation matrices of the two arrays are

$$\begin{aligned} \mathbf{R}_{xx} &= \mathbf{A}\mathbf{R}_{ss}\mathbf{A}^H + \sigma^2\mathbf{I}, \\ \mathbf{R}_{x\tilde{x}} &= \mathbf{A}\mathbf{R}_{ss}\Phi^H\mathbf{A}^H + \mathbf{R}_{n\tilde{n}}. \end{aligned} \quad (2.101)$$

In case the two arrays are completely independent, the noise crosscorrelation matrix  $\mathbf{R}_{n\tilde{n}}$  is zero, as the noise sources are uncorrelated. However, it is also possible to consider two identical  $M - 1$ -element subarrays of a uniform  $M$ -element array. E.g. elements  $1 \dots M - 1$  as the first array and element  $2 \dots M$  as the second array. In the latter case, the noise sources are pairwise identical and the noise crosscorrelation matrix is

$$\mathbf{R}_{n\tilde{n}} = \sigma^2\mathbf{Z}, \quad (2.102)$$

where  $\mathbf{Z}$  is a matrix with ones on the first subdiagonal and zeros elsewhere. As for MUSIC the noise variance  $\sigma^2$  is given by the smallest eigenvalue of  $\mathbf{R}_{xx}$ . Thus, the correlation matrices for the noiseless case can be calculated as

$$\begin{aligned} \mathbf{C}_{xx} &= \mathbf{R}_{xx} - \sigma^2\mathbf{I}, \\ \mathbf{C}_{x\tilde{x}} &= \mathbf{R}_{x\tilde{x}} - \sigma^2\mathbf{Z}. \end{aligned} \quad (2.103)$$

Now consider the linear matrix pencil

$$\{\mathbf{C}_{xx}, \mathbf{C}_{x\tilde{x}}\} := \mathbf{C}_{xx} - \gamma\mathbf{C}_{x\tilde{x}} = \mathbf{A}\mathbf{R}_{ss}(\mathbf{I} - \gamma\Phi^H)\mathbf{A}^H. \quad (2.104)$$

In general the rank of this matrix pencil will be  $D$  as  $M - D$  diagonal elements of the diagonal matrix  $\mathbf{R}_{ss}$  are zero, which cancels out  $M - D$  columns and rows of the matrix pencil. The rank is further reduced if the value of  $\gamma$  leads to an additional cancellation of one row and column. This is true for any  $\gamma = \Phi_k$ , hence the angles  $\theta_k$  are obtained by solving the generalised eigenvalue problem

$$\det\{\mathbf{C}_{xx} - \gamma\mathbf{C}_{x\tilde{x}}\} = 0, \quad (2.105)$$

and identifying the  $D$  eigenvalues located on the unit circle in the complex domain. The remaining  $M - D$  eigenvalues are all zero. As the calculations are based on an estimate of the correlation matrix in real application, there will be some deviation with respect to the position of the eigenvalues. A well-suited approach is defining a maximum distance for which eigenvalues are assigned to the unit circle. This threshold has to be found empirically, as it depends on the number of channels, the dimension of the estimated correlation matrix and the signal-to-noise ratio.

The signal amplitude is the second target parameter of interest. With  $\mathbf{e}_k$  being the eigenvector corresponding to the  $k$ th eigenvalue, the following equation holds due to the definition of the generalised eigenvalue problem:

$$\underbrace{\mathbf{A} \mathbf{R}_{ss}}_{\text{diagonal}} \left( \mathbf{I} - \gamma_k \mathbf{\Phi}^H \right) \mathbf{A}^H \mathbf{e}_k = \mathbf{0} \quad (2.106)$$

The centre part of (2.106) is diagonal with the  $k$ th element on the diagonal being zero. Hence, the eigenvector  $\mathbf{e}_k$  is shown to be orthogonal to a subspace spanned by the vectors  $\mathbf{a}_n$ ,  $n \neq k$ . Using this property of  $\mathbf{e}_k$  allows solving

$$\mathbf{e}_k^H \mathbf{C}_{xx} \mathbf{e}_k = \mathbf{e}_k^H \mathbf{A} \mathbf{R}_{ss} \mathbf{A} \mathbf{e}_k = \mathbf{e}_k^H \mathbf{a}_k |s_k|^2 \mathbf{a}_k^H \mathbf{e}_k \quad (2.107)$$

for the signal power reflected by the  $k$ th target:

$$|s_k|^2 = \frac{\mathbf{e}_k^H \mathbf{C}_{xx} \mathbf{e}_k}{|\mathbf{e}_k^H \mathbf{a}_k|^2} \quad (2.108)$$

It shall be noted that for MUSIC the determination of the signal power is possible in a similar way.

### 2.6.5 Two-Dimensional Imaging

Aside from the narrow band assumption, no restrictions with regard to the waveform have been made in the above considerations. Both the data model and the beamsteering matrix rely only on the amplitude and phase relation between the receivers. As long as this information is preserved, any processing of the received signal is allowed. In case of FM-CW radars this is true due to the coherent nature of the receiver, but also the range processing using Fourier analysis maintains the information about amplitude and phase for each range cell. Hence, the usual way for two-dimensional radar imaging is to calculate the range profile with an appropriate method in the first step. In the second step the output of the range processor serves as input for the beamformer to get a two dimensional radar image resolved in both range and angle (cf. Fig. 2.25).

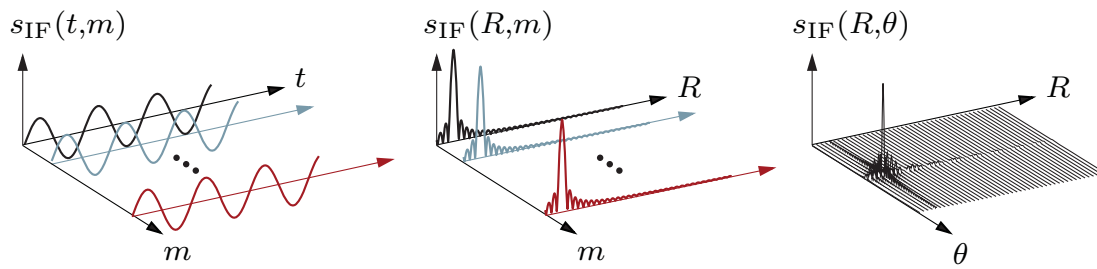


**Fig. 2.25:** Two-dimensional imaging with FM-CW-radars.

### 2.6.6 Broadband True Time Delay Beamformer

The extension of the narrowband approach for wideband waveforms is possible in a straightforward way [39]. According to Fig. 2.26 the received signals have to be divided into spectral subbands with sufficiently narrow bandwidth, e.g. using a Fourier transform (FT). Now, the above mentioned techniques are applied to the subbands. The outputs of the narrowband beamformers are combined and an inverse Fourier transform (IFT) is applied in order to assemble the output of the overall wideband beamformer. It is important to note that for the narrowband beamformers only techniques are allowed that ensure a constant amplitude and linear phase progression between the subbands, otherwise the wideband waveform degrades due to dispersion. Using a conventional beamformer in this wideband framework shows, that this is simply the implementation of a true time delay (TTD) in the frequency domain, as the beamforming weights are adjusted according to the respective centre frequency of each subband. The challenge is that the spectral analysis – that may be performed in the digital domain using a fast Fourier transform (FFT) – must be able to handle the full signal bandwidth.

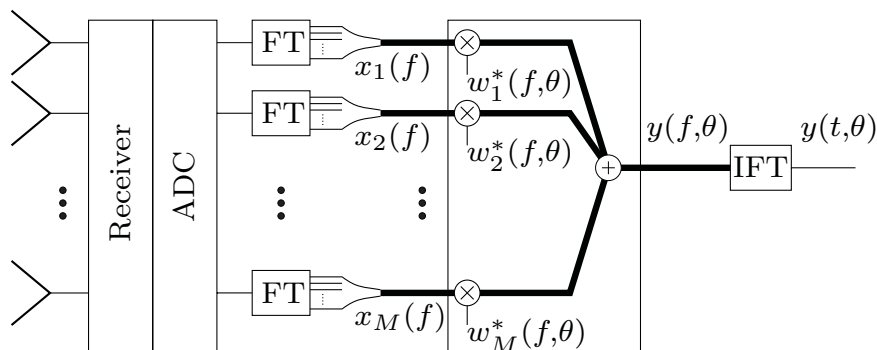


**Fig. 2.26:** Block diagram of a generic broadband beamformer.

In the above considerations it has been shown that for FM-CW radars the IF-time domain samples directly provide the RF-frequency domain representation of the channel response. Hence, there is no need for a spectral decomposition of the down-converted signal, as this is already accomplished by the dechirp operation in the analogue receiver. The wideband processing of an FM-CW sensor array is shown in Fig. 2.27. Assume an array of  $M$  receivers and  $N$  baseband samples per receiver. Each of these samples resemble the real part of the channel frequency response at the respective instantaneous TX frequency. The imaginary part is added using the Hilbert transform. After that,  $N$  narrowband beamformers are used to process  $M$  samples each. The range processing is done afterwards, which is the main difference compared to the narrowband processing in Fig. 2.25.

Simulations have been performed for a sweep bandwidth from 74 GHz to 83 GHz and an FM-CW pulse duration of 1.2 ms. A target was located at an off-boresight angle of  $70^\circ$ . The simulation results are shown in Fig. 2.28.

In both dimensions the resolution is improved when using the described true time delay processing. On the other hand the grating lobe occurring on the left side of the angular spectrum is attenuated by around 6 dB and spread over a wider angular range. The behaviour can be explained when looking at the beamformer output prior to range processing (cf. Fig. 2.29). At 0.66 ms a grating lobe starts to appear. This time exactly relates to an instantaneous transmit frequency of 79.3 GHz. For the given angle of incidence and the spacing of the antenna elements (1.95 mm) this is exactly the frequency where ambiguities are expected from theory due to undersampling of the spatial signal. While the frequency is increased during the FM-CW pulse, the grating lobe is approaching the main lobe. After the range processing this migration of the grating lobe leads to broader distribution and lower overall gain within the grating lobe.

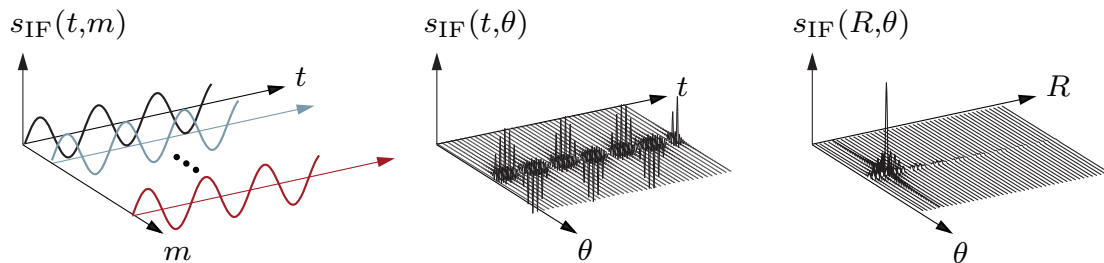


**Fig. 2.27:** True time delay imaging with FM-CW radars.

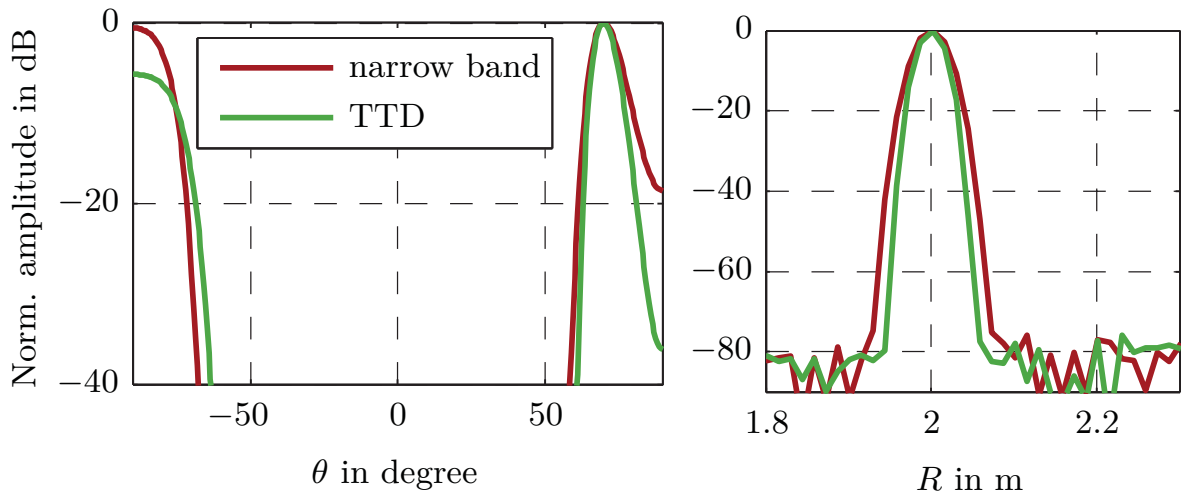


**Fig. 2.28:** Simulated angular (left) and range response (right) of a narrowband beamformer and the described true time delay processing, all values are normalised

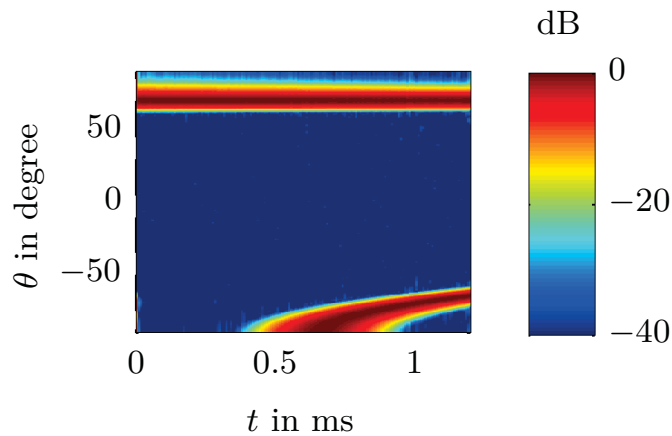


**Fig. 2.29:** Time domain response of the true time delay beamformer before range processing.



### 3 Broadband FM-CW Sensor at 78 GHz

The variety of possible applications for mm-wave sensors implies the development of a modular sensor system. The key component is a broadband dual channel radar sensor that will be described in the following sections.

#### 3.1 Overview and Operating Modes

The building blocks of the FM-CW sensor are depicted in Fig. 3.1. Compared to generic descriptions as in Chapter 2 a more detailed view on the signal generation is provided and some extensions are added for advanced operating modes.

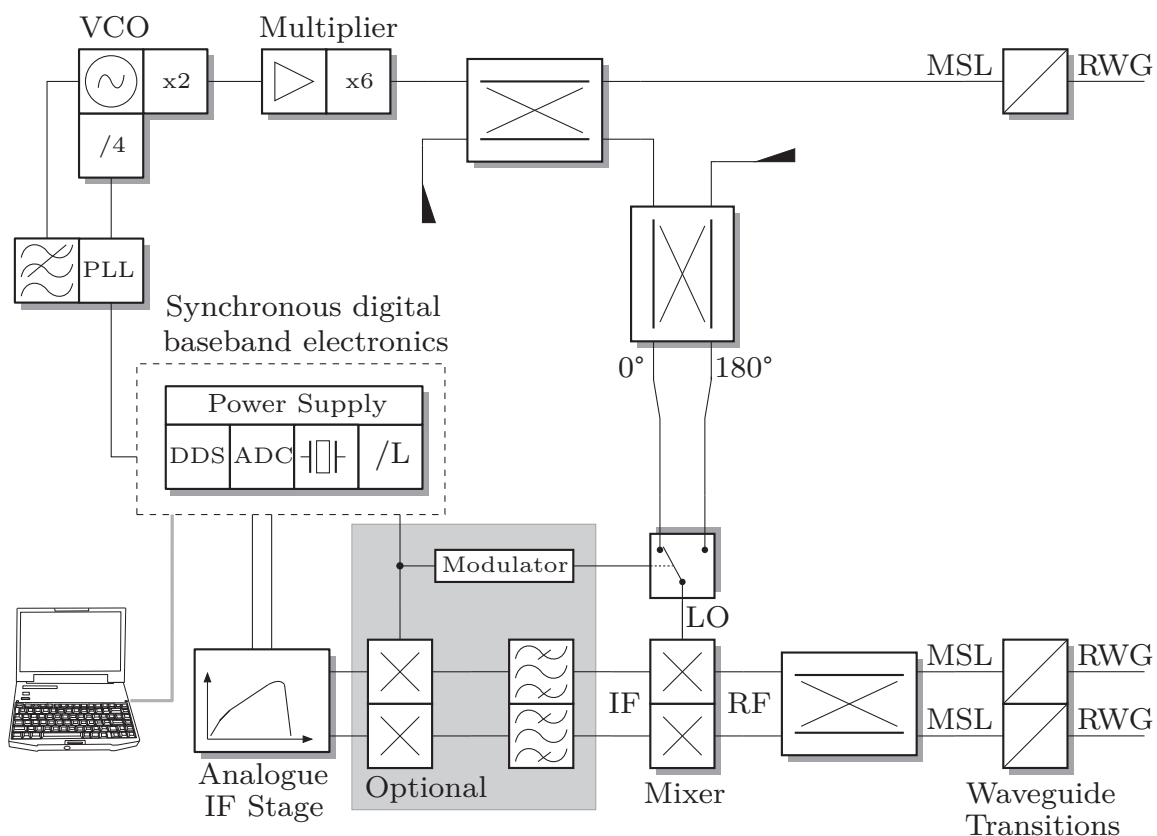


**Fig. 3.1:** Block diagram of the dual channel FM-CW radar sensor.

The synthesiser uses a digital phase-locked loop (PLL) device [40] to lock a VCO [41] operating around 6.5 GHz to the output signal of a DDS (Direct Digital Synthesiser). The mm-wave signal is obtained by a frequency doubler integrated with the VCO and an additional active frequency multiplier by 6 [42]. A comprehensive analysis of the noise and spurious performance of this kind of synthesiser is given in Section 3.3.

A hybrid coupler feeds the generated signal to the transmit path of the sensor and as LO signal to the mixer. As an option, the LO signal can be modulated by binary phase shift keying (BPSK). This offers additional modes such as a heterodyne operation or the detection of active, modulating radar tags.

The input signals at the two receive channels are combined with a 90°-hybrid coupler. This enables single channel I/Q-reception while maintaining dual channel operation. The dual channel mixer [43] is followed by an optional second mixing stage, that is only used in case of heterodyne reception (cf. Section 3.7). An analogue IF stage contains appropriate amplifiers and filters to provide range compensation and to prevent aliasing after the analogue-to-digital conversion (ADC).

The control and synchronisation of the signal generation and the data acquisition is provided by the digital baseband electronics described in [8]. The commanding of these electronics and the processing of the raw data is done using a standard PC or laptop.

To be able to cover as many applications as possible two additional variants of the frontend were designed and fabricated (cf. Fig. 3.2). The monostatic frontend can be used in level gauging or mechanically scanned radars (Section 5.1), whereas the dual channel variant is most suited for digital beamforming radars in combination with a switched antenna array (Chapter 4).

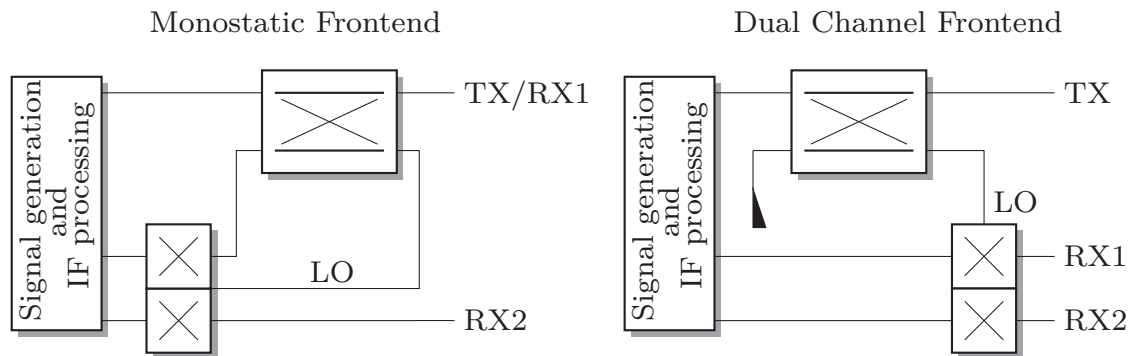


**Fig. 3.2:** Block diagrams of the monostatic (left) and dual channel (right) front-end variants.

### 3.2 Processing Technology and Interconnects

The radar sensor described here is intended for research and demonstration purposes. Thus, some requirements have been defined due to performance, application and cost related reasons:

- usage of in-house thin film and PCB technology as far as possible,
- avoidance of mechanical complexity as far as possible,
- accessibility of the circuits for testing,
- MMIC cavities for low inductance interconnects,
- low sensitivity with respect to fabrication tolerances,
- reliable and low complexity signal interconnects.

An overview of the fabrication technology is given in Fig. 3.3.

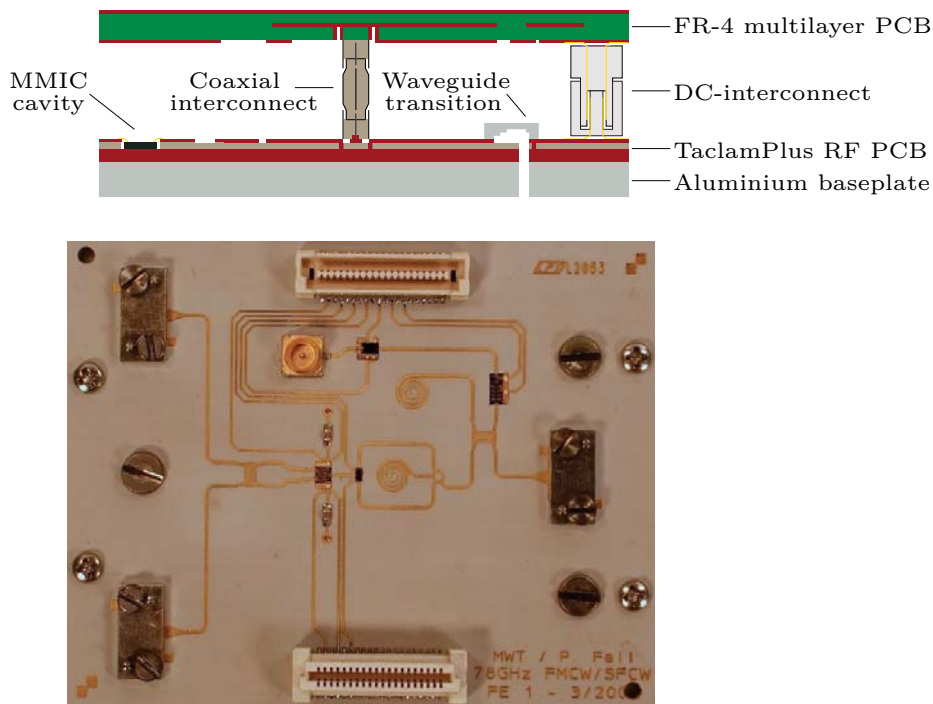


**Fig. 3.3:** Overview of the fabrication technology used for the mm-wave radar sensor (top); photograph of the RF PCB used for the fully featured frontend variant (bottom).

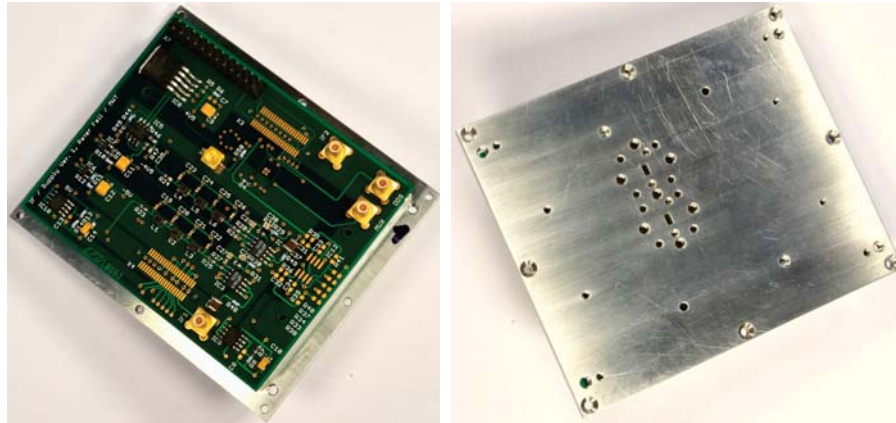


**Fig. 3.4:** Photographs of the monostatic FM-CW frontend.

At mm-wave frequencies it is mandatory to place the MMICs into cavities to enable short and low inductance bond wire interconnects. In modern PCB production facilities these cavities are fabricated by laser ablating [44] or low tolerance (approx.  $\pm 35 \mu\text{m}$ ) depth controlled milling. Both technologies allow cavities on top of multilayer PCBs, but are not affordable for research institutions. Therefore, it was decided to use a so-called metal backed substrate (Taconic TaclamPlus [44]) for the mm-wave circuit. With this kind of substrates the fabrication of cavities is possible with standard precision, but of course the circuit design is limited to a single layer.

The connections to the lower frequency and DC electronics are provided either by coaxial or multipin board-to-board interconnects. A multilayer FR-4 PCB is used for all signals below 2 GHz as indicated in Fig. 3.3. Figure 3.4 shows the final implementation of the frontend according to the principles shown in Fig. 3.3. The design of its key components is described in the following sections.

#### 3.2.1 Microstrip Line-to-Waveguide Transition

Right angle MSL-to-waveguide transitions are very useful for the design of mm-wave modules, as they help realising a compact circuit layout. In literature many different approaches are described. Most of them are based on a radiating patch protruding into the waveguide a quarter wavelength apart from a backshort [45, 46]. All of these transitions require a double sided structuring of the microstrip substrate, but for metal backed substrates the circuit design is bounded to a single layer. Therefore the choice of suitable waveguide transitions is limited. Especially as a right-angle transition was required, a new structure had to be found that can be produced easily by single-layer etching and milling processes.

Details on this waveguide transition can be found in [47]. A short description is given in the next paragraph.

The transition (Fig. 3.5) is based on a combination of well-known techniques. First, the microstrip line is transformed into a via-bounded substrate-integrated waveguide (SI-WG). Several structures are reported for this purpose [48], a simple tapered transition is used in this case. The substrate integrated waveguide is then transformed into a waveguide partially filled with air. To obtain a broadband matching this is done with two quarter wave sections. The third part of the overall transition is a right angle bend in the E-plane. The matching of this bend has been improved using a single step as in [49]. Due to the high frequency, only

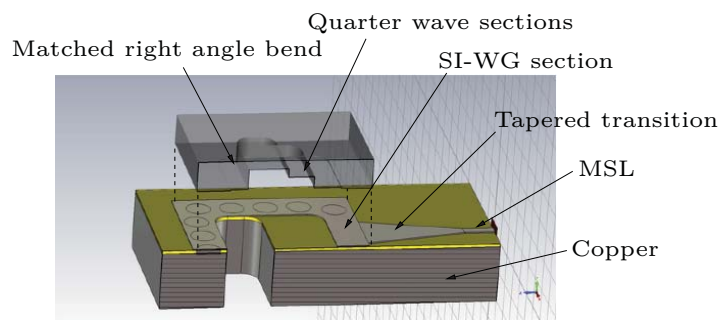


**Fig. 3.5:** Schematic of the substrate-integrated waveguide based transition. The lid is lifted for clarity.

scalar measurements were performed in a back-to-back configuration within this work. Hence, an exact deembedding of a single transition was not possible. However, the measured data could be compensated for the line losses (ca. 1 dB/cm) estimated by two identical setups with different line lengths. The back-to-back test structure and the measured results are depicted in Fig. 3.6. The transition shows a very flat and broadband behaviour. Insertion loss is better than 0.5 dB in the simulation and less than 2 dB in the measurement. Return loss is greater than 10 dB from 61 GHz to 90 GHz in both simulation and measurement. The comparison of measured and simulated results shows a good agreement.

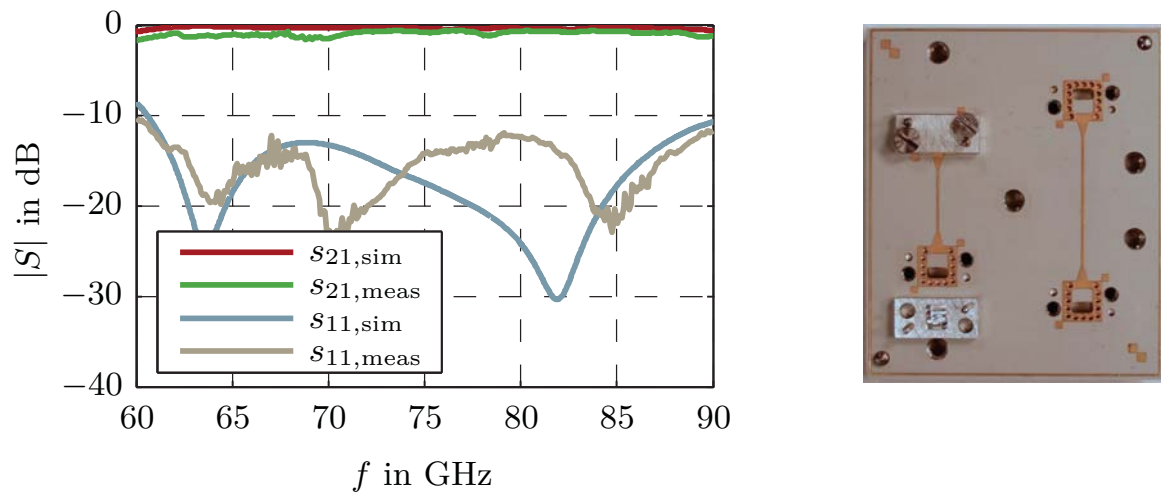


**Fig. 3.6:** Simulated and measured S-parameters of the substrate-integrated waveguide based transition (left); back-to-back test setup (right).

### 3.2.2 Planar mm-Wave Components

In addition to the microstrip line-to-waveguide transition the most critical planar mm-wave component is the coupler. According to the block diagrams in Fig. 3.1 and Fig. 3.2 couplers have to perform different tasks in FM-CW radars as shown here. They act as power splitters in order to obtain the LO signal, and furthermore provide two signals with a well-defined phase shift. The latter feature is needed for I/Q reception ( $90^\circ$  phase shift) as well as for BPSK modulation ( $180^\circ$  phase shift).

The couplers in this work are designed following common design rules [50], thus, they shall be described only very shortly. For all planar structures the simulation and optimisation was done using Agilent ADS/Momentum [51]. As the desired bandwidth is in the order of 10% and having other applications in mind requiring an even larger bandwidth [52], it was decided to consider a broadband two stage branchline coupler as a suitable candidate in case of the  $90^\circ$ -coupler. The simulated scattering parameters are depicted in Fig. 3.7. The

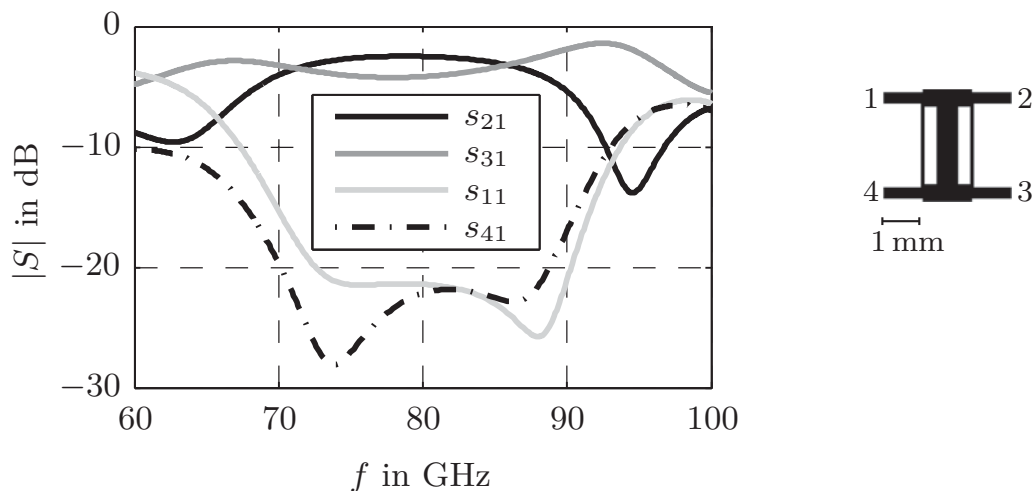


**Fig. 3.7:** Simulated scattering parameters of the two stage  $90^\circ$ -branchline coupler (left); layout and definition of the ports (right).

bandwidth ranges from 72 GHz to 90 GHz with respect to a return loss and an isolation being better than 20 dB. The direct path  $s_{21}$  and the coupling path  $s_{31}$  are slightly asymmetric, which is a compromise between a high return loss, a good isolation, and restrictions given by the fabrication technology. However, the coupler is well suited for radar and communication applications allocated in the frequency range from 71 GHz to 86 GHz.

For monostatic sensors the isolation of the TX/RX duplexer is very critical as the direct leakage from the transmitter to the receiver can determine the

sensor's noise floor as it is explained in Section 3.6. For this reason and to have a 180°-coupler available, a rat race coupler was designed (cf. Fig. 3.8). With respect to a 20 dB return loss and isolation the coupler provides a wide

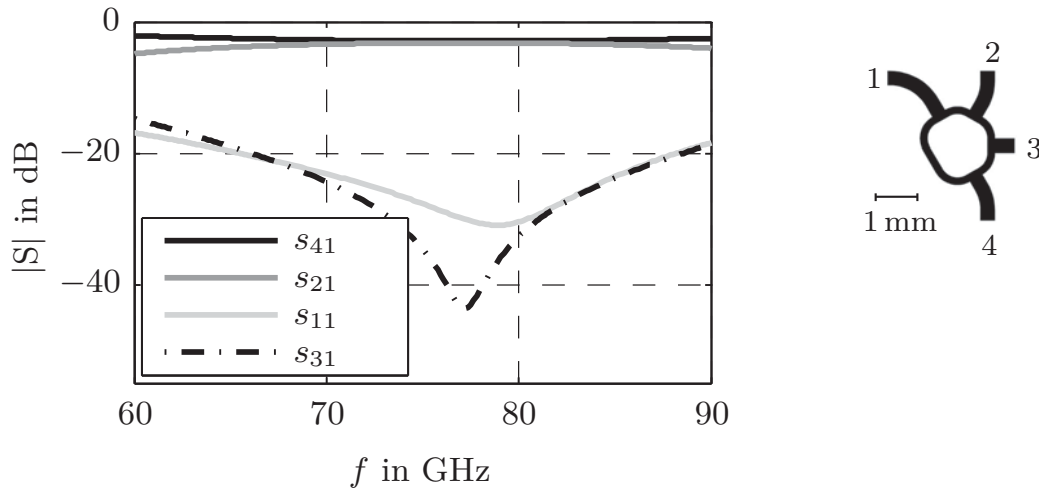


**Fig. 3.8:** Simulated scattering parameters of the 180°-rat race coupler (left); layout and definition of the ports (right).

bandwidth from 66 GHz to 88 GHz, again covering the important frequencies used for radar and communication applications.

### 3.3 FM-CW Synthesiser

The waveform synthesis is done using a DDS (Direct Digital Synthesiser) at frequencies below 25 MHz. DDS devices provide precise frequency tuning in the  $\mu\text{Hz}$  range and extremely linear frequency modulated waveforms. However, the signal has to be up-converted to the actual mm-wave frequencies. Using cascaded frequency multipliers would be an intuitive approach, but currently no devices are available, providing a frequency multiplication by a factor of approx. 3000 at reasonable cost and phase noise or jitter performance. Solutions reported in literature typically use combinations of multipliers and control loops. These can be either PLLs (Phase-Locked Loops) [8] or frequency control setups. [53]. Additional frequency shifting stages using an up-conversion with a fixed frequency local oscillator can help improving the phase noise, but introduce higher system complexity [54].

In this work a direct PLL-based approach is used as depicted in Fig. 3.1. The term “direct” means, that there is no frequency shift or up-conversion included within the synthesiser. Basically, the PLL can be considered as an adjustable frequency multiplier. That means that the frequency but also the phase noise

applied to the PLL input is multiplied. As mentioned before, the overall multiplication factor including the PLL and the external multipliers has to be rather high in order to meet the desired output frequency. Hence, special care has to be taken when generating the baseband waveform. DDS devices are precise and flexible signal sources but contain inherent deterministic perturbations that also depend on the output frequency. So it is necessary to investigate these effects in order to get the best possible synthesiser performance.

### 3.3.1 Modelling and Performance of Direct Digital Synthesisers

A direct digital synthesiser is a digital device converting a fixed frequency clock, typically provided by a quartz oscillator (XCO), into a variable frequency, discrete time sinusoidal output signal [55]. The functional principle is shown in Fig. 3.9. The core of the DDS is an  $n_{\text{Acc}}$  bit wide accumulator, which is incremented by the so-called frequency tuning word (FTW) for each clock cycle. The output value  $M_{\text{Acc}}$  of the accumulator represents the instantaneous phase

$$\phi_{\text{inst}} = 2\pi \frac{M_{\text{Acc}}}{2^{n_{\text{Acc}}}} \quad (3.1)$$

of the desired output signal. It can be easily derived that for a given clock frequency  $f_{\text{CLK}}$  the frequency tuning word has to be chosen as

$$\text{FTW} = \text{round} \left[ 2^{n_{\text{Acc}}} \frac{f_{\text{out}}}{f_{\text{CLK}}} \right]. \quad (3.2)$$

To provide a fine frequency tuning the word length of the accumulator is typically quite high (up to 48 bit). As a consequence a tremendous number of phase states has to be translated to respective amplitudes. To reduce the size of the lookup table to a reasonable value the word length is truncated to  $n_{\text{LU}}$  bit prior to the lookup. Of course, this truncation introduces a deterministic phase error as a

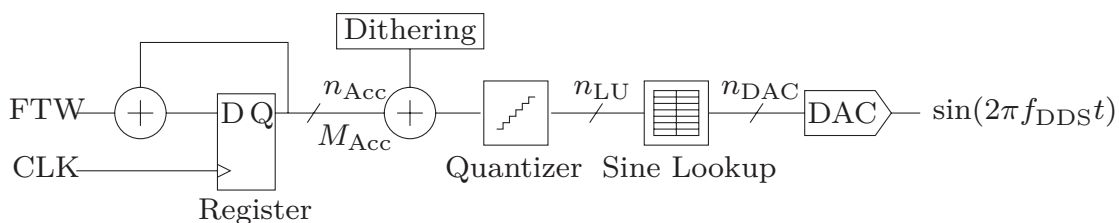


**Fig. 3.9:** Functional block diagram of a DDS according to [55].

function of time and output frequency [56, 57]. To reduce the power density of the resulting spurious lines, small random numbers are added prior to phase quantisation. Even though these numbers are below the smallest quantisation level of the following stage, they can produce carry-forwards affecting the higher significant digits. Using this technique the power of the spurious lines is spread over a certain frequency range. Also the values stored in the lookup table and fed to the DAC are subject to quantisation. At the output this contributes to both phase noise and amplitude noise. In addition to the intrinsic error sources the phase noise or jitter of the clock signal affects the signal quality at the DDS output.

As mentioned before, direct synthesiser setups with high multiplication factors are very sensitive to signal perturbation at the input. Therefore, it is necessary to investigate the DDS by means of simulations in order to quantify the perturbations and to identify optimum operating conditions. Figure 3.10 shows the phase noise spectrum of a DDS obtained by simulation and measurement. The location of the dominant spurious lines can be predicted by the model quite well. With respect to the power density there are differences. This is due to the fact that some details of the internal implementation of the DDS device are not completely known, especially concerning the dithering technique. The noise floor seen in the measurement is significantly higher than for the simulation. As the noise of the input clock is considered in the simulation there must be an additional noise contribution.

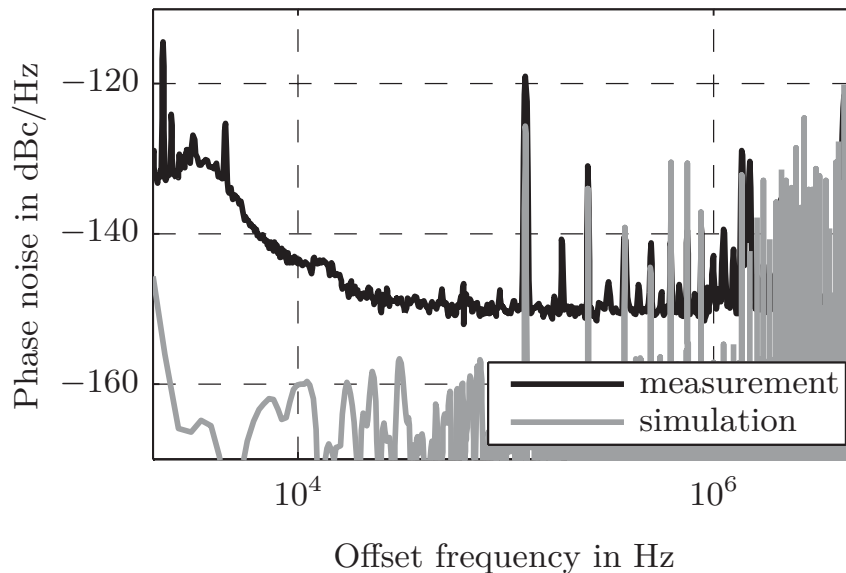


**Fig. 3.10:** Simulation and measurement of the DDS phase noise spectrum at an output frequency of 23.943 MHz.

It turned out that the DDS is quite sensitive to perturbations introduced by its power supply. To investigate the impact of different power supply variants, an output frequency of  $f = 25 \text{ MHz} = \frac{f_{\text{CLK}}}{4}$  was used, for which a minimum spurious signal content can be expected, as in this case there is no phase truncation within the DDS. The measurement results in Fig. 3.11 prove the influence of the power supply. The noise of the input clock is depicted for comparison. The

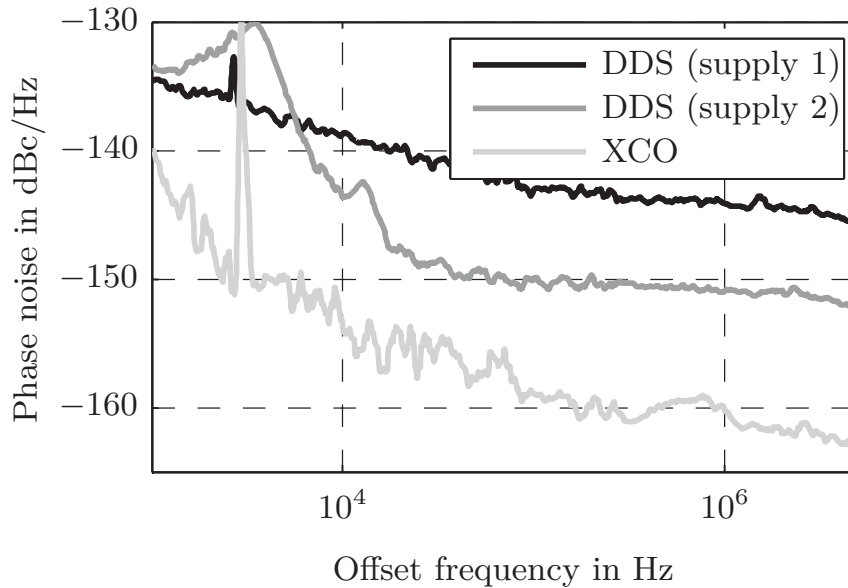


**Fig. 3.11:** DDS phase noise floor measured at  $f_{\text{DDS}} = f_{\text{CLK}}/4$  with different power supply variants in comparison with XCO phase noise.

spurious line at 4 kHz in the clock spectrum indicates that there is a harmonic perturbation in the main power supply. On the one hand, the presence of noise in the input signal directly affects the output spectrum of the DDS. On the other hand, the response of the voltage regulators supplying the DDS device converts the harmonic perturbation into wideband noise, the spectrum of which depends on the dimensioning of the regulator. For the FM-CW application investigated here, supply variant 2 shown in Fig. 3.11 is better suited, as the phase noise is 7 dB to 8 dB less at higher offset frequencies.

### 3.3.2 Phase-Locked Loop Design

Phase-locked loops (PLL) as shown in Fig. 3.12 are typically used to stabilise a tunable VCO by phase-locking it to a stable and low phase noise fixed-frequency signal source. Basically, a PLL is a feedback control loop that tunes the VCO in

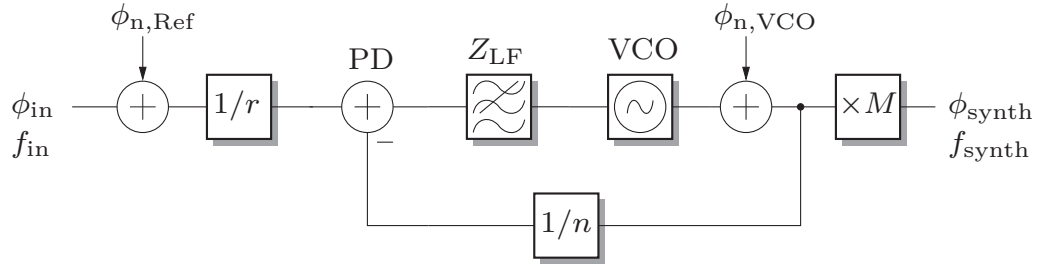


**Fig. 3.12:** Block diagram of the phase-locked loop (PLL) synthesiser including the dominant sources of phase noise and the frequency multiplier used to generate the mm-wave frequency output.

such a way that the phase difference detected with the phase detector is zero or at least constant. In the locked state this leads to the following relation between the input and output frequency:

$$f_{\text{synth}} = M \frac{n}{r} f_{\text{in}} \quad (3.3)$$

Hence, frequency tuning of the VCO can still be accomplished by changing the divider ratio  $\frac{n}{r}$  or the input frequency  $f_{\text{in}}$ . The latter possibility is used in the generation of the FM-CW waveform as the input signal is provided by a DDS.

As any linear system a PLL can be described in terms of its transfer function in the frequency domain [58]

$$\Phi_{\text{synth}}(s) = M \frac{1}{r} \frac{K_{\text{PD}} Z_{\text{LF}}(s) \frac{K_{\text{VCO}}}{s}}{1 - K_{\text{phi}} Z_{\text{LF}}(s) \frac{K_{\text{VCO}}}{s} \frac{1}{n}}, \quad (3.4)$$

with  $K_{\text{PD}}$  being the phase detector constant and  $K_{\text{VCO}}$  the tuning slope of the VCO. Modern high frequency PLL devices [40] mostly are pure digital devices with adjustable divider ratios and a charge pump as phase detector output. To convert the current provided at the phase detector output, the loop filter is implemented as a frequency dependent impedance  $Z_{\text{LF}}(s)$ . As frequency multiplying is equivalent to multiplying the phase, the phase at the output of the PLL is simply weighted with a constant factor  $M$ .

The proper choice of the loop filter bandwidth is crucial, as it determines the agility of the synthesiser and at the same time the suppression of the wideband phase noise. These two properties are contradictory, so a trade-off has to be found.

The instantaneous phase of the input chirp signal consists of a linear, a quadratic, and a zero mean random band-limited part that relate to the start

frequency, the frequency slope, and the phase noise, respectively. In general infinite time linear or quadratic signals have a zero bandwidth. However, in FM-CW systems time-limited pulses are used resulting in a signal bandwidth being the reciprocal of the pulse duration. The system described here aims to provide pulse durations down to 100  $\mu$ s. To restrict settling effects in the time domain to a small percentage of the pulse duration, a PLL bandwidth of 400 kHz was chosen.

Figure 3.13 shows the output power and phase noise spectra of the FM-CW synthesiser at different output frequencies. PLL-locking is achieved within the

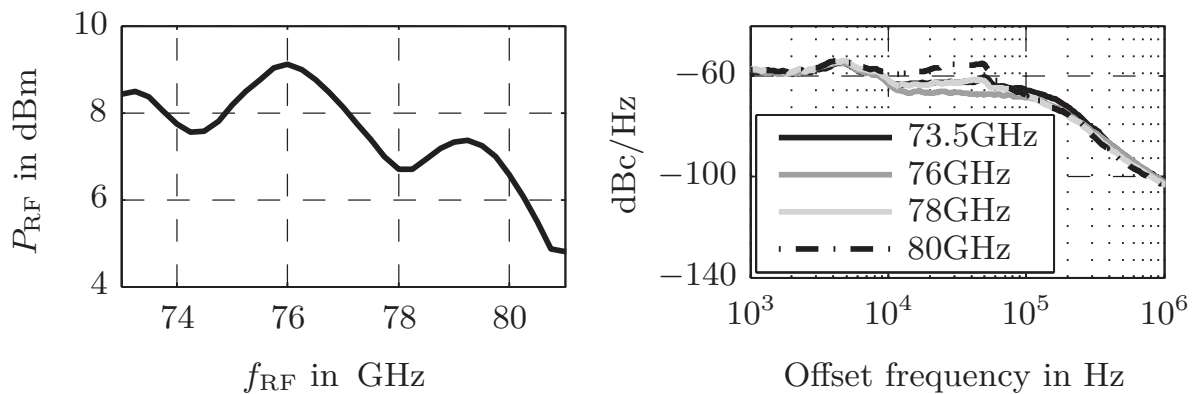


**Fig. 3.13:** Measured output power of the monostatic frontend as a function of the output frequency (left) and phase noise spectrum (right) of the PLL synthesiser used for the FM-CW radar.

complete tuning range of the VCO, providing a frequency range from 73 GHz to 80.5 GHz with an output power between 5 dBm and 9 dBm, measured at the waveguide output of the frontend.

### 3.4 Analogue DC and Baseband Electronics

Apart from signal generation, data acquisition, and the actual RF frontend, additional DC and low frequency electronics are required. These electronic circuits have to provide the power supply and switch-on logic for the MMICs and the low frequency integrated circuits. The design of these parts mainly follows the datasheets and application notes of the suppliers, so there is no detailed discussion at this point. However, the dimensioning of the circuits should be done in a way to achieve the best possible noise performance, as this is crucial especially for the synthesiser.

As a second task, an appropriate analogue processing of the receiver output signal has to be performed. As this part is rarely treated in literature, the next section will give an overview of the design.

### 3.4.1 Intermediate Frequency Filtering Stage

The signal at the mixer output is typically small, but covers a high dynamic range, as in the worst case the received power is related to  $R^{-4}$ . So there has to be an analogue filtering stage preceding the ADC that has to fulfil the following requirements:

- reduction of signal dynamic,
- anti-aliasing filtering,
- low noise amplification.

This analogue processing stage has to be designed in a way that – under typical operating conditions – the signal level at the input of an ADC is within the limits given by its dynamic range. The block diagram of the implementation described here is shown in Fig. 3.14. The required properties and the design of the building blocks are discussed in the following paragraphs.

The response of radar targets typically decays with distance following  $P_{RX}(R) \sim R^2 \dots R^4$  depending on the target size and shape [59]. In pulse radars this range or time-of-flight dependent decay is equalised using a so-called sensitivity time control (STC). As for FM-CW radars the intermediate frequency is related to the target distance, this STC can be replaced by an appropriate filtering in the IF domain [60]. Consequently, the respective functional block is called SFC-filter (Sensitivity Frequency Control). In case of a frequency modulation with a linear slope, this SFC-filter is a simple high pass filter (SFC-HP). Each order  $n$  of this filter compensates for a  $P_{RX}(R) \sim R^{2n}$  decay. The choice of  $n = 1$  or  $n = 2$  depends on the expected radar targets and was chosen to be  $n = 1$ , as this has been shown to be well suited in automotive environments [59] as well as e.g. in level gauging applications.

The strongest signal in FM-CW systems is induced by the direct path from the transmitter to the receiver (RX-TX leakage). As the leakage path is short, its

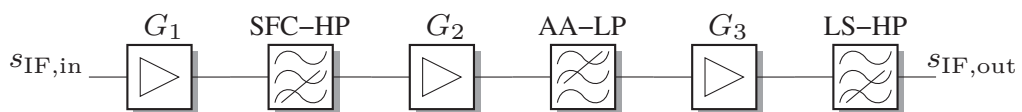


**Fig. 3.14:** Block diagram of the analogue IF processing.

IF response can be suppressed with a high pass filter (leakage suppression high pass, LS-HP). The cut off frequency of this filter is low and therefore defining the settling time. It is important to use filters with a low ringing, as this oscillation may occur in the range spectrum as a ghost target. Suitable filter prototypes are Bessel filters or cascaded critically damped filters [20]. Bessel filters turned out to be a good compromise in terms of transient and frequency response. A second order active Bessel filter is used in this work.

Due to the frequency response the two filters described above, the signal dynamic is minimised. An additional seventh order Chebyshev lowpass filter suppresses frequencies higher than half the sampling rate to ensure an aliasing free representation of the signal in the digital domain (anti-aliasing low pass, AA-LP).

Some considerations have to be made concerning the gain of the amplifier stages. At the first stage the signal still has the full dynamic range. Hence, the gain should be modest to avoid clipping. On the other hand, a higher gain would reduce the impact of the noise contributed by the following stages. Hence, a trade-off has to be found. The gain of all stages is optimised with respect to noise performance and linearity using a SPICE simulator [61].

The parameters of the functional blocks are summarised in Table 3.1.

Block	Gain	Cutoff Frequency
$G_1$	26 dB	-
SFC-HP	0 dB	3.18 MHz
$G_2$	23.5 dB	-
AA-LP	0 dB	2.5 MHz
$G_3$	29.5 dB	-
LS-HP	-6 dB	4 kHz

**Tab. 3.1:** Functional block parameters of the analogue IF processing.

Figure 3.15 shows the simulated and measured transfer function of the analogue IF processing in the frequency domain. Thereby, the simulated and measured behaviour match very well.

Three different regions can be identified. Signals below the cutoff frequency of the leakage suppression-lowpass and higher than the cutoff frequency of the anti aliasing-lowpass are attenuated. The nominal operating frequency range is in between 4 kHz and 2.5 MHz. However, if a target is located at closer distances it still can be detected with a decreased sensitivity.

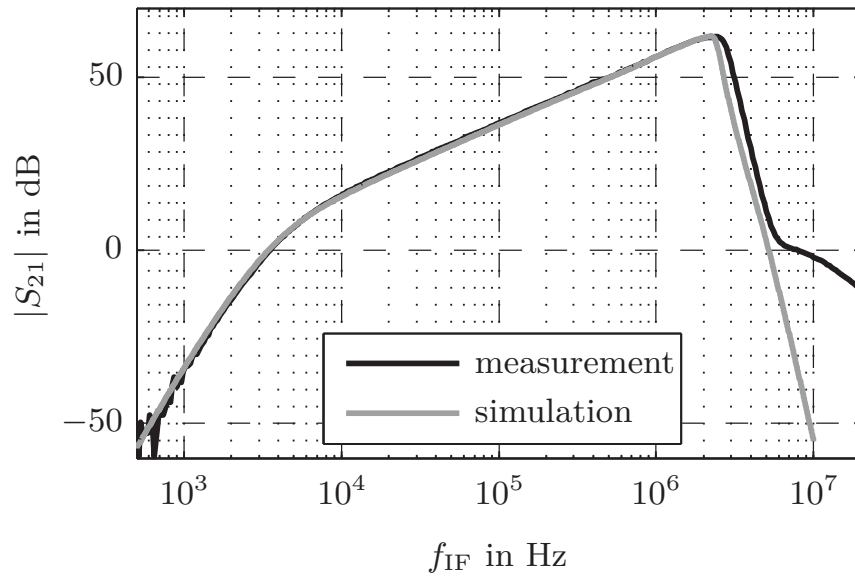


**Fig. 3.15:** Simulated and measured transfer function results of the analogue IF stage.

### 3.5 Comprehensive FM-CW Model and Simulation Results

To investigate the performance of the radar sensor prior to fabrication a precise numerical simulation model is advantageous. Especially with respect to the noise behaviour more insight can be gained compared to an analytical investigation. The challenge when modelling broadband FM-CW radars is dealing with the large signal bandwidth on the one hand and the long pulse duration on the other hand. Choosing the sample rate to meet the Nyquist limit with respect to the transmitted signal bandwidth leads to a time step in the nanosecond scale even for a moderate bandwidth of 1 GHz. The pulse duration in FM-CW radars is typically up to a few milliseconds. This gap of around six orders of magnitude causes a very long simulation time.

In [62] a simulation technique is proposed that models an FM-CW system in terms of the instantaneous frequencies of the transmitted and received signal. As the maximum IF frequency is equal to the frequency difference between those two signals, the simulation sampling rate can be chosen as in the real system. The limitations of this kind of simulation becomes apparent when noise is considered. In [62] all noise sources are considered as additive noise at the output of the receiver. Phase noise effects such as the frequency dependent compression due to the correlated noise included in the LO and received signal are not covered by this model. To overcome this problem it is proposed to shape the additive noise according to the a priori knowledge about these effects.

In this work a model has been set up based on the instantaneous phase of the signals occurring in an FM-CW sensor (cf. Fig. 3.16). The aim was to maintain a low sample rate while covering as many effects as possible. The techniques used to achieve this goal are highlighted hereinafter. The instantaneous phase signal coming from the synthesiser model Fig. 3.12 ( $\Phi_{\text{synth}}$ ) is split into two parts. The first part feeds the LO input of the mixer, the second part experiences the radar signal's propagation delay and is connected to the RF input of the mixer. It is possible to apply an optional BPSK signal to one or both signals in order to model the heterodyne system concept described in Section 3.7. The mixer is modelled as a phase subtractor with a cosine function converting the IF signal's phase to the respective amplitude. Thereby, the signal is weighted according to the received power obtained through the radar equation. The mixer noise and conversion loss  $L_c$  are also modelled according to values taken from the datasheet [43]. Finally, the analogue IF stage is considered using a linear model of the actual circuit.

With respect to the numerical simulation, considerations have to be made concerning the simulation time step. It was shown before, that the instantaneous input phase of the overall model consists of a linear, a quadratic, and a zero mean random part. As the system model is linear up to the cosine block in Fig. 3.16, those three parts can be treated independently. The start frequency cancels out in the mathematical analysis of FM-CW radars and the absolute phase of the transmitted signal is not of interest. Thus, the linear phase term can be omitted, which corresponds to a start frequency of 0 Hz. The quadratic phase term must be retained as it accomplishes the linear frequency modulation.

However, a quadratic signal has a zero bandwidth [20]. Consequently, the inverse length of the FM-CW pulse and the bandwidth of the phase noise de-

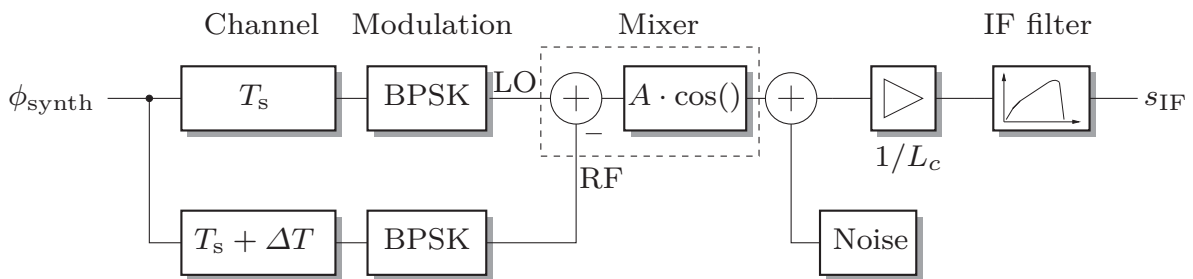


**Fig. 3.16:** Phase domain model of an FM-CW sensor with optional LO modulation for a heterodyne operating mode; modulation of the delayed path enables the simulation of a modulated LO leakage signal.

termine the minimum sampling rate. On the one hand, oscillator phase noise rapidly decays with increasing frequency. On the other hand, a PLL is known to generate a flat noise spectrum up to its loop bandwidth. Hence, the sampling rate must be at least twice the loop bandwidth to properly represent the output phase of the PLL.

Within the mixer model the output signal is determined by applying the cosine function to the phase difference of the transmitted and delayed signal. At this point there is the transition from the phase representation to the amplitude representation of the IF signal. As the frequency of this signal is given by the radar parameters and the target distance, an additional constraint is found for the simulation sampling rate. In the real system the IF sampling rate is 6.5 MHz, so this sampling rate is chosen for the simulation as well.

Additional consideration have to be made when modelling the roundtrip time delay of the radar signal. This delay can amount to any value, that cannot be represented in integer multiples of the simulation time step. As long as the delay is greater than one time step, the delayed sample can be calculated by means of interpolation without increasing the sampling rate [63]. Therefore, both the LO signal and the received signal are delayed by a single simulation time step  $T_s$ .

Figure 3.17 shows the simulated time domain response of the sensor. The parameters of the sensor, the power of the leakage signal and the target are chosen as later on in the measurements (cf. Fig. 3.21). A short settling time of

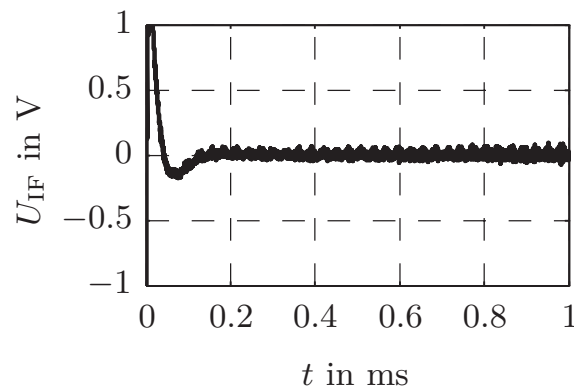


**Fig. 3.17:** Simulated time domain response of the sensor for a target located at a distance of 4 m.

about 100  $\mu$ s can be observed. This is mainly caused by the response of the Bessel high pass filter used for the suppression of low frequency signal components (LS highpass). After this time period the desired harmonic oscillation is seen that is affected by noise. The comparison of simulation and measurement in the

frequency or range domain in Fig. 3.18 shows that the model predicts the sensor behaviour quite well. At closer ranges the simulated noise floor is lower than

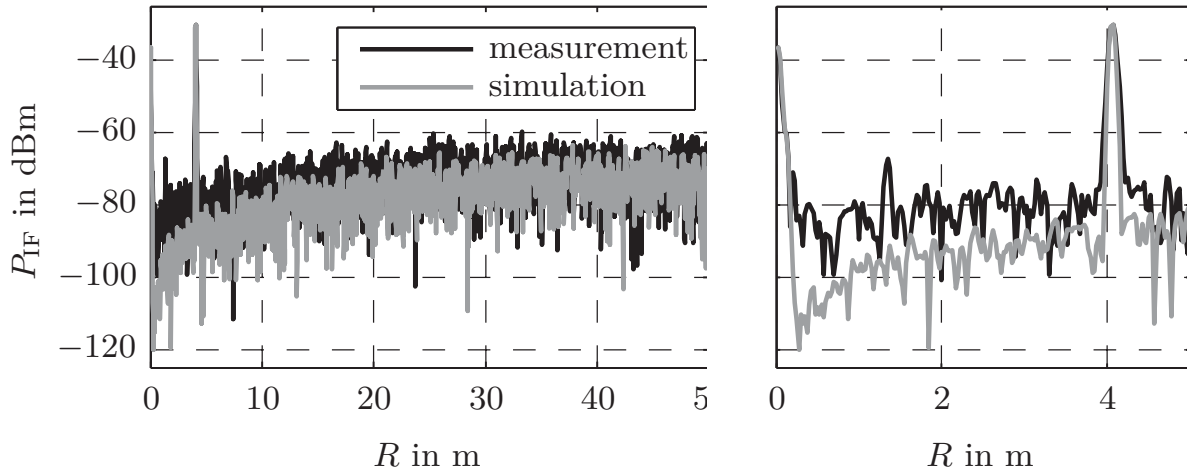


**Fig. 3.18:** Simulated and measured range profiles obtained with the FM-CW sensor for a target located at a distance of 4 m; Internal signal coupling and reflections at waveguide flanges are considered in the simulation.

in the measurement. This deviation is caused by the power supply noise that has not been included in the simulation (cf. Fig. 3.11). For higher intermediate frequencies the noise level matches properly. Even smaller features such as the small drop around 43 m can be recognised in both simulation and measurement.

The advantage of having a reliable model is to be able to investigate the influence of different effects independently. In Fig. 3.19 the simulated noise contribution of the mixer noise and the phase noise related to the major reflections (target and waveguide flange) and the direct signal coupling (RX/TX leakage) is compared. The results imply that the overall system noise is dominated by the phase noise of the leakage signal rather than the noise figure of the mixer.

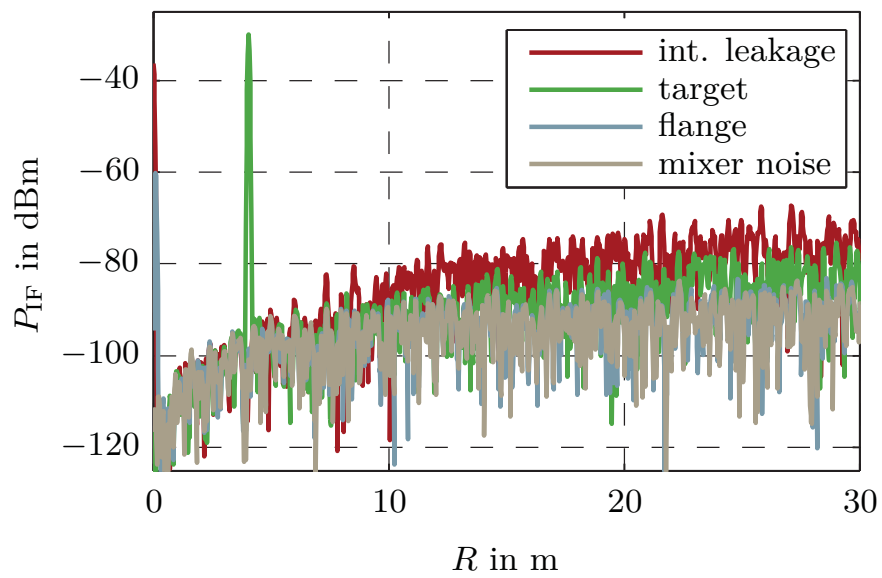


**Fig. 3.19:** Contribution of different noise sources to the overall noise floor.

### 3.6 Performance Evaluation

For the precise evaluation of the sensor performance a well-defined measurement environment is necessary. Using a waveguide setup as shown in Fig. 3.20, reproducible results are obtained to compare sensors and to evaluate the impact of improvements. The free space delay of the radar signal is accomplished by a WR-12 waveguide whereas the losses are simulated using a DRA (Direct Reading Attenuator). The physical length of the waveguide is 3 m. Due to the reduced group velocity of waves propagating within the waveguide, the effective length is 3.86 m at 77 GHz. Additional delays are added by the DRA and the signal lines within the sensor. The overall effective length of the setup is 4.06 m. At its end the waveguide is connected to a short circuit resembling the reflectivity of a target. Both the DRA and the waveguide transmission loss  $L_{WG}$  contribute to the overall inserted loss

$$L_{ins} = L_{DRA} L_{WG} . \quad (3.5)$$

As the sensitivity of the sensor is limited by its noise floor, the latter one has to be determined by suitable measurements. These measurements have to be done in presence of the actual target, as each target raises the noise level due to phase noise included in the radar signal. A simple way to obtain the noise floor spectrum is calculating the variance of a certain number of subsequent measurements. Basically, this approach is a periodogram-based PSD estimator as shown in Section 2.3. In a similar way the signal level is determined by calculating the mean value.

Once the noise floor and the signal power are obtained through system level measurements, the maximum insertable loss can be calculated by multiplying the available margin (SNR) with the inserted loss:

$$L_{max} = L_{ins} \text{SNR} . \quad (3.6)$$

If the transmit power is known, the sensitivity can be expressed in terms of the received power

$$P_{RX,min} = \frac{P_{TX}}{L_{max}} . \quad (3.7)$$



**Fig. 3.20:** Measurement setup for sensitivity tests.

The measurement results using the described setup are shown in Fig. 3.21 together with the key settings of the sensor. The range resolution obtained in this experiment is 6 cm, measured at -3dB with respect to the maximum response. This matches the theoretically expected value given by the sweep bandwidth and the window function. However, the dispersion of the group velocity does not allow a better resolution using the waveguide setup.

An increased noise floor can be observed between 2 m and 6 m, which corresponds to an IF range of 16.7 kHz to 50 kHz. Inspecting the phase noise of the synthesiser in Fig. 3.13 it becomes apparent that this is exactly the frequency range affected by the power supply noise. Hence, this noise is shown to be caused by the phase noise of the signal leaking from the transmitter to the receiver.

The inserted loss  $L_{\text{ins}} = 65$  dB and the SNR margin of 48 dB yield a maximum insertable loss of 113 dB at a target distance of 4.06 m. With an average transmit power of  $P_{\text{TX}} \approx 7$  dBm, the sensitivity can be stated as  $P_{\text{min}} = -106$  dBm.

Using this information the system noise figure is derived in the following. The noise bandwidth of the system is related to the reciprocal of the processing interval:

$$\Delta f_{\text{noise}} = \frac{1}{T} = 208.3 \text{ Hz} \quad (3.8)$$

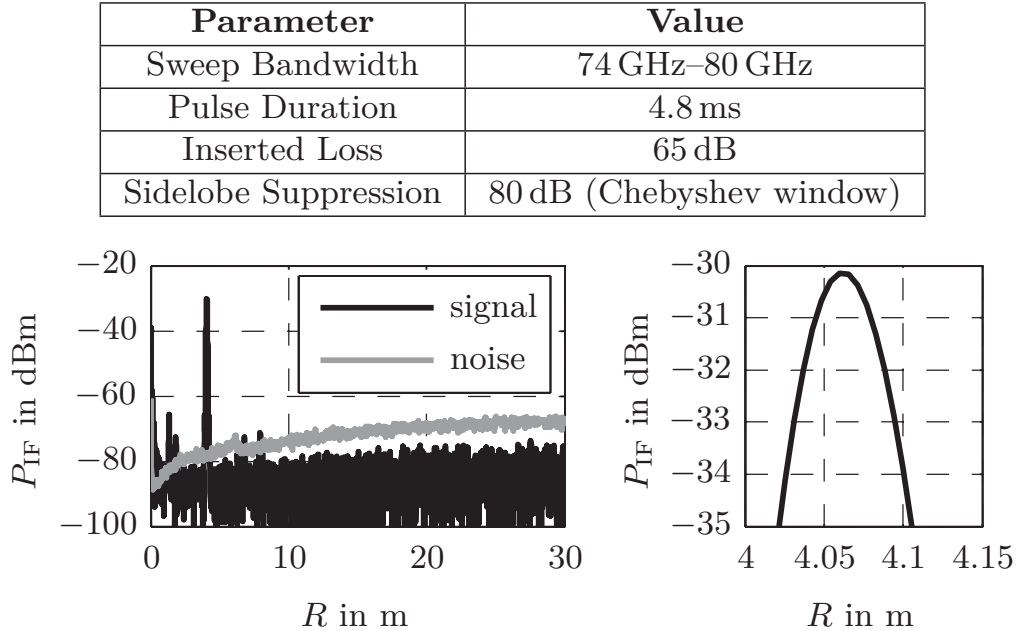


**Fig. 3.21:** Key parameters of sensor configuration and range processing (top); respective signal and noise spectrum (bottom left) and range response (bottom right) obtained using the measurement setup in Fig. 3.20.

In case the processing interval is not a multiple of the signal period, the signal power is spread over several frequency bins within the main lobe and the sidelobes. On the other hand, any window function other than a rectangular window degrades the resolution and at the same time increases the noise bandwidth. According to Section 39 a Chebyshev window with 80 dB sidelobe suppression causes a processing loss up to  $L_{\text{proc}} = 2.4$  dB. Hence, the system noise figure is

$$F_{\text{sys}} = \frac{P_{\text{min}}}{k_B T_0 \Delta f_{\text{noise}} L_{\text{proc}}} = 42 \text{ dB} , \quad (3.9)$$

with  $k_B$  being the Boltzmann constant and  $T_0 = 290$  K the input noise temperature. As the leakage signal phase noise is the major reason for this high value, it can be expected that the noise figure drops significantly for intermediate frequencies higher than the PLL loop bandwidth. Assuming a flat response of the mixer conversion loss, the frequency dependent system noise figure is obtained by weighting the noise floor with the frequency response of the IF stage. The result in Fig. 3.22 proves what has been stated above. For frequencies higher than 400 kHz the noise figure decays down to 22 dB, providing a better sensitivity at farther ranges. However, as already predicted by simulation (see Fig. 3.19) the system sensitivity is still limited by the leaking phase noise. The noise contribution of the mixer is typically 10 dB lower. Hence, a better TX/RX isolation and/or a lower phase noise would be required to improve the sensitivity. If the isolation is limited by the mixer itself, some other techniques are possible; those will be presented in the next sections.

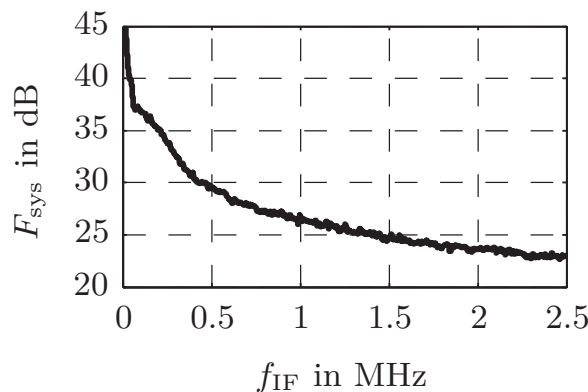


**Fig. 3.22:** Measured system noise figure  $F_{\text{sys}}$  as a function of the intermediate frequency.

### 3.7 Advanced Operating Modes

The LO path in the block diagram of the frontend depicted in Fig. 3.1 on page 53 is extended by a modulator circuit. This modulator comprises a 180°-coupler and an SPDT switch [64]. With this configuration it is possible to apply a BPSK modulation (Binary Phase Shift Keying) to the LO signal. The modulation signal can be either a periodic square wave or an arbitrary binary sequence, e.g. a pseudo noise sequence. The first case leads to a double sideband modulation of the LO signal and allows a heterodyne reception of the transmitted FM-CW waveform. In the second case, received waveforms that are BPSK-coded in the same way can be detected while suppressing uncoded waveforms [65]. The implementation, advantages, and applications of modulated waveforms are discussed in the following sections.

#### 3.7.1 Heterodyne Reception with Periodically Modulated LO

The modulation of the LO signal requires a corresponding modification of the mathematical description in (2.25) and (2.26). Considering the modulation  $s_{\text{mod}}(\tau)$ , the IF signal at the output of the mixer changes to

$$\begin{aligned} s_{\text{IF}}(\tau) &\propto s_{\text{mod}}(\tau) s_{\text{TX}}(\tau) s_{\text{RX}}(\tau) \\ &\propto A_t(\tau) s_{\text{mod}}(\tau) \cos[2\pi S\Delta T \tau + \omega_0 \Delta T - \pi S\Delta T^2 + \phi_t(\tau)], \end{aligned} \quad (3.10)$$

where  $A_t(\tau)$  and  $\phi_t(\tau)$  summarise the total amplitude and phase variations caused by dispersion, phase noise, and modulation nonlinearity. From (3.10) it can be seen that the IF signal carries the same modulation as the LO signal. Feeding the modulator in Fig. 3.1 with a periodic signal leads to  $s_{\text{mod}}(\tau)$  being a square wave without any DC offset. Considering only the fundamental frequency of the modulation signal, this resembles a double sideband modulation with the carrier suppressed. Choosing the modulation frequency at least twice the maximum baseband frequency  $f_{\text{BB,max}}$ , the resulting spectrum will look like that one in Fig. 3.23. There are several possibilities for the further processing. Of course it can be done with an analogue mixer as stated in Fig. 3.1 or using full rate sampling with

$$f_{\text{sample}} = 2(f_{\text{mod}} + f_{\text{BB,max}}).$$

The latter solution requires a down-conversion in the digital domain and a very high sampling rate. However, as the IF signal is a bandpass signal, even under-sampling with

$$f_{\text{sample}} = \frac{f_{\text{mod}}}{N} > 2 f_{\text{BB,max}}$$

would be possible.

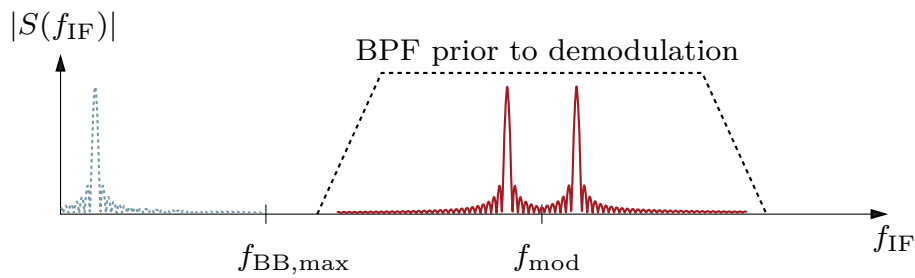


**Fig. 3.23:** Spectrum of the IF signal in case of an unmodulated (dashed blue) or periodically modulated LO (solid red); bandpass filter (BPF, dashed black), that is be applied prior to demodulation.

### 3.7.2 Leakage Phase Noise Suppression

At this point it is not obvious, why a heterodyne reception is advantageous compared to a homodyne reception. As one can see from (2.26) the phase noise of the signal source contributes to the overall noise floor for each target. This is also true for the TX-RX leakage signal mentioned in Section 3.4. The difference is that the main leakage contribution is caused by a finite isolation between the LO and the input port of the mixer (Fig. 3.24). That means, that a “self-mixing”

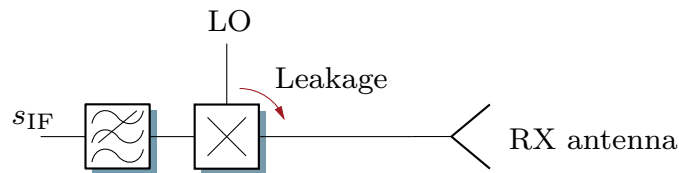


**Fig. 3.24:** LO-RX leakage path in FM-CW radars.

of the LO signal occurs, which leads to an output signal close to DC, and the desired signals around  $f_{\text{mod}}$  remain undisturbed. A similar approach for leakage phase noise suppression is proposed [66], where the modulator is shifted to the RX path and realised as a simple switch.

The measurement results in Fig. 3.25 show that the noise behaviour can be reduced significantly by operating the sensor in the heterodyne mode. Especially at closer ranges an improvement of up to 15 dB is achieved.

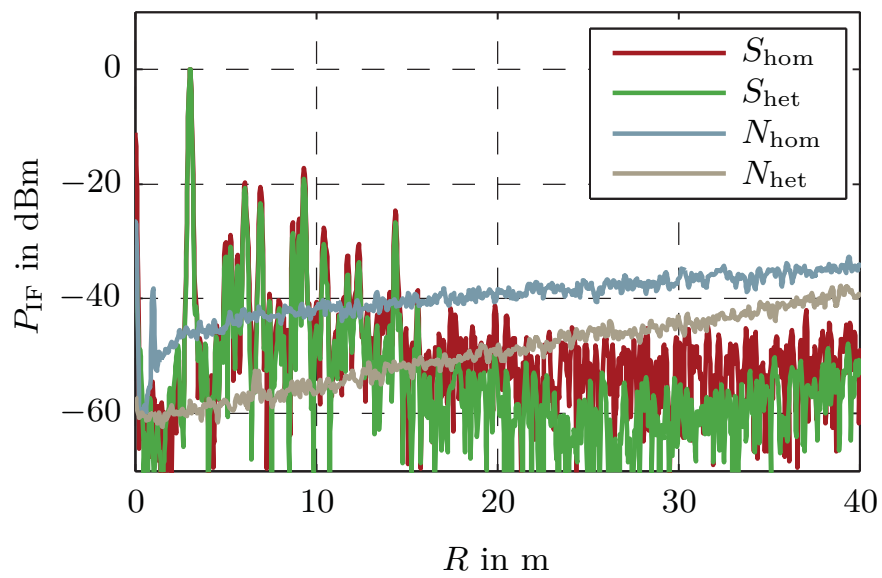


**Fig. 3.25:** Measured signal and noise levels for homodyne (index: hom) and heterodyne (index: het) reception.

### 3.7.3 Phase Noise Cancellation Using a Dual Channel Mixer

As the main noise contribution is due to the internal coupling of the mixer, the use of a monolithic dual channel mixer [43] provides another possibility to cancel the leakage phase noise with a setup as depicted in Fig. 3.26 [67]. Thereby, one

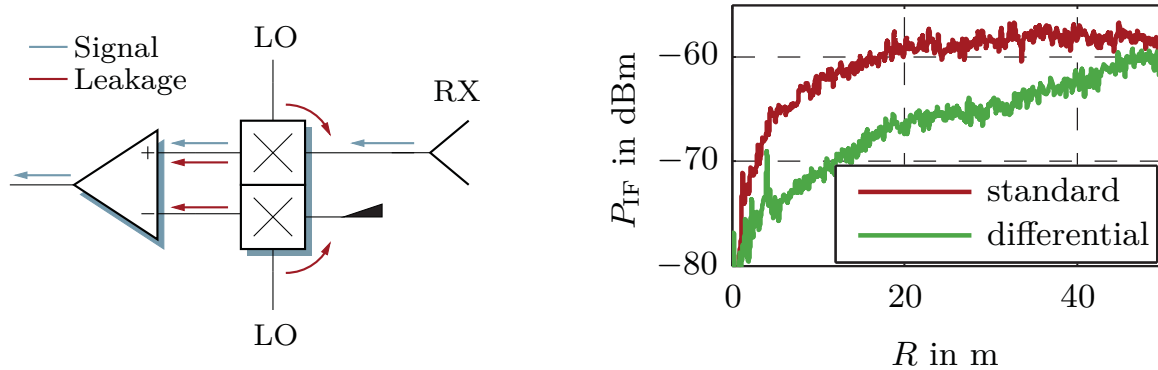


**Fig. 3.26:** Phase noise cancellation using a symmetric dual channel mixer together with a differential analogue IF stage (left); IF noise level for standard and differential operation (right).

mixer channel serves as a reference and delivers only the undesired noise signal at its output. An analogue subtractor removes this noise from the signal acquired with the other channel. The improvement achieved with the differential setup is at the same scale as for the heterodyne receiver.



## 4 Imaging Sensor with Switched Transmit Antenna Array

Imaging radars employing digital beamforming (DBF) typically require a uniform linear antenna array (ULA). However, using a large number of parallel receivers increases system complexity and costs. Switched antenna arrays can provide a similar performance at a lower expense and are proven to be good candidates for high resolution DBF applications [8]. Thereby, switching the transmitting antennas is advantageous compared to a switched receiving array. Amplification stages can easily compensate for losses occurring in the distribution network while the receiver noise figure is not affected. When using multiple receiving antennas, an equivalent aperture can be formed by evaluating each pair of transmit and receive antennas. Figure 4.1 demonstrates this approach for two receive antennas. Including the positions of the respective transmit *and*

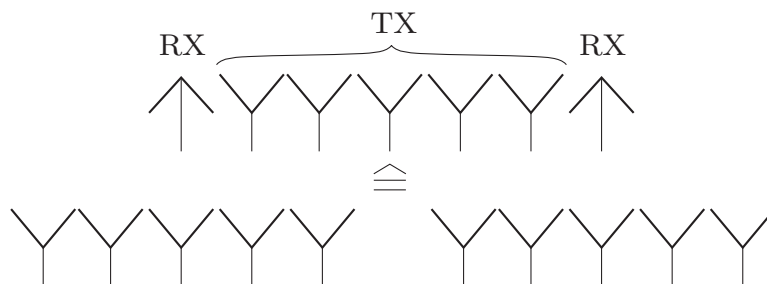


**Fig. 4.1:** Equivalent aperture of a configuration consisting of 5 TX and 2 RX antennas.

the two receive antennas into the signal model in (2.73) leads to a description that is equivalent to having two subarrays, each of which shifted to the position of one of the actual receive antennas. Hence, the equivalent size of the aperture is more than twice the physical aperture size, which yields a significant enhancement of the angular resolution.

This chapter describes the design of an active switched antenna array with 32 integrated planar patch antennas illuminating a cylindrical lens [68]. This array can be operated over a frequency range from 73 GHz to 81 GHz. Together with the broadband FM-CW frontend (cf. Chapter 3) a DBF radar was implemented.

## 4.1 Switching Network and Patch Array

A block diagram of the active switched array is shown in Fig. 4.2. It comprises a five stage SP32T switching network with 31 SPDT switches [64]. After the

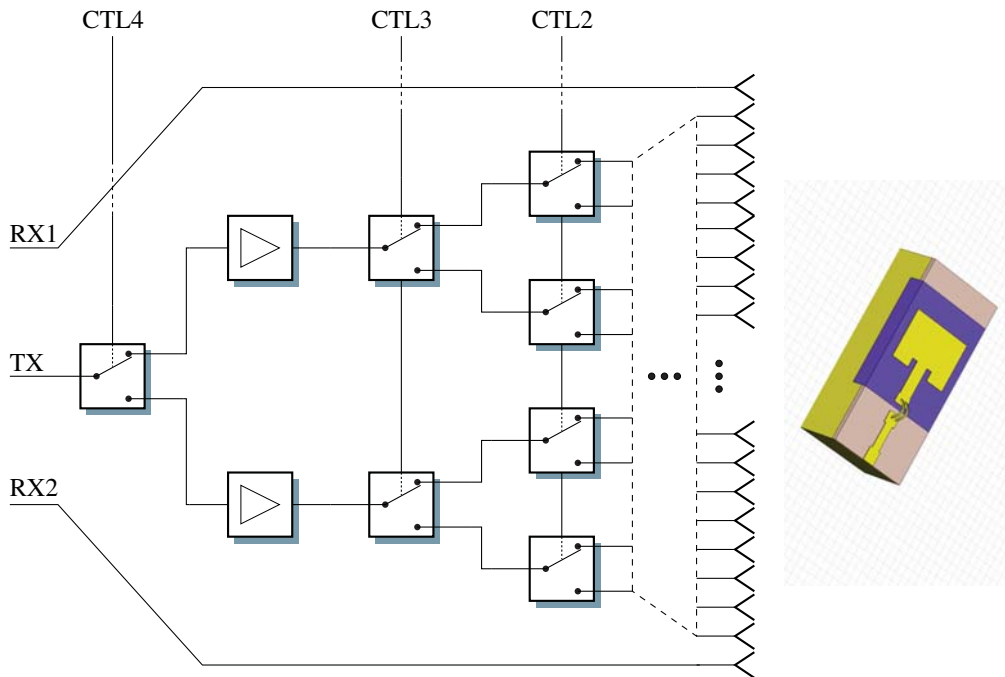


**Fig. 4.2:** Block diagram of the switched antenna array (left); schematic of an embedded patch antenna (right).

first stage two amplifiers [69] are inserted to compensate for transmission line and switch insertion losses. 32 transmitting antennas are connected to the network and one receiving antenna is placed on each side of the transmitting array. As explained before, this configuration forms an equivalent aperture, which is about twice the geometrical size of the array aperture [70, 8]. Again, the mm-wave circuit is implemented on the PTFE-based metal backed substrate Taconic TaclamPlus [44]. The height of this substrate is only 0.1 mm. As the required relative bandwidth of the antenna elements is about 10%, the 34 patch antennas are fabricated on an embedded Taconic TLX-9 substrate with a height of 0.38 mm (cf. Fig. 4.2). The connection between the switching circuit and the patch antennas is made by wire bonding.

Figure 4.3 shows the hardware of the switched array. The actual mm-wave circuit is covered by a standard FR-4 PCB providing DC supply and bias for amplifiers and switches through spring loaded pins. An opening of sufficient size is cut into this PCB to allow the patch antennas radiating without perturbation.

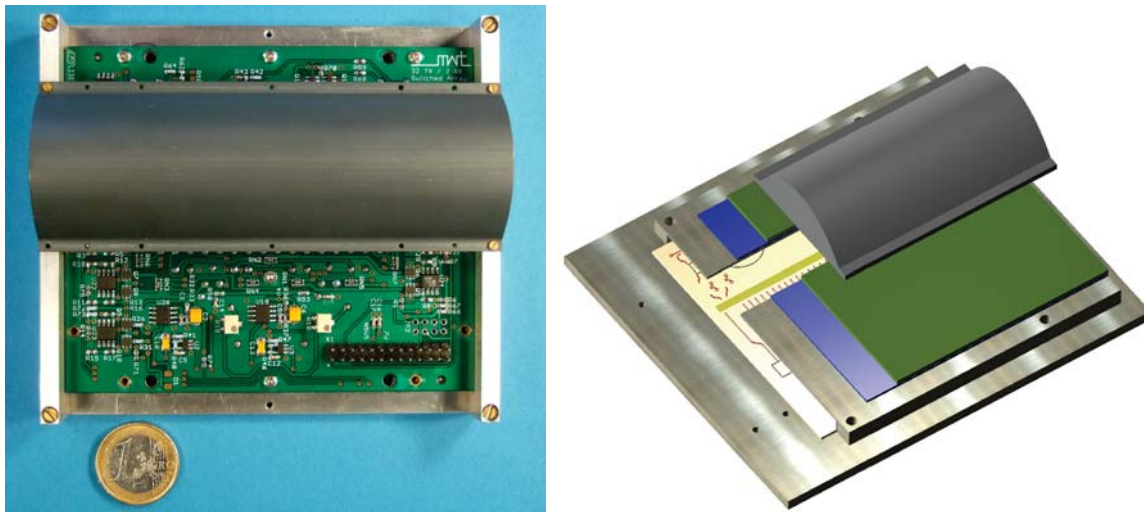


**Fig. 4.3:** Photograph (left) and CAD model (right) of the active switched patch array; both pictures include the cylindrical lens necessary for a narrow  $E$ -plane beamwidth.

Design and optimisation of the embedded patch antenna have been done using CST Microwave Studio [71]. The spacing of the antenna elements is chosen to 1.95 mm which provides a  $\pm 60^\circ$  unambiguous field of view at 83 GHz.

Due to the thick antenna substrate and the joint design of the patch and the network compensating for the bond wire inductance a wide impedance bandwidth could be achieved (Fig. 4.4).

Within the frequency range from 73 GHz to 81 GHz the simulated return loss of a single patch antenna is better than 27 dB. The respective measurements were done using a scalar network analyser with a WR-12 waveguide interface. Hence, a deembedding of the waveguide-to-microstrip transition is not possible. This is why the experimental results are mainly determined by the waveguide transition the return loss of which is also shown in Fig. 4.4. However, even including the waveguide transition the patch radiator shows a sufficient performance.

## 4.2 Cylindrical Lens Design and Farfield Characteristics

To achieve a narrow beamwidth in the plane perpendicular to the array, a cylindrical lens was designed, the cross section of which is shown in Fig. 4.6 (left). Typical mm-wave lenses found in literature have a spherical-convex profile with the spherical side facing the primary source or plane-convex profiles where the

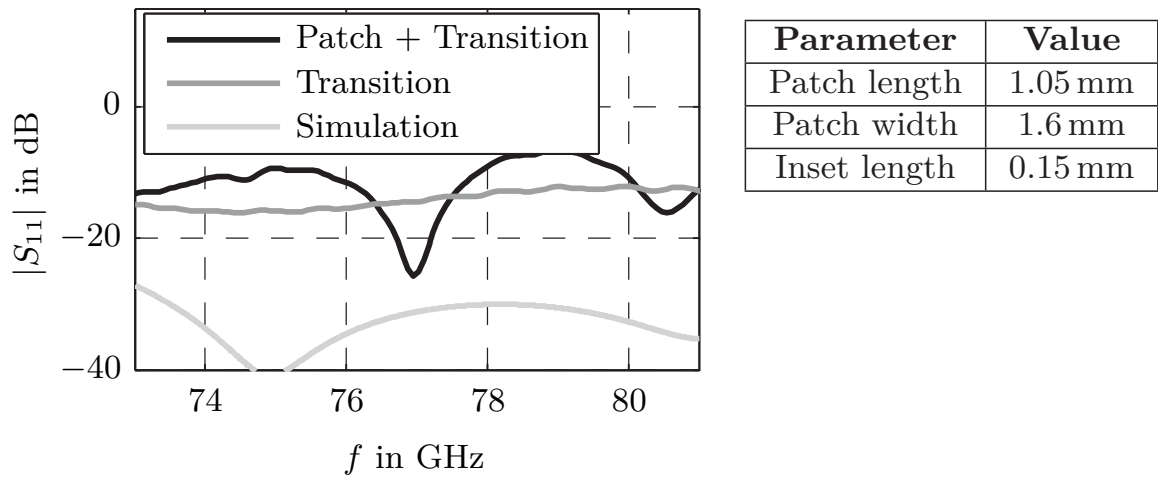


**Fig. 4.4:** Simulated and measured return loss of a single patch antenna (left) and key parameters of the patch geometry (right); the measured behaviour is mainly determined by the microstrip-to-waveguide transition.

source is located on the convex side. The advantage of these types of lenses is the availability of an analytical expression for the description of the profile.

Due to the short focal length required in the given setup and the ease of fabrication the above mentioned types are not applicable. Instead, the plane-convex arrangement in Fig. 4.5 was chosen, for which no closed analytical solution exists.

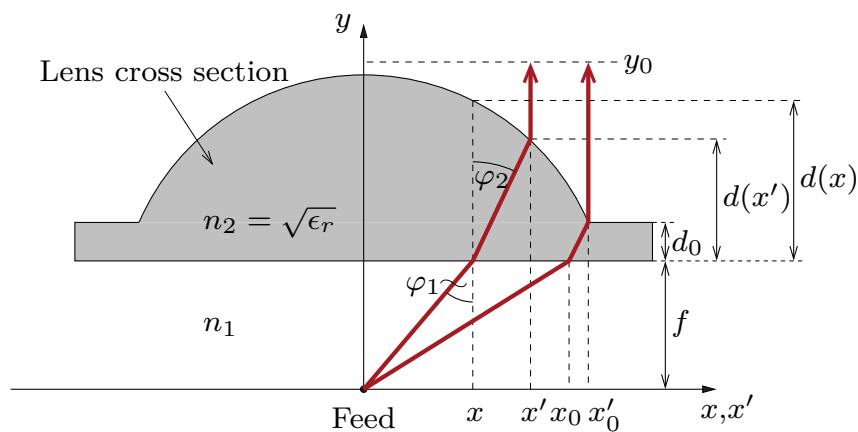


**Fig. 4.5:** Parameter definition for the computation of the plane convex lens design.

The lack of an analytical solution is caused by the twofold refraction at the air-dielectric interfaces leading to a transcendent equation. According to Snellius' law the relation between the angles  $\varphi_1$  and  $\varphi_2$  in Fig. 4.5 is

$$\frac{\sin(\varphi_2)}{\sin(\varphi_1)} = \frac{n_1}{n_2}, \quad (4.1)$$

where  $n_1 = 1$  and  $n_2 = \sqrt{\varepsilon_r}$  are the refractive indices of air and the dielectric material of the lens with the relative permittivity  $\varepsilon_r$ . To achieve a plane wave, the electrical lengths of all rays must be the same with respect to an arbitrary plane  $y = y_0$  perpendicular to the  $y$ -axis. Taking the ray hitting the lens at  $x = x_0$  as a reference gives

$$\begin{aligned} n_1 \sqrt{x_0^2 + f^2} + n_2 \frac{d_0}{\cos(\varphi_2(x_0))} + n_1 (y_0 - d_0) = \\ n_1 \sqrt{x^2 + f^2} + n_2 \frac{d(x')}{\cos(\varphi_2(x))} + n_1 (y_0 - d(x')). \end{aligned} \quad (4.2)$$

By solving for the lens thickness  $d$  at a position  $x'$  the position of the constant phase line  $y = y_0$  cancels out. Finally, the lens profile is obtained as

$$d(x') = \frac{n_1 \sqrt{x^2 + f^2} - n_1 \sqrt{x_0^2 + f^2} - n_2 \frac{d_0}{\cos(\varphi_2(x_0))} + d_0 n_1}{n_1 - \frac{n_2}{\cos(\varphi_2(x))}}. \quad (4.3)$$

It must be noted that for fabrication the lens thickness has to be known as a function of  $x'$ , but the right hand side expression still depends on  $x$ , where  $x'$  relates to  $x$  as

$$x' = d(x') \tan(\varphi_2(x)) + x. \quad (4.4)$$

As mentioned before, substituting (4.4) in (4.3) does not yield a closed expression. The solution is numerically calculating the lens contour for closely spaced values of  $x$  and map the results to the respective position  $x'$ .

Periodic gratings are used on the flat side of the lens in order to reduce reflections at the air-dielectric interface. The profile and the scattering parameters of this matching layer are shown in Fig. 4.6. The return loss of the matching layer is better than 30 dB within the relevant frequency range. As the dielectric losses are negligible for the thin anti-reflection layer, the transmission is very close to 0 dB. For ease of fabrication the matching layer is omitted at the convex interface of the lens.

The farfield measurement of the patch antenna without the cylindrical lens (Fig. 4.7 (left)) shows a good agreement with the simulated results. The ripple

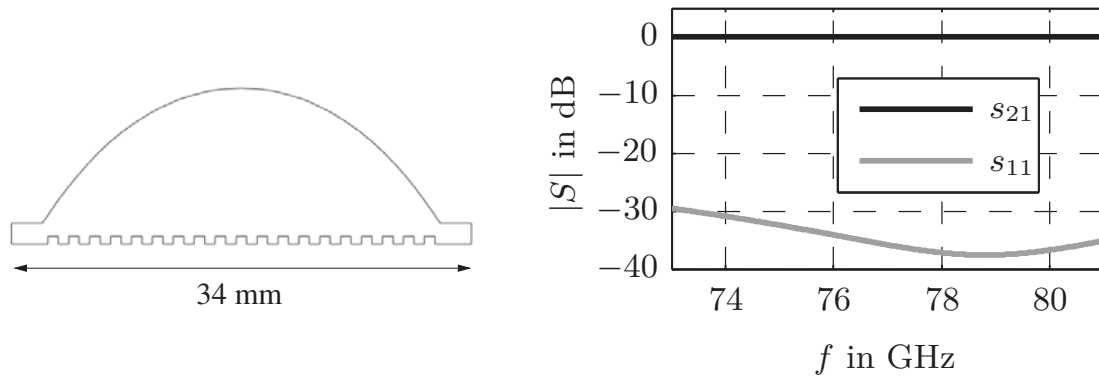


**Fig. 4.6:** Cross section of the cylindrical lens with periodic gratings as matching layer on the flat side (left); simulated scattering parameters of the matched air-dielectric interface (right).

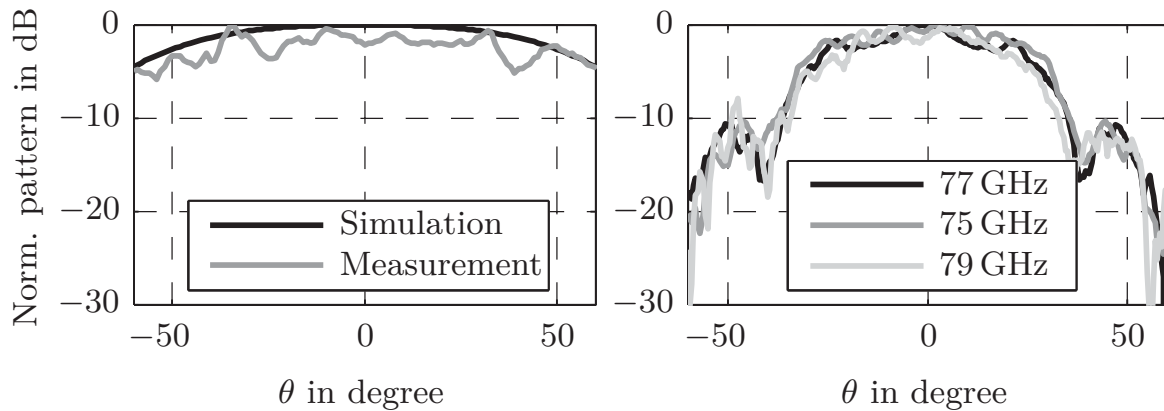


**Fig. 4.7:** Measured H-plane radiation pattern of a single patch antenna (left) and the cylindrical lens illuminated by a patch (right).

occurring in the measured pattern is caused by spurious radiation occurring at the edges of the finite substrate.

The intention when designing the cylindrical lens was to preserve the antenna pattern of the primary source in the H-plane and to focus the beam in the E-plane. In Fig. 4.7 (right) a degradation of the pattern can be observed when including the cylindrical lens. This is because cylindrical lenses only behave in the desired way, if they are sufficiently thin. In case of thick lenses, the spherical wave originating from the primary source is disturbed by the twofold refraction at the air-dielectric interfaces due to a migration of the virtual phase centre (cf. Fig. 4.8). In the described setup the focal length is very small ( $F = 15$  mm)

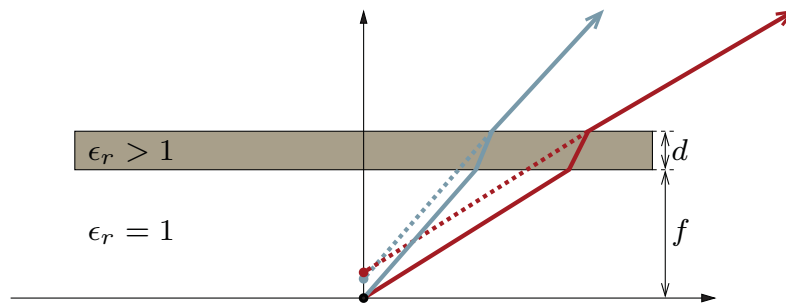


**Fig. 4.8:** Raytracing through a dielectric plate leads to an angular dependent migration of the virtual phase centre.

and the thickness of the lens is up to 15 mm. Hence, a degradation can be expected.

Due to the reduced 3 dB beamwidth the field of view of the switched array is limited to  $\pm 30^\circ$ . This is sufficient for the applications having in mind here. However, one possibility to overcome the effects of a thick lens could be in using a Fresnel design.

In the E-plane, a narrow beamwidth of  $5^\circ - 6^\circ$  is achieved (cf. Fig. 4.9). Even though there is an amplitude tapering down to  $-8$  dB at the edges of the lens,

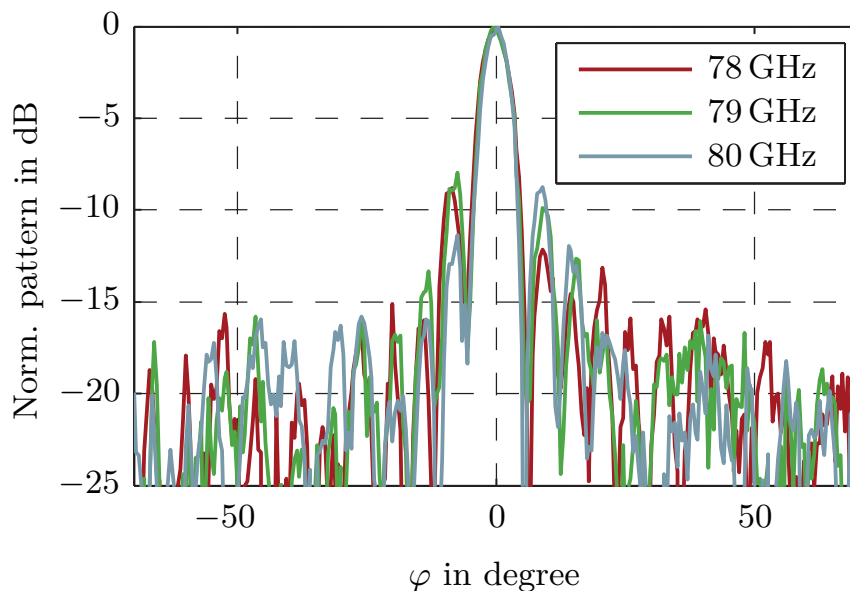


**Fig. 4.9:** Measured radiation pattern of the cylindrical lens illuminated by a single patch (E-plane).

the sidelobe attenuation is in the order of 10 dB–13 dB. This is much less than theoretically expected. The reason can also be found in the large thickness of the lens.

As the array is intended to be operated over a wide frequency range, the antenna gain of the active switched array has been measured as a function of the frequency. Figure 4.10 shows the results of some representative switching states, activating the patch 8, 14, or 19. As a reference the performance of a passive patch antenna is also depicted. The term “passive” means that there is no switching network influencing the behaviour. In both cases the setup included the cylindrical lens.

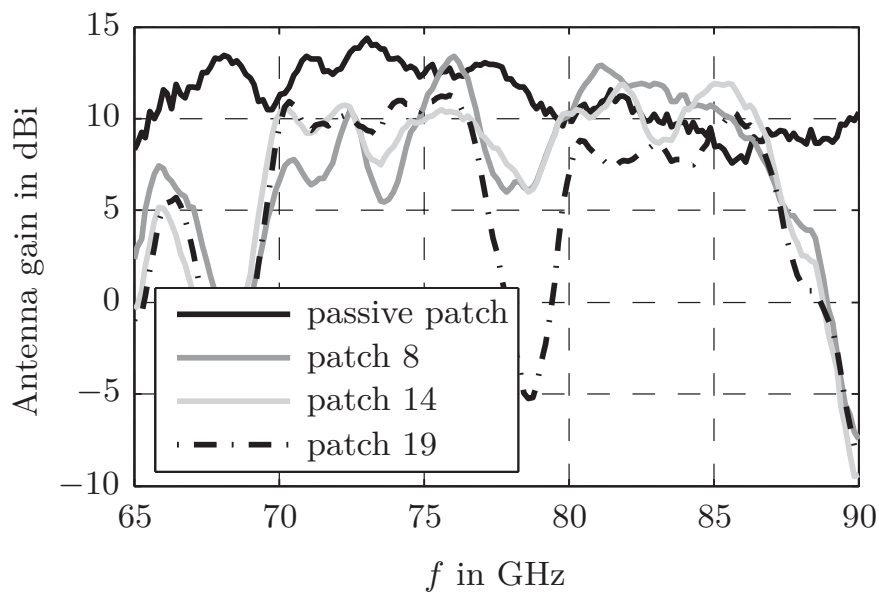


**Fig. 4.10:** Measured antenna gain over frequency for three different switching states and patches.

The passive antenna shows a flat response within the desired range from 73 GHz to 81 GHz. The maximum ripple is  $\pm 2$  dB. For the active array, the amplifiers almost compensate for the losses occurring within the switching network. A significant drop around 79 GHz is apparent for all states, but the depth strongly depends on the switching state as visible in Fig. 4.10. As the RF circuit is perfectly symmetric, the switches are most likely to be responsible for this behaviour. As an example an imperfect isolation of a switch in the last stage would lead to a spurious radiation of the adjacent patch. However, in this case the drop in the frequency response would change as a function of the angle. This could not be verified during the measurements (cf. Fig. 4.11).

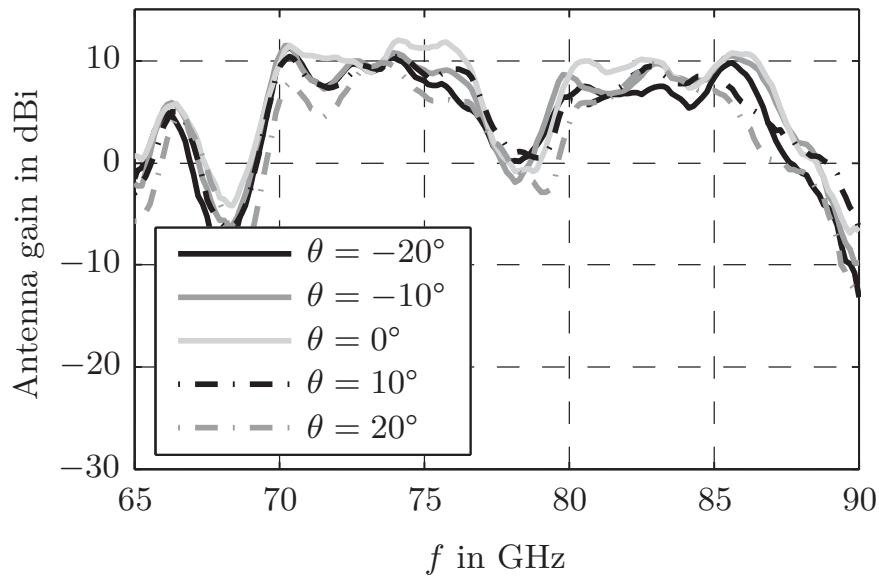


**Fig. 4.11:** Measured antenna gain over frequency for a single switching state and different angles  $\theta$ .

It has also been noticed that the forward bias voltage of the PIN-diodes varies among the switches. This indicates that some of them are not operating properly. Additionally, the switches are designed for narrowband automotive applications from 76 GHz to 77 GHz and no wideband scattering parameters are available. However, the problem is not related to the system concept or the mm-wave circuit and antenna design. In the future, PIN-diode switches may be replaced by wideband and low loss MEMS-based designs as presented e.g. in [72, 73].

### 4.3 Coarray-based Beamforming for not Fully Populated Arrays

The equivalent aperture approach based on using one receive antenna on each side of the transmit array improves the angular resolution. When looking closer to the equivalent antenna configuration it turns out that there is a gap at the centre location. As a consequence, the application of the delay-and-sum beamformer – which was shown to be closely related to the discrete Fourier transform – yields a minimum sidelobe level that is in the order of  $-30$  dB compared to the maximum, even though appropriate windowing is used (s. Fig. 4.13). The explanation is that the missing “sample” in the spatial domain can be expressed as a Dirac-shaped perturbation with a broadband spectrum. An interpolation of amplitude and phase of the missing element cannot solve the problem in multi-target scenarios, even though the application of AR models can improve the results [62].

From the spectral estimation point of view, the Bartlett beamformer is a periodogram-based estimator (cf. Section 2.3). That means that the PSD is obtained by squaring the Fourier spectrum of the signal. Correlogram-based estimators are equivalent (provided the autocorrelation sequence is known), even if they are typically not used in connection with digital beamforming. This fact is exploited hereinafter.

The term “coarray” is known from investigating the properties of sparse arrays [74] and is simply the autocorrelation sequence of the antenna distribution. For optimum performance over a  $\pm 90^\circ$  field of view this coarray should not contain any gaps larger than half the wavelength. If minimum redundancy is required, not more than one pair of antennas is allowed to contribute to each lag of the autocorrelation sequence (except the zeroth lag, as always all antennas contribute to this). Even though this work does not deal with sparse arrays, the coarray concepts helps understanding and mitigating the effect of the aperture gap.

Figure 4.12 compares the coarray of a fully populated array and a notched array where the centre element is missing. In both cases the unbiased, windowed technique for the calculation of the autocorrelation sequence is used, which gives  $2M - 1 = 129$  autocorrelation lags out of  $M = 65$  samples. For the full array the coarray is constant and equal to one. The coarray of the notched configuration shows some deviations. The reason is that the calculation of the correlation sequence is based on averaging. However, in case of a missing sample the number of samples available for averaging does differ from the number that is assumed to be available. For the zeroth lag the error is  $\frac{1}{65}$ , for the first lag  $\frac{2}{64}$ , for the third lag  $\frac{2}{63}$  and so on. Starting from the 33th lag the centre gap is no longer included in the calculation.

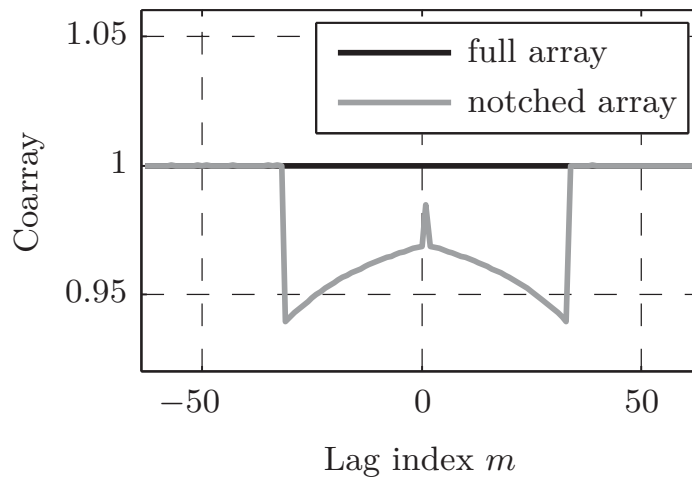


**Fig. 4.12:** Unbiased coarray estimates of a fully populated uniform linear array and an array with the centre element missing.

Considering the aperture's coarray shows that the missing antenna element leads to a weighting of the autocorrelation sequence, that is independent of the measured data and is easily compensated for by applying the inverse weights. Once the correlation sequence is corrected, the PSD of the angular spectrum is the discrete Fourier transform of this sequence. Using an adequate window the side lobe attenuation is no longer restricted to  $-30$  dB.

Figure 4.13 shows a comparison of the results obtained for a notched array, a fully populated array and using the corrected coarray approach. In all cases a Chebyshev window with 40 dB sidelobe attenuation was applied. The shape of the main beam is the same for all examples, but differences are seen regarding the sidelobes. For the notched array the average relative sidelobe level is in the order of  $-30$  dB, whereas for the full array and the coarray correction the maximum sidelobe level is given by the Chebyshev window. The positions of the sidelobes' maxima and minima do not coincide in the latter two cases. The reason is that the length of the correlation sequence is  $2M - 1$  compared to the size  $M$  of the array. Consequently, the separation between the minima and maxima is only half in case of the coarray approach.

The above described technique is not only restricted to correlation sequences but also to correlation matrices. Whenever using an adaptive technique that relies on the correlation matrix, its coefficients should be corrected by the inverse of the coarray.

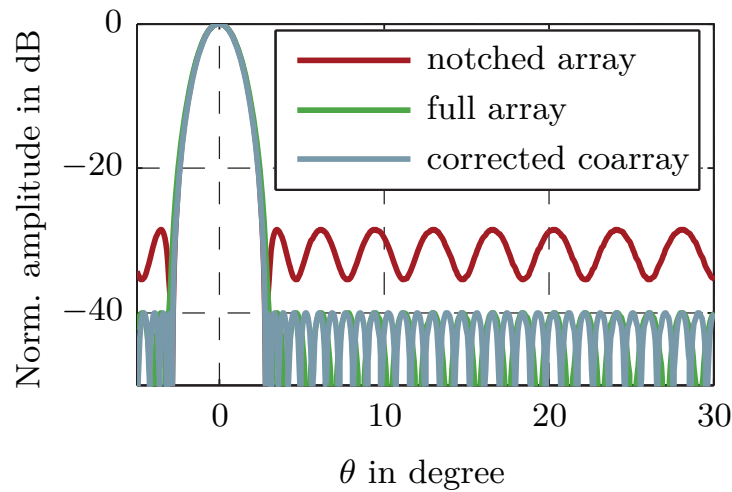


**Fig. 4.13:** Digitally formed beam patterns using a full array, a notched array and the compensated coarray approach.

## 4.4 Measurement Results Obtained with the Switched DBF Sensor

The switched array has been combined with the broadband dual channel FM-CW frontend described in Chapter 3. To compensate for systematic phase errors, a calibration of the sensor is necessary. A very simple approach is to use a point scatterer in boresight direction situated in a low reflective environment, e.g. an anechoic chamber. The deviations from the ideal constant phase response are stored and used for the calibration of the actual measurement. Due to the inherent symmetry of the switching network and the equal delay of all paths, the phase errors are noticed to be very small. However, a precise calibration is needed to achieve a low sidelobe level.

### 4.4.1 Measurement of Point Scatterers

As a first measurement scenario three corner reflectors have been arranged in an anechoic chamber. A picture of the setup together with the most important sensor settings are found in Fig. 4.14. In all static scenarios the slow mode is used in order to improve the signal-to-noise ratio. The results obtained by the beamforming techniques described in Section 2.6 are shown in Fig. 4.15 and Fig. 4.16. The resolution (measured at  $-3$  dB) achieved with the conventional beamformer is about 6 cm in range and  $2.4^\circ$  in the angular dimension. This

Parameter	Value
Sweep bandwidth	74 GHz–80 GHz
Pulse duration (slow/fast mode)	600 $\mu$ s/160 $\mu$ s
Acquisition time (slow/fast mode)	19.2 ms/5.1 ms
Range sidelobes	–80 dB (Chebyshev window)
Angular sidelobes	–40 dB (Chebyshev window)

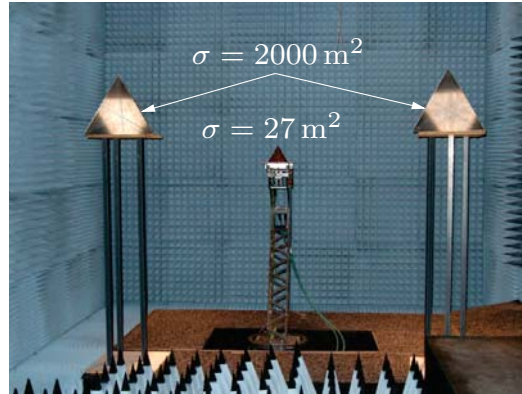


**Fig. 4.14:** Typical sensor settings (top) and scenario consisting of three objects located in an anechoic chamber (bottom). Given are the radar cross section (RCS) values of the corner reflectors.

matches the theoretically expected values given by bandwidth, aperture size, and the applied window functions.

The adaptive weights for the Capon beamformer have been calculated using a  $32 \times 32$  correlation matrix estimated out of the 64 measured channels, and the coarray correction (cf. Section 4.3) was applied to obtain an accurate estimate. The size of the correlation matrix implies that the effective aperture size used for Capon’s method is only half the aperture size employed for the conventional beamforming. Nevertheless, the adaptive beamformer shows superior performance compared to the conventional one.

As derived in Section 2.6, eigenvalue based methods extract parameters of complex harmonic signals (cisoids) using the eigenstructure of correlation matrices. These cisoids are represented either as a pseudospectrum having sharp peaks at the respective angular frequency (MUSIC) or as a line spectrum (ES-PRIT). Hence, a direct comparison to adaptive or non-adaptive methods in terms of 3 dB width and sidelobe level of the beamformer response is not appropriate. However, the improvement of the resolution becomes evident by inspecting Fig. 4.16. In case of MUSIC the “weighted” version is used in order to reduce the sensitivity to noise. The best results are obtained with the dimension of the

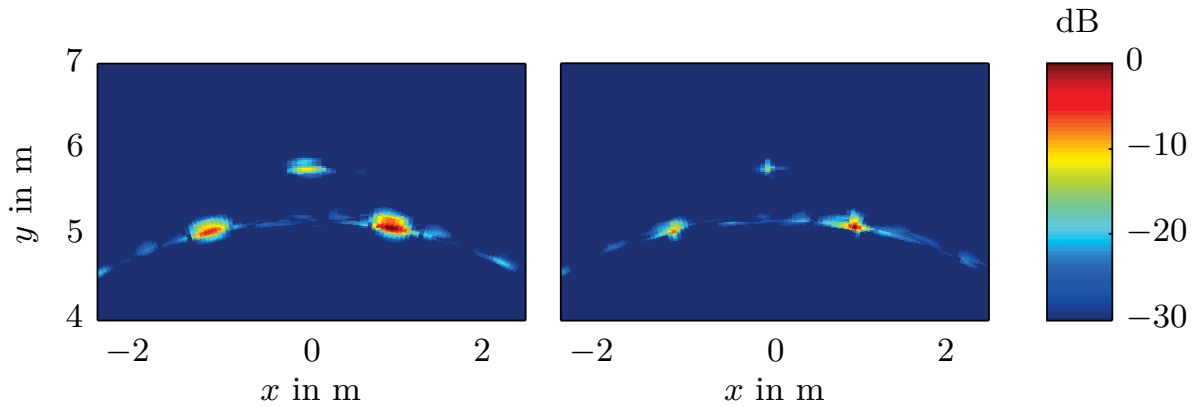


**Fig. 4.15:** Radar measurement of the scenario in Fig. 4.14 processed with delay-and-sum beamforming (left) and Capon's method (right).

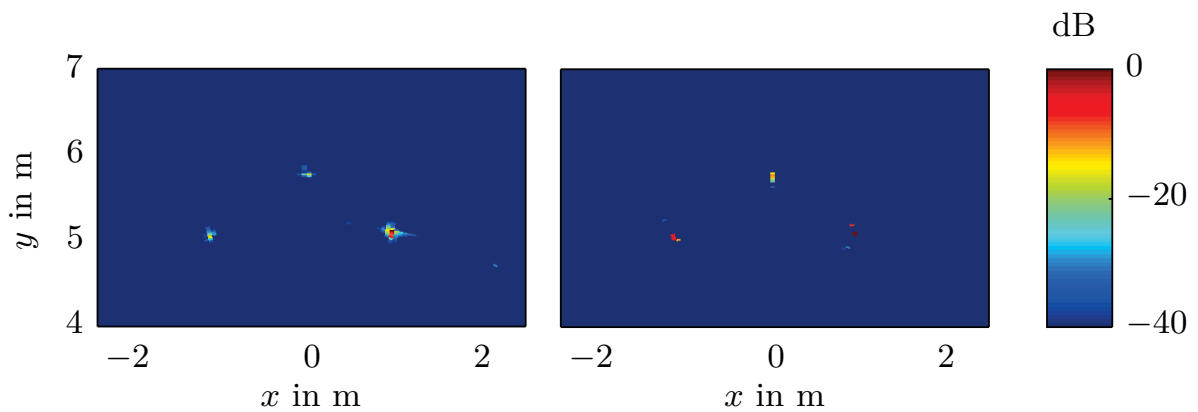


**Fig. 4.16:** Radar measurement of the scenario in Fig. 4.14 processed with ESPRIT (left) and MUSIC (right).

correlation matrix being 16. Within the MUSIC algorithm it is mandatory to estimate the dimension of the signal subspace. A dynamic approach is used here where the smallest eigenvalue is multiplied by 5 to obtain the threshold between the eigenvalues representing the signal and noise subspace. Additionally, the signal subspace dimension is limited to 8 which gives a maximum of 8 detectable point scatterers.

The ESPRIT algorithm also yields only a limited number of cisoids which is one less than the dimension of the correlation matrix. The latter one is chosen

to be 10. This is much smaller as for the Capon beamformer, but yields a better correlation estimate as a higher number of subarrays can be used for averaging (cf. Appendix A.4 on page 131). Even when using a good estimate ESPRIT can yield eigenvalues that are not related to cisoids. However, those eigenvalues are located far off the unit circle in the complex domain. Similar to MUSIC a thresholding is implemented neglecting all eigenvalues with a distance of greater than 0.1 to the unit circle.

#### 4.4.2 Measurement of a Complex Environment

The limitation to a smaller number of targets seems to be quite appropriate in scenarios like that one shown above. The application to more complex scenarios is demonstrated using measurements taken in the environment shown in Fig. 4.17 from the sensor's perspective.

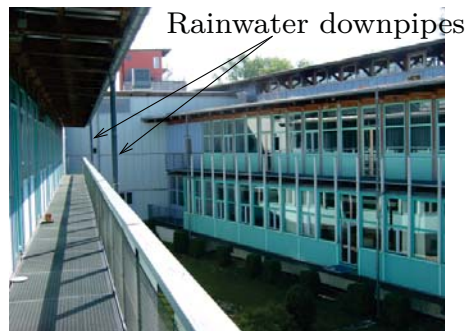


**Fig. 4.17:** Measurement scenario situated between two buildings from the sensor's perspective.

The results after delay-and-sum and minimum variance beamforming shall serve as a reference. In addition to the beamforming the output is normalised by the local noise and clutter level, which is obtained using a two-dimensional cell averaging as done for the CFAR processor described later in Section 5.1.2. Hence, the graphs in Fig. 4.18 show the signal-to-clutter-and-noise ratio (SCNR). For both methods similar features of the environment are visible, such as the rainwater downpipes and the periodic reflections caused by the window frames of both buildings. Again, the Capon beamformer provides a better angular resolution compared to the conventional beamformer, which becomes apparent especially for greater distances.

Even though the number of targets per range cell is limited, the eigenvalue-based methods perform quite well in the given environment (cf. Fig. 4.19) and the angular resolution is much better than for the conventional and the Capon

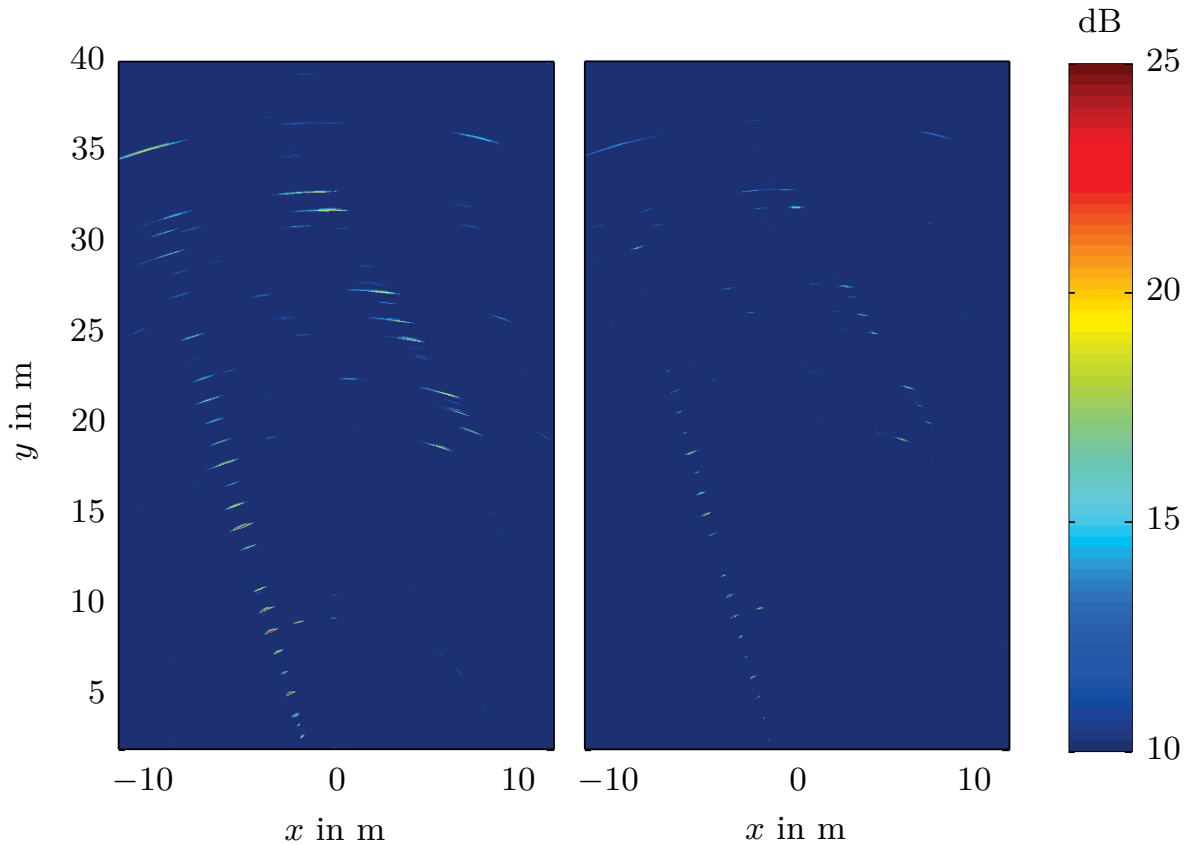


**Fig. 4.18:** Radar measurement of the scenario in Fig. 4.17 processed with delay-and-sum beamforming (left) and Capon's method (right); the viewgraphs show the SCNR obtained by averaging the local clutter and noise level.

beamformer. Due to the discrete nature of the scatterers obtained by MUSIC or ESPRIT a normalisation by the local clutter or noise is not applicable. It has been noticed that the performance of the eigenvalue-based methods degrades when decreasing the bandwidth. The obvious reason is that the number of point scatterers within one range cell scales with the range resolution and reaches the limit given by the dimension of the correlation matrix. Even though ESPRIT seems to provide the sharpest radar image, some noise can be seen in the centre area between the two buildings. This could have been accomplished by adjusting the threshold closer towards the unit circle or by reducing the dimension of the correlation matrix and thereby improving its estimate. However, both approaches would diminish the sensitivity to real scatterers as well. Consequently, a trade-off has to be found for a given signal-to-noise ratio.

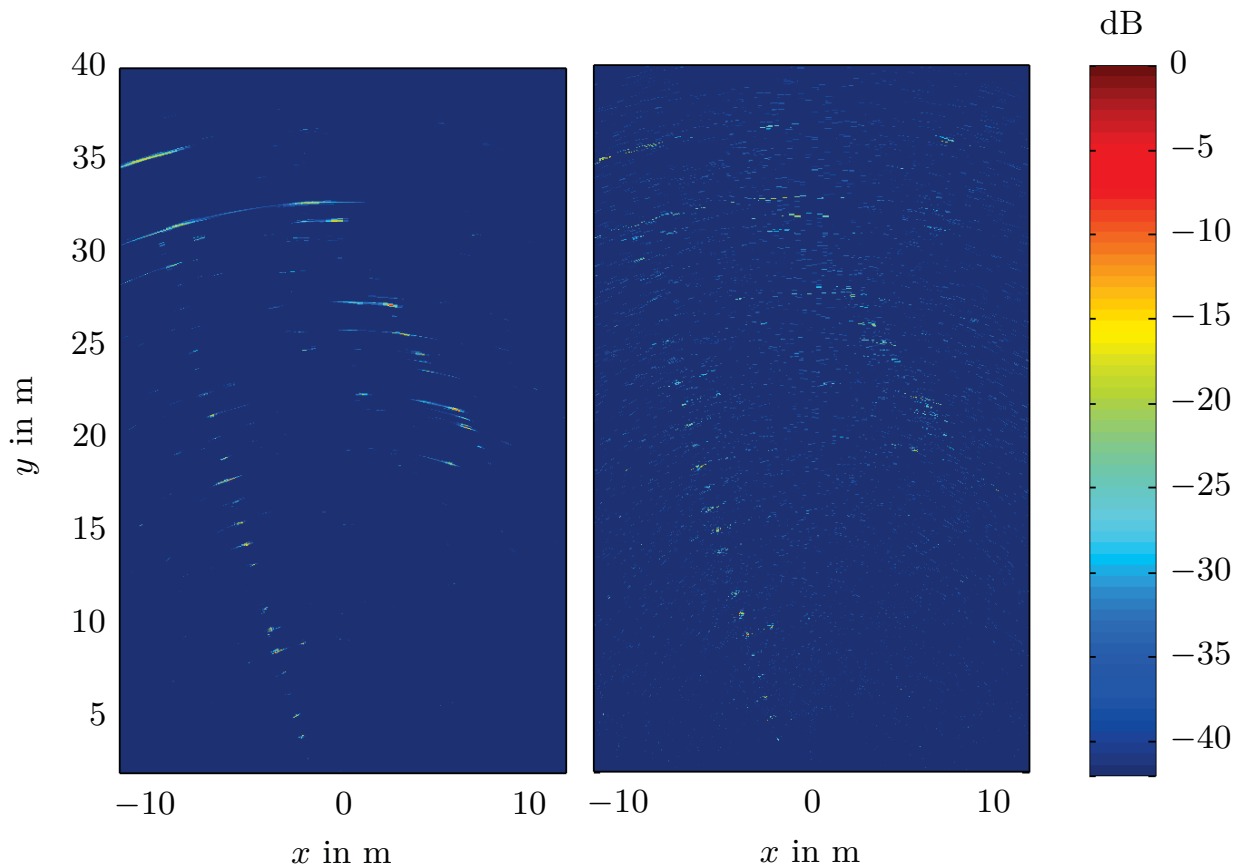


**Fig. 4.19:** Radar measurement of the scenario in Fig. 4.17 processed with MUSIC (left) and ESPRIT (right).

## 4.5 Imaging of Moving Targets using a Switched Sensor Array

For static scenarios, parallel and sequential acquisition of the array channels are equivalent. In time variant environments the position of the target  $r_m$  in the data model (equation (2.74) on page 39) changes with time. Hence, the data model gets time dependent as well [75, 76].

As derived in Section 2.6 the magnitudes of the data model coefficients are all one for ULA setups. So the phase is the only parameter yielding information about the target's angular offset and speed. Let the switching sequence  $t_x(x_m)$  be a function that describes, at which time  $t_x$  the element at the position  $x_m$  is acquired. Then the total phase at the output of the array elements is given by

$$\Phi_\theta(x_m) = k_0 \cos(\theta) x_m, \quad (4.5)$$

$$\Phi_v(x_m) = 2 k_0 v t_x(x_m), \quad (4.6)$$

$$\Phi_t(x_m) = \Phi_\theta(x_m) + \Phi_v(t_x(x_m)), \quad (4.7)$$

with  $\Phi_\theta$  and  $\Phi_v$  being related to the angular offset and the target velocity, respectively.

Assuming a uniform linear switching sequence  $t_x(x_m) = k_{\text{sw}} x_m + T_{x,0}$  the phase at the  $m$ th element amounts to

$$\Phi_t(x_m) = k_0 \cos(\theta) x_m + 2 k_0 v (k_{\text{sw}} x_m + T_{x,0}). \quad (4.8)$$

Two consequences can be found from this equation. Firstly, for an unambiguous representation of the signal it is necessary to avoid phase differences greater than  $\pi$  between two adjacent antenna elements. Hence, the relation

$$\Delta x = x_{m+1} - x_m < \frac{\lambda - 4v\Delta t_x}{2|\cos(\theta)|} \quad (4.9)$$

has to be fulfilled for all angles of incidence within the field of view of the antennas, where  $\Delta t_x = t_x(m+1) - t_x(m)$  is the time delay between the sampling of the two antennas at  $x_m$  and  $x_{m+1}$ . This is an extended or generalised formulation of the spatial sampling theorem used in static scenarios.

Secondly, both the target Doppler shift and the angular offset lead to a linear slope of the phase as shown in Fig. 4.20 (left). A given total phase  $\Phi_t$  can be caused by an infinite number of possible speed/angle pairs. Without any further information, the contributions cannot be separated. As the antenna position is usually fixed, the only way to gain more information is changing the switching sequence. The problem is closely related to the separation of range and Doppler in FM-CW processing, where e.g. a triangular modulation scheme is used. The same technique would be applicable here, as a positive  $k_{\text{sw}}$  leads to an increase of the spatial frequency and a negative  $k_{\text{sw}}$  decreases it. In multi-target scenarios, the problem remains, how to resolve ambiguities in the angle/Doppler domain.

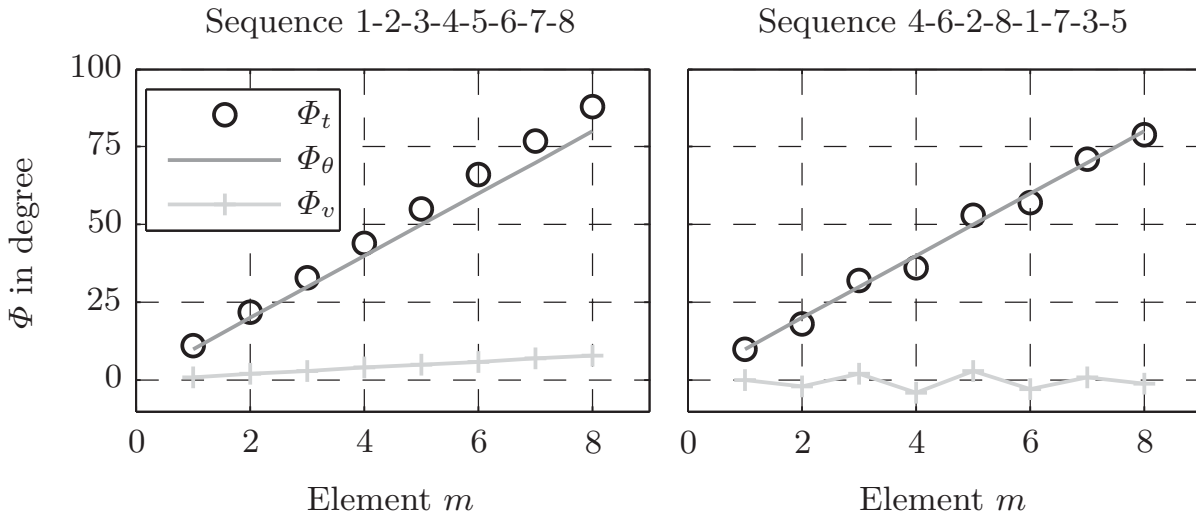


**Fig. 4.20:** Contribution of target motion ( $\Phi_v$ ) and angular offset ( $\Phi_\theta$ ) to the overall phase at the antenna elements for the different switching sequences indicated on top of the viewgraphs.

#### 4.5.1 Optimised Switching Sequence for Reduced Doppler Sensitivity

A different approach to mitigate the Doppler sensitivity of a switched sensor arrangement is by choosing the switching sequence in a way, that no ambiguities occur, and ghost targets are reduced or shifted to angular positions outside the intended field of view [77]. The procedure is illustrated in Fig. 4.20. The right viewgraph shows the contributions of angular offset and Doppler to the overall phase distribution. The sequence is chosen such that the average phase shift caused by the Doppler is zero. Hence, a linear interpolation of the acquired phase values leads to a phase slope related to the correct angular position. The deviation from the linear slope can be considered as a phase modulation of the harmonic signal obtained for static targets. It is obvious, that the shape and amplitude of this “modulation signal” defines the degradation caused by the Doppler. Figure 4.21 shows the phase modulation for the switching sequence chosen in Fig. 4.20 (right).

Due to the alternating sign of the phase error (cf. Fig. 4.21 (left)), the distance between the modulation sidebands and the desired signal in the angular spectrum can be expected to be large. In addition, the tapering of the phase error leads to a narrow angular extent of the undesired ghost targets. Simulations have been conducted for different target velocities. Thereby, the sensor parameters are set to the fast mode (cf. Fig. 4.14) in order to allow a higher target

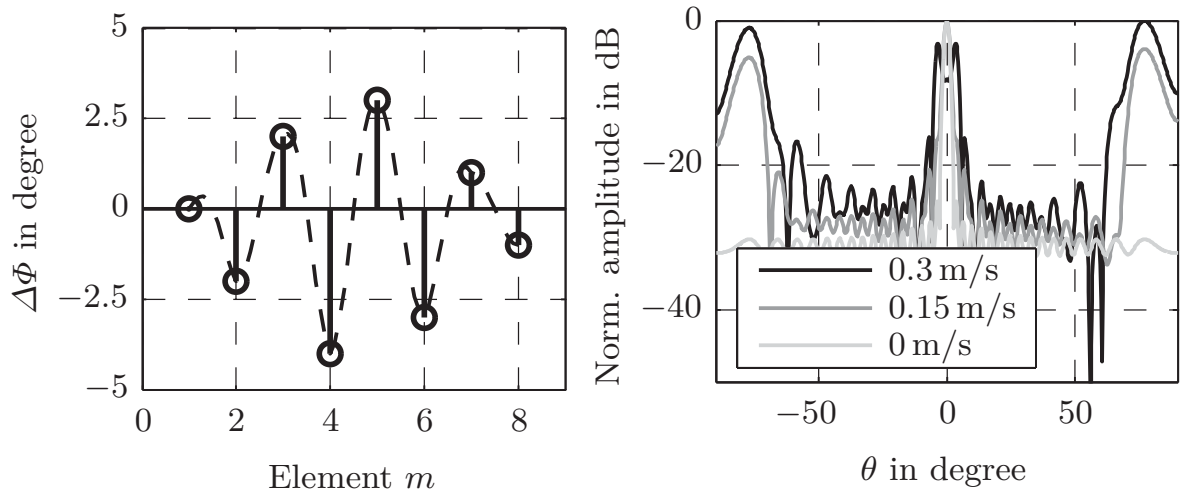


**Fig. 4.21:** Phase error introduced by the target motion when using the optimised switching sequence (left); beamformer response for different target velocities (right).

velocity. The respective angular spectra (Fig. 4.21 (right)) and two dimensional radar images (Fig. 4.22) prove that the intended properties could be achieved.

In case of the linear switching sequence, the expected angular migration caused by the linear slope of the phase error can be seen in Fig. 4.22 (left). The split target observed for  $v = 0.15 \frac{\text{m}}{\text{s}}$  is due to the equivalent aperture formed by the two receiving antennas. For each half of this equivalent aperture the phase error is like that one in Fig. 4.20 (left). Hence, there is a discontinuity at the centre of the array, leading to a Doppler induced phase modulation that can be described as two periods of a sawtooth waveform.

When considering the results for the optimised sequence at lower speeds, the shape of the main beam does not change considerably, and only a small increase of the sidelobe level can be observed. Two symmetric ghost targets arise at an angular offset of more than  $60^\circ$ . As the target speed increases the level of the sidelobes and the ghost targets rises. Additionally, the main peak starts to split into two separate peaks. It has been determined that the maximum allowable radial translation of the target is a quarter wavelength during the complete measurement.

The results obtained by means of simulation could be confirmed by measurements. For that purpose a corner reflector has been attached to a linear actuator in order to perform a radial motion with respect to the radar sensor. The measurement results in Fig. 4.23 match the theoretically expected results for both the standard and the optimised switching sequence. On the one hand, this proves the feasibility of improving the Doppler sensitivity by adapting the

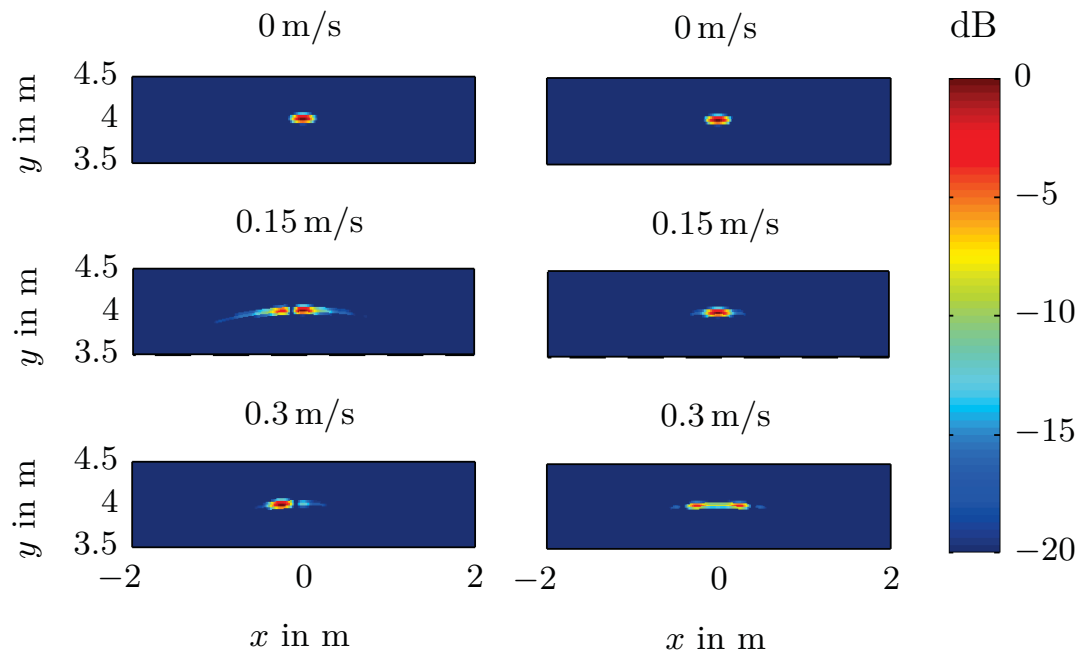


**Fig. 4.22:** Simulated beamformer response for different target velocities using the linear (left) or the optimised (right) switching sequence.

switching sequence. On the other hand, it confirms that the simulation model is reliable also for dynamic scenarios.

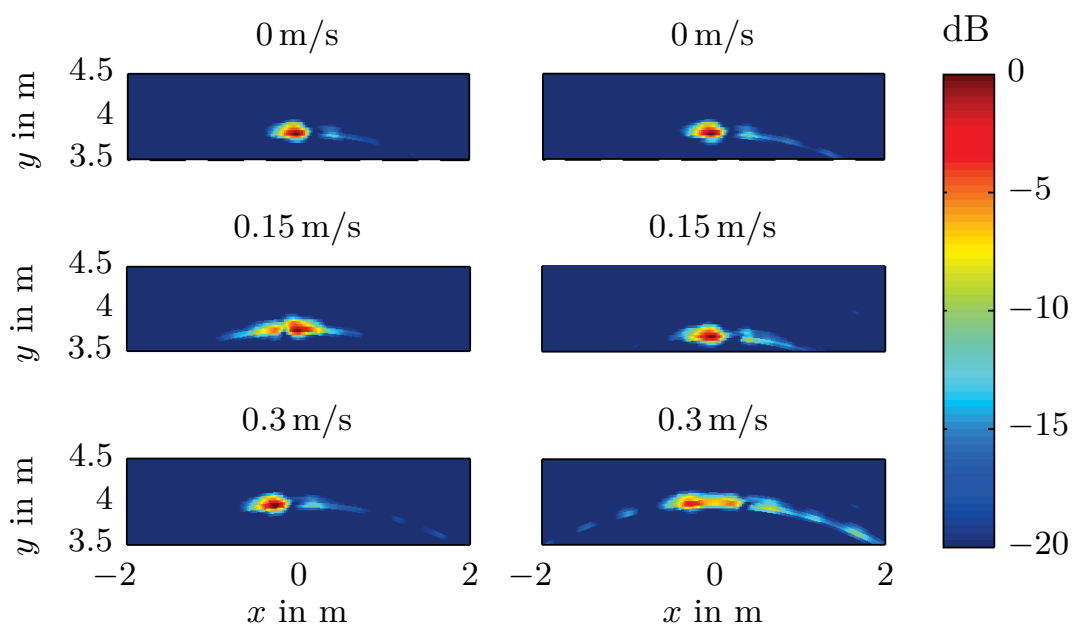


**Fig. 4.23:** Measured beamformer response for different target velocities using the linear (left) or the optimised (right) switching sequence.

### 4.5.2 ESPRIT-based Subarray Approach for Doppler Mitigation

In Section 2.6.4 it has been shown that the ESPRIT algorithm relies on the auto- and crosscorrelation of two identical subarrays. Thereby, the actual array manifold is not of importance as long as the subarrays can be transformed into each other by a known linear translation. Of course, the spacing between the subarrays has to be small enough to avoid ambiguities. For a  $\pm 90^\circ$  coverage of the array this restriction leads to a spacing of half a wavelength. For static scenarios the subarrays are created by considering the array elements  $1 \dots M-1$  or  $2 \dots M$ . In a switched configuration the measurements of these subarrays are taken at different times. Hence, the matrix describing the effect of the spatial translation incorporates the influence of both the angular offset and the velocity of the target. This means by using the ESPRIT algorithm in this way no advantage is gained with respect to angle/Doppler ambiguity.

In the described system both subarrays of the equivalent aperture are acquired at exactly the same time. That means that there is only an *intrinsic* phase error within each subarray. The translation matrix is only affected by the angular offset [78]. When choosing the distance between the receiving antennas as half a wavelength, an unambiguous field of view of  $\pm 90^\circ$  is possible in principle. However, the spacing of the subarray elements still has to fulfil the generalised sampling criterion valid for switched arrays (cf. equation (4.9)).

The physical arrangement together with the equivalent aperture is shown in Fig. 4.24. As this method would have required a different antenna setup, only

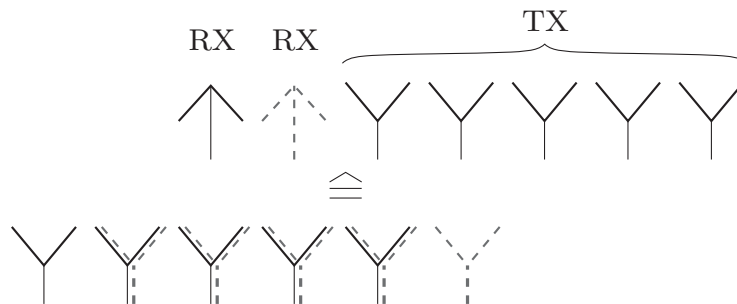


**Fig. 4.24:** Equivalent aperture of 5 TX and 2 RX antennas, suitable to generate Doppler tolerant subarrays for ESPRIT processing.

simulated results are shown in Fig. 4.25. It can be seen, that the targets appear at the correct angular positions even if they are moving. According to (4.9) and the sensor settings in the fast mode, the maximum unambiguous velocity is  $5.8 \frac{m}{s}$  for a boresight target and  $5.2 \frac{m}{s}$  for a  $\pm 30^\circ$  field of view. A range error is apparent for moving targets as the frequency of the received signal is affected

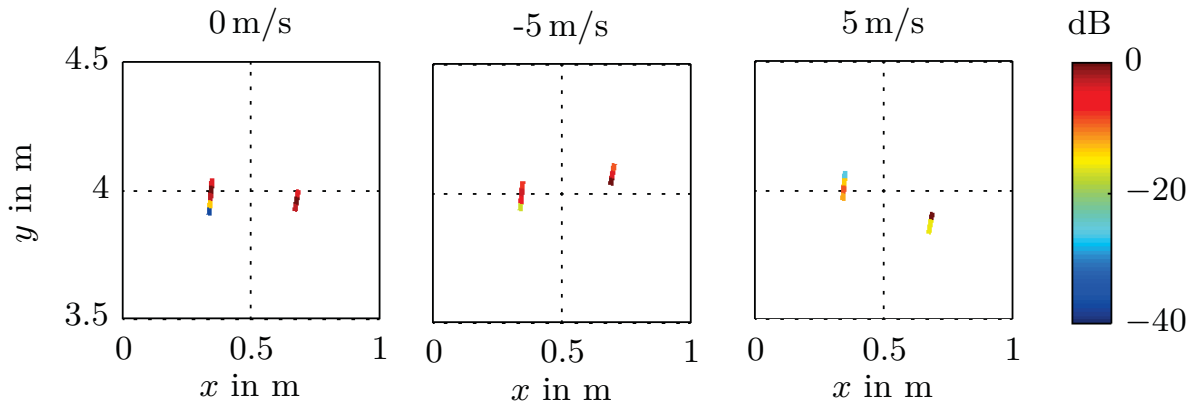


**Fig. 4.25:** Simulation results for the application of the ESPRIT based subarray approach for Doppler mitigation in switched antenna arrays; the right target is moving at different velocities.

by the Doppler effect. However, the range/Doppler ambiguity can be easily resolved by means of a triangular modulation scheme (cf. Section 2.5).

## 5 Applications Investigated with the Developed Sensors

The development and availability of components and integrated circuits (MMICs) in the millimetre-wave range is mainly driven by automotive radar applications [79, 80]. However, besides the automotive sensors, also industrial and security applications can take benefit from these components. The applications range from Doppler sensors [81] over one-dimensional level gauging to two-dimensional safety systems [3]. This chapter presents examples of two-dimensional surveillance radars based on mechanically steered sensors and SAR. Additionally, a quasi three-dimensional radar imaging using SAR and digital beamforming is described.

### 5.1 Runway Surveillance

Since a few years, Foreign Object Debris (FOD) detection on airport runways has gained increasing interest. A basic motivation is the fatal accident of a Concorde aircraft in 2000 due to a metal part dropped by an aircraft on the runway some time before. Currently there are systems based on optical sensors like CCD cameras [82] or Lidar [83] and those based on mm-wave radars [84], but also systems combining those techniques are available on the market [7, 85].

The system configuration investigated here is depicted in Fig. 5.1 [86, 87]. It consists of a number of low power and low cost mm-wave sensors as those developed within this work, that are located on both sides of the runway. The interlaced arrangement of opposing sensors provides a full coverage of the runway with a minimum number of installations.

The scalability of this approach and the use of off-the-shelf components can make such a system affordable even for smaller airports.

#### 5.1.1 Antenna Concept

Commercially available components for mm-wave frequencies typically provide an output power in the order of 0 dBm to 10 dBm. To achieve the detection performance needed for runway surveillance the sensor's  $G/T_{\text{sys}}$  has to be optimised. With respect to the receiver sensitivity many efforts have been made

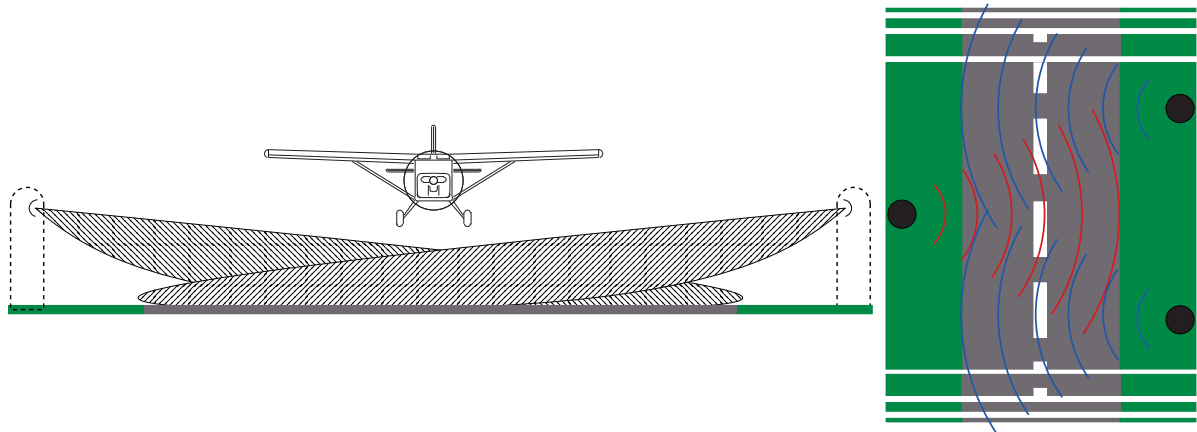


**Fig. 5.1:** Runway surveillance system consisting of low power mm-wave sensors located at both sides of the runway.

as described in Chapter 3. Additionally, increasing the gain of the antenna and designing an appropriate pattern helps improving the performance further on.

In monostatic radar configurations the received power is

$$P_{RX} = \frac{P_{TX} G^2(\varphi) \lambda^2 \sigma}{(4\pi)^3 R^4}, \quad (5.1)$$

where  $G(\varphi)$  is the gain of the antenna in the direction of the target and  $\sigma$  the target's radar cross section (RCS).

For the given scenario, one can exploit the fact that all objects are known to be located on the runway surface. The geometry leads to a well-defined relationship between the off-boresight angle  $\varphi$  and the slant range  $R$  or the ground range  $R_g$  (cf. Fig. 5.2).

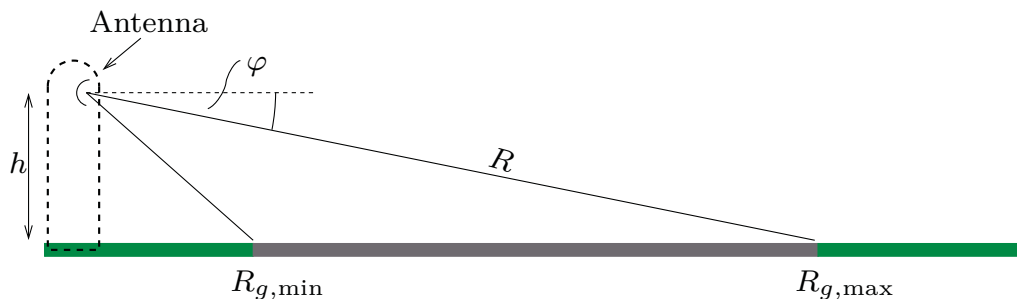


**Fig. 5.2:** Definition of the off-boresight angle  $\varphi$  and the target distance.

Substituting  $R = h \operatorname{cosec}(\varphi)$  in (5.1) gives

$$P_{RX} = \frac{P_{TX} \lambda^2 \sigma}{(4\pi)^3 h^4} \frac{G^2(\varphi)}{\operatorname{cosec}^4(\varphi)}. \quad (5.2)$$

Inspecting (5.2) shows that using an antenna pattern

$$G(\varphi) \propto \operatorname{cosec}^2(\varphi) \quad (5.3)$$

results in a received power, that no longer depends on the target's ground distance. By compensating for the known range dependent power variation of the received signal, the complete receiver dynamic is available to cover a wide range of possible RCS's.

Folded reflectarray antennas [88, 89] with  $\operatorname{cosec}^2$ -patterns [90, 91] and pencil beam pattern have been used for experimental studies [86, 87]. A comparison between a  $\operatorname{cosec}^2$ -antenna with a diameter of 200 mm and a pencil beam antenna with 130 mm diameter shall be shown hereinafter.

The small height over ground of the antenna  $h = 0.5$  m leads to a very steep slope of the  $\operatorname{cosec}^2$ -pattern. As a consequence this pattern can only be approximated in physical implementations. Figure 5.3 shows the achieved pattern of the  $\operatorname{cosec}^2$ -antenna in comparison with the desired ideal mask and the pencil beam antenna. In addition, the normalised gain of the antennas is depicted as a function of the ground range. It is thereby assumed that the maximum gain of the antennas is pointing to the maximum ground distance  $R_{g,\max}$ . Especially for low off-boresight angles  $\varphi < 3^\circ$  the  $\operatorname{cosec}^2$ -approximation is poor due to the limited aperture size of 200 mm. As a result the normalised gain over the ground range deviates up to 10 dB from the ideal case. The shape of the pencil beam pattern and also the achieved gain over ground range is quite similar for farther ranges. For the closer distances  $R_g < 10$  m the  $\operatorname{cosec}^2$ -antenna outperforms the pencil beam antenna.

A better approximation of the  $\operatorname{cosec}^2$  pattern is obtained by slightly tilting the antennas as shown in Fig. 5.4. As a drawback, the available gain is reduced within the desired range. However, tilting the antennas can be used to trade off dynamic range against sensitivity.

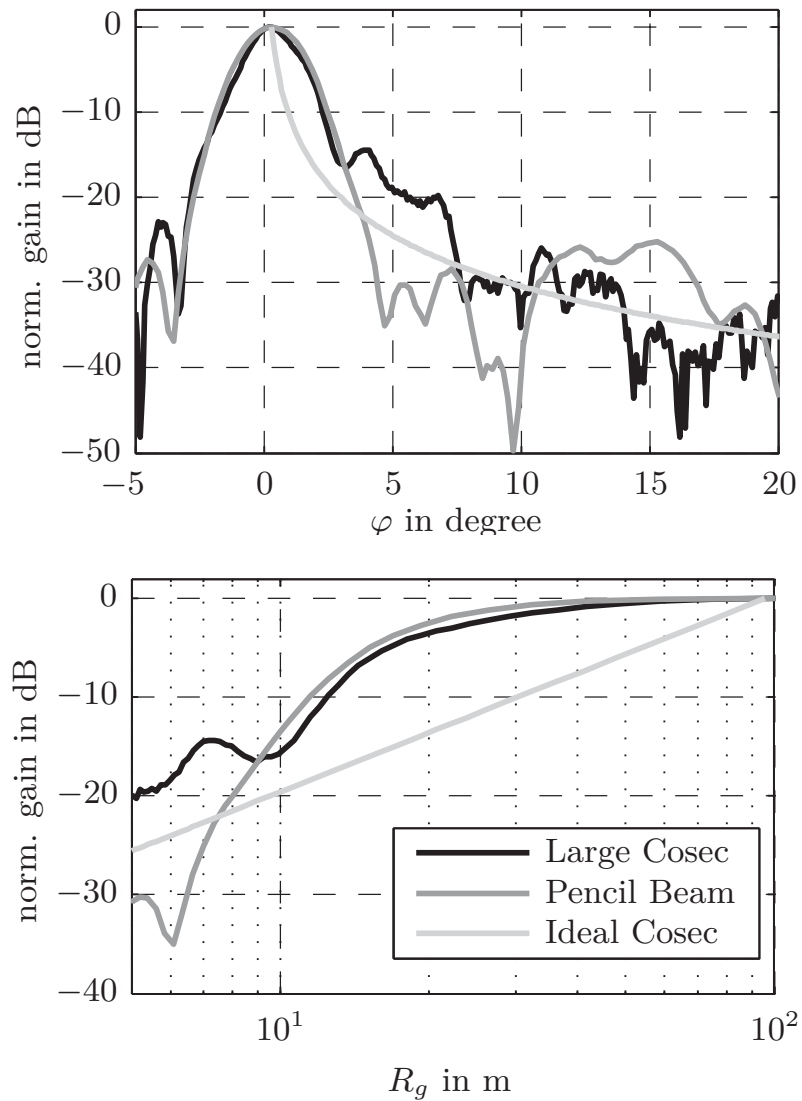


**Fig. 5.3:** Normalised antenna gain as a function of the off-boresight angle  $\varphi$  (top) and the ground range (bottom) as defined in Fig. 5.2.

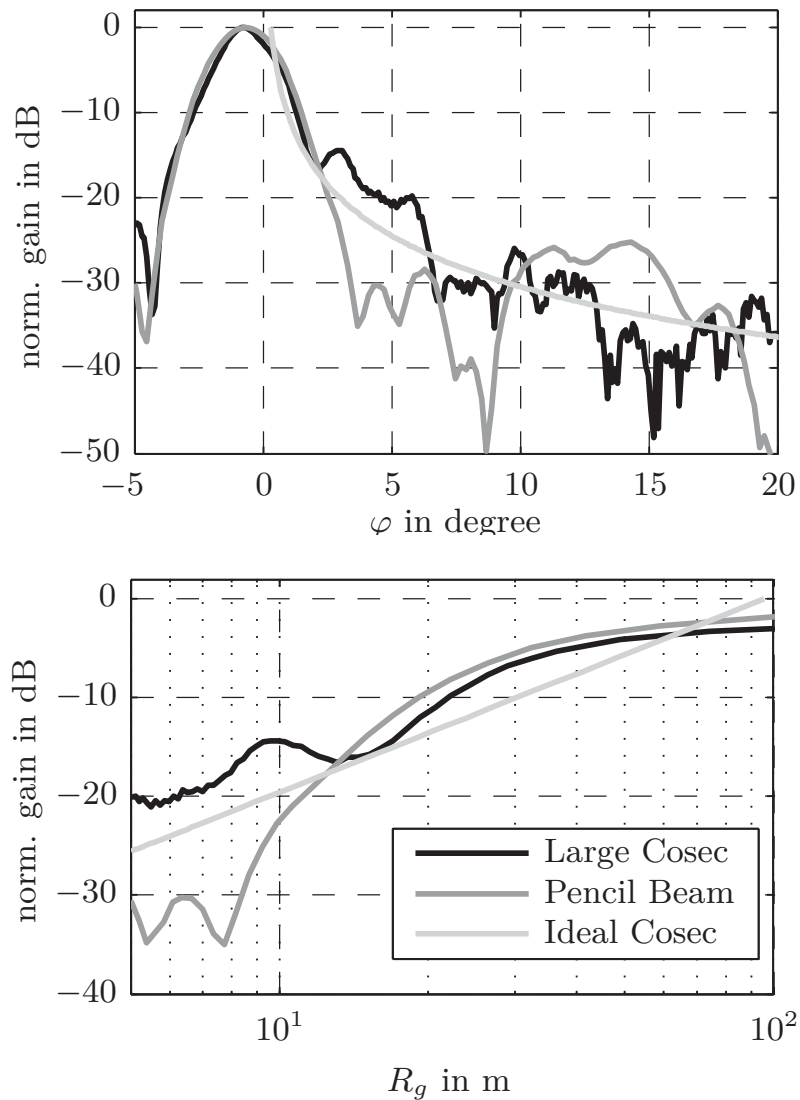


**Fig. 5.4:** Normalised antenna gain as a function of the off-boresight angle  $\varphi$  (top) and the ground range (bottom) as defined in Fig. 5.2; antennas are tilted to better match the desired cosec<sup>2</sup>-behaviour (cf. Fig. 5.3).

### 5.1.2 Signal Processing

The two-dimensional back scattering map of the runway surface is obtained by mechanically scanning the sensor. Detecting FOD by observing this image is not satisfactory for the practical application. On the one hand, the large dynamic range of the signals cannot be mapped to a colour or brightness coded image with sufficient contrast. On the other hand, it is desired that the operator of the system is alerted automatically in case of a detected object.

The solution is to use a constant false alarm rate detector (CFAR). The idea behind this detector is, that the clutter and noise level is estimated for each cell of interest. If the ratio between the signal detected within this cell and the estimated background level exceeds a certain threshold, an alert is triggered.

CFAR detectors described in literature [92, 93] typically operate on one-dimensional range profiles, but the concept is also applicable for two-dimensional data. Figure 5.5 shows the principle of the two dimensional CFAR detector. The background level is estimated using a two-dimensional moving average filter, where the respective cell of interest is located in the centre of the averaging window. It is excluded from the calculation to avoid an artificial rise of the estimate, if there is a target present in this cell. Even a point target may be spread over several angular and range cells. This is due to the azimuthal pattern of the antenna and the point spread function of the range processor. Hence, it is advantageous to additionally use some guard cells surrounding the cell of interest, that are also excluded from the background estimation.

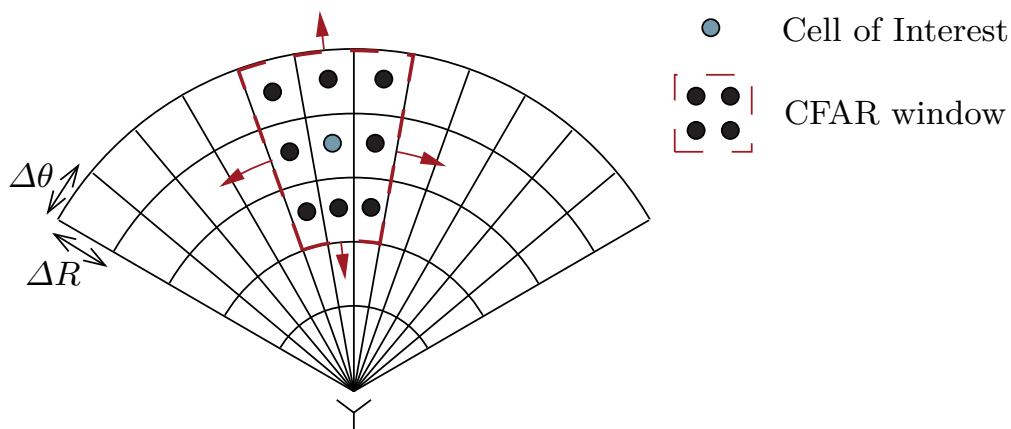


**Fig. 5.5:** Two-dimensional estimation of the clutter level using a moving average filter.

### 5.1.3 Experimental Results

In a first step the sensitivity of the sensor was investigated in a one-dimensional setup using a 25 mm aluminium sphere as a reference target whose RCS does not depend on the azimuthal angle of incidence.

In order to reduce the clutter power contained within one range resolution cell, a wide sweep bandwidth of 7 GHz was used in all experiments. The duration of the FM-CW pulse was 4.8 ms. Figure 5.6 shows the measurement results with the sphere being located at a distance of 50 m on a rough asphalt surface. Thereby, the signal and variance levels are estimated out of 64 snapshots. Since the variance gives the noise level relevant for the processing of a single FM-CW pulse, the viewgraph shows that the signal to interferer ratio (clutter or noise) can be improved by 10 dB when coherently integrating 64 measurements. As the theoretical processing gain is  $10 \log_{10}(64) \text{ dB} = 18 \text{ dB}$  and no improvement is achieved by increasing the number of pulses, this implies that the detection performance is limited by the clutter when having integrated at least 10 subsequent measurements. On the other hand if only a single pulse is considered, the limit is given by the system noise.

A second aspect can be seen from the results. Even though the RCS of the sphere is very small, there is a considerable excursion visible within the clutter background. This is due to the specular reflection properties of asphalt and concrete surfaces also reported in literature [94].

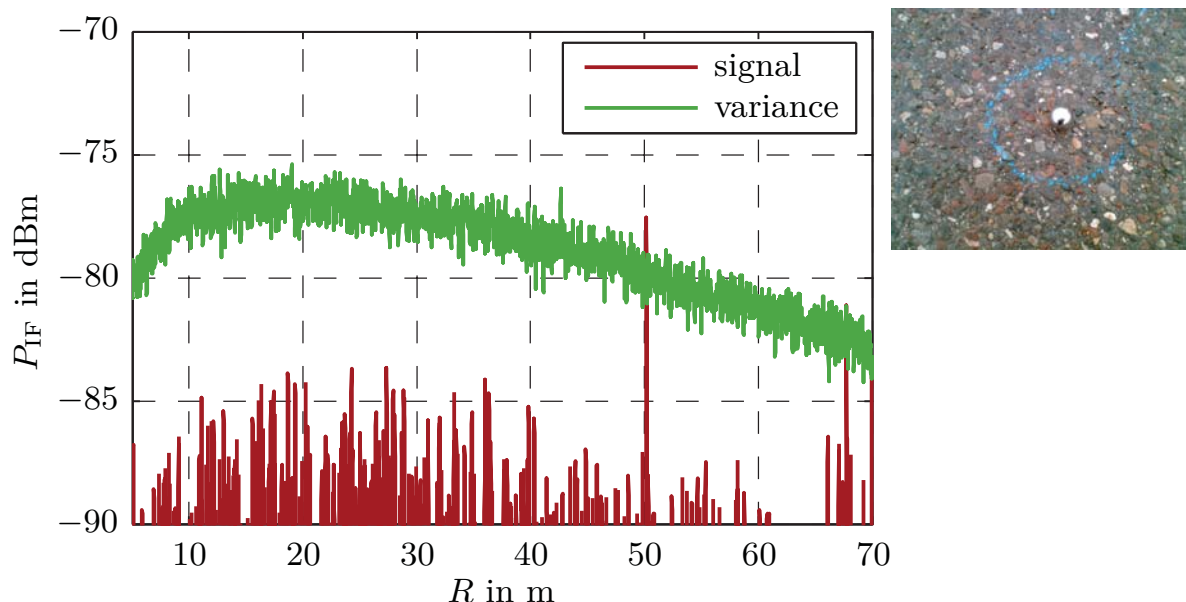


**Fig. 5.6:** Radar response (left) of a 25 mm aluminium sphere (right) located at 50 m distance on a rough asphalt surface.

The overall clutter power received from a single range cell is related to the range resolution, the azimuthal beamwidth of the antenna and the distance at which the respective range cell is located (cf. Fig. 5.5):

$$P_{\text{clutter}} \propto R \Delta R \Delta \theta \quad (5.4)$$

Since the detection performance is given by the signal-to-clutter ratio, an improvement is achieved by increasing the bandwidth or decreasing the antenna beamwidth.

After these preliminary investigations measurements were conducted at Aix les Milles Airport in the south of France using the two antennas described above [87]. Thereby, FOD has been distributed randomly on the runway surface. Most of the objects are “real” FOD that has been collected at Charles de Gaulle airport in Paris.

Figure 5.7 shows a photograph of the scenario. FOD that has been automatically detected by the CFAR detector is marked by red crosses. Multiple detections are due to an angular step width being smaller than the azimuthal beamwidth. Table 5.1 summarises the detection performance using the pencil beam antenna and the cosec<sup>2</sup>-antenna.

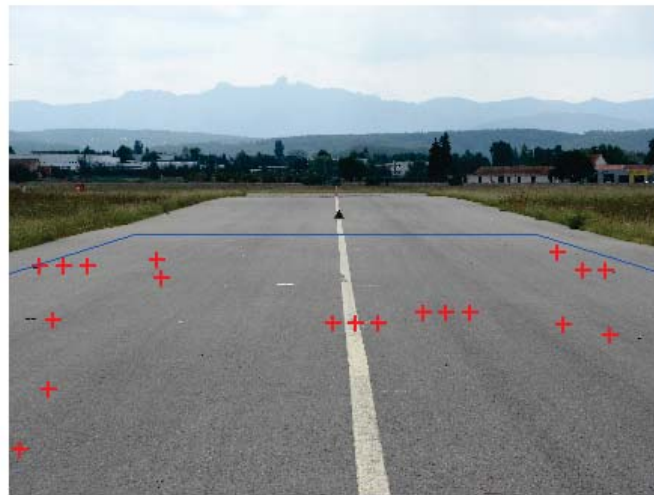


**Fig. 5.7:** Photograph of the runway with randomly distributed objects; automatically detected FOD is marked by red crosses, the blue line indicates the area considered for processing.

No.	Object	$R_g$ in m	Antenna:	
			A	B
1	Acrylic plate	40	No	No
2	Sphere, 40 mm	55	Yes	Yes
3	Cubic piece of wood	not used	–	–
4	Bent metal strip	not used	–	–
5	Big stone	65	No	No
6	Middle sized stone	32	Yes	Yes
7	Small stone	29	No	Yes
8	Nut, M10	30	Yes	Yes
9	Screw, M10 × 60 mm	50	No	No
10	Sphere, 25 mm	30	Yes	Yes
11	Piece of plane (CDG)	47	Yes	Yes
12	Plane tank cap (CDG)	50	Yes	Yes
13	Piece of plane break 1 (CDG)	32	Yes	No
14	Piece of plane break 2 (CDG)	74	No	No
15	Piece of runway lamp 1 (CDG)	60	No	No
16	Piece of runway lamp 2 (CDG)	31	No	No
17	Small stone (CDG)	29	Yes	Yes

**Tab. 5.1:** Description of various FOD and detection performance achieved with the pencil beam antenna (A) and the cosec<sup>2</sup>-antenna (B).

As expected the behaviour is quite similar for both antennas. Due to the smaller azimuthal beamwidth the cosec<sup>2</sup> antenna performs slightly better. Even though a coherent integration time of about 50 ms–100 ms has to be used to reach the clutter limit, the scanning of a  $\pm 90^\circ$  field of view can be accomplished within less than half a minute, which is fast enough for the intended application.

The results show, that even very small targets can be detected within the asphalt clutter background as long as they have a certain elevation above the flat surface and minimum monostatic RCS. Both conditions make the detection of flat objects very hard and strongly dependent on their orientation. In future,



## 5 Applications Investigated with the Developed Sensors

---

a bistatic processing of the radar pulses (e.g. of sensors facing each other along the runway) may be used to handle those objects.

Additionally, the static clutter background may be stored and subtracted from subsequent measurements to further improve the detection performance (see also the considerations about the sensor calibration in Section 2.4). Apart from the sensor coherency this would require a very stable condition of the environment. Especially at farther ranges air turbulences may influence the accuracy. Hence, an ad-hoc approach is preferable.

## 5.2 MM-Wave Synthetic Aperture Radar

Synthetic Aperture Radars (SAR) exploit the linear motion of a radar sensor in order to obtain a very high range independent azimuthal or lateral resolution. As the SAR processing in this work is based on well-known algorithms, a detailed description is omitted and may be found in textbooks such as [95] or [96].

To evaluate SAR as another interesting candidate for surveillance applications, a demonstrator was developed [97], that can carry various sensors, e.g. those described in Chapter 3 and Chapter 4 or the 24 GHz imaging sensor presented in [62]. Using these monostatic and digital beam forming (DBF) sensors, the basic SAR modes such as stripmap SAR and Spotlight SAR can be implemented. Additionally, azimuth SAR processing has been combined with DBF in elevation. This configuration allows the three-dimensional imaging of scenarios.

### 5.2.1 SAR Demonstrator Setup

The whole system shown in Fig. 5.8 consists of a linear actuator which accomplishes the linear motion of the radar sensors. A laptop computer controls both the actuator and the sensors.

Different configurations with the monostatic and the DBF sensor developed in this work are investigated. Additionally, a 24 GHz DBF sensor [8] has been integrated using the same principles as described in Chapter 4 except for the number of antenna elements (25 TX and 2 RX). Originally, this sensor was

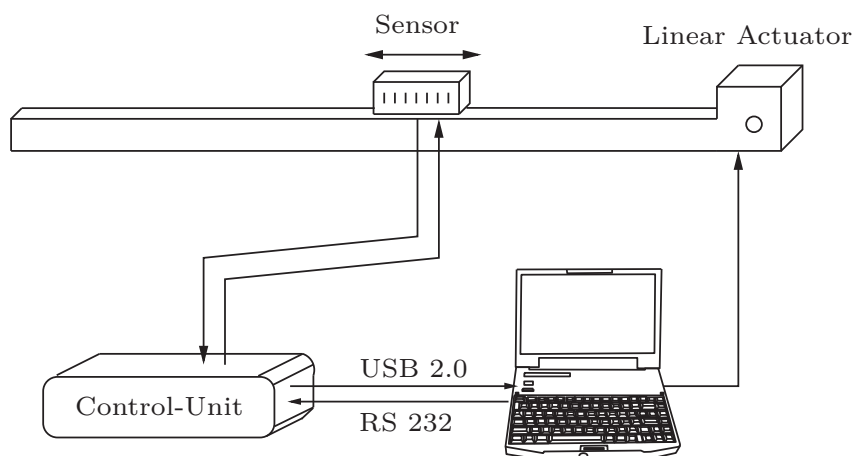


Fig. 5.8: SAR demonstrator setup.

intended for automotive applications, but other applications like industrial safety [3] are proposed as well.

The key parameters of all sensors are summarised in Table 5.2.

### 5.2.2 Modes of Operation and Signal Processing

The first step in SAR signal processing is extracting the range information. The following steps depend on the type of sensor and the SAR mode. For single channel sensors just one range profile per azimuth sampling point is available. Due to the architecture, stripmap SAR is the only possible mode.

For the imaging sensors, 64 or 50 range profiles have to be processed to extract the desired information. Beamforming can be employed either to steer a beam to the scene of interest for spotlight operation or to deliver a complete elevation scan for the 3D mode.

Due to the use of a linear actuator and its accuracy, there was no need taking into account any errors in the trajectory. Further on, it is possible to do stop-and-go measurements. Hence, the data acquisition time is not a limiting factor for the azimuth sampling rate.

For all operating modes azimuth focusing is performed in the range Doppler domain because of the lower computational complexity and the ability of range cell migration correction [98]. Although range cell migration correction is not needed for the narrow beam antenna used in this configuration, the correction has been implemented to be able to use antennas with different aperture sizes.

### 5.2.3 Performance Evaluation in Stripmap Mode at 77 GHz

The stripmap mode was tested in conjunction with the monostatic 77 GHz radar. A picture of the overall setup is shown in Fig. 5.9. In Fig. 5.10 the result of a measurement is depicted, where two small reflectors separated by 7 cm have been placed at a distance of 30 m. The theoretical limit of the azimuthal resolution is about 5 cm given by the azimuthal antenna size. The measurement shows that

	<b>Monostatic</b>	<b>DBF 77 GHz</b>	<b>DBF 24 GHz</b>
Centre frequency	77 GHz	77 GHz	24.5 GHz
Bandwidth	typ. 6 GHz	typ. 6 GHz	typ. 800 MHz
Aperture size	dia. 130 mm	80 mm × 34 mm	170 mm × 70 mm
Beamwidth $\Delta\theta_{3dB}$	2.5°	2.5° (DBF)	3° (DBF)
Beamwidth $\Delta\varphi_{3dB}$	2.5°	6°	12°

**Tab. 5.2:** Key parameters of the sensors used with the SAR demonstrator.



**Fig. 5.9:** Photograph of the overall setup for evaluating stripmap SAR at 77 GHz.

the two reflectors are clearly distinguished after stripmap processing. The range resolution is also 5 cm leading to a square resolution cell or SAR pixel size.

A second scenario more related to FOD detection is shown in Fig. 5.11. Three aluminium spheres are situated at a distance of around 27 m to 28 m. In order

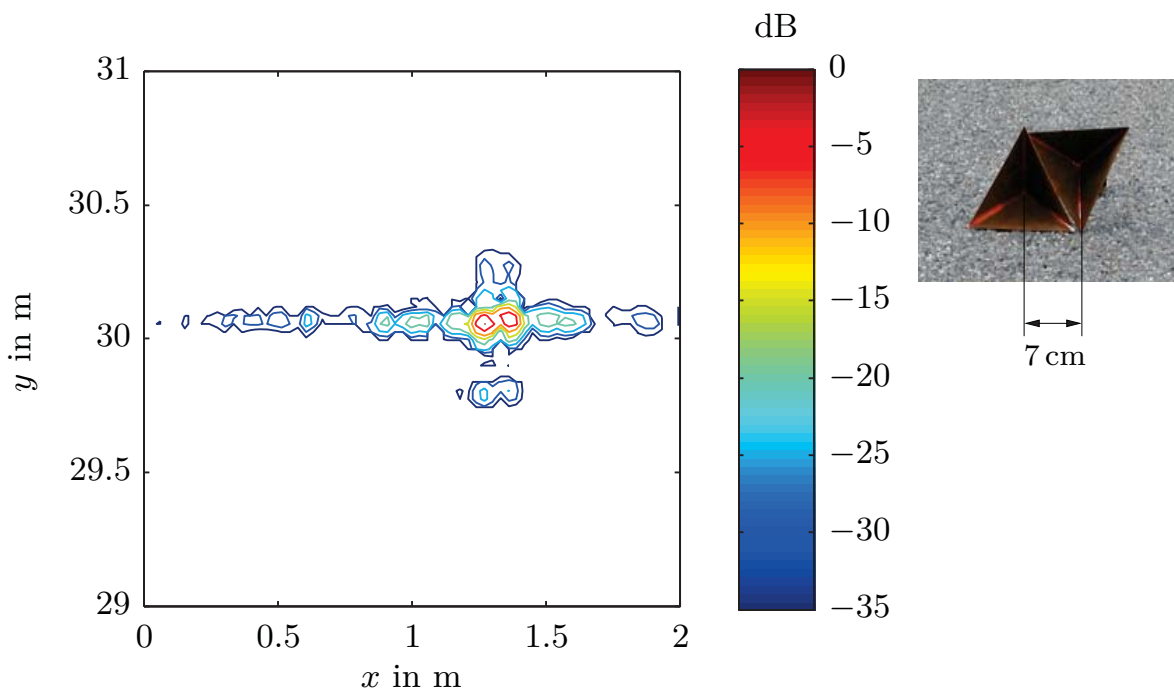


**Fig. 5.10:** Measurement results obtained with the 77 GHz sensor in stripmap mode (left) using two closely spaced corner reflectors (right) as radar target.

to better compensate for the signal dynamic caused by free space propagation, a cosec<sup>2</sup> folded reflectarray antenna with 130 mm diameter was used, that has been designed for that purpose [99]. The parameters of this antenna in terms of gain and azimuthal beamwidth are very similar compared to the pencil beam antenna used in the first test. The raw data that are obtained by the stripmap measurement are processed using a two-dimensional CFAR processing as described in Section 5.1.2. That means the viewgraph in Fig. 5.11 depicts the ratio of the signal to the estimated clutter and noise level. The signal-to-clutter-and-noise ratio for the spheres is in the order of 10 dB to 15 dB. Hence, a reliable detection is possible.

Of course not only discrete scatterers but also distributed objects can be detected using SAR. Figure 5.12 shows an indoor environment scanned with the SAR demonstrator in stripmap mode. Here the raw output data of the range Doppler algorithm are used to generate a two dimensional image of the closer surrounding without CFAR thresholding and detection. The tips of the double wing door can clearly be identified as well as the profile of the adjacent walls. Again the SAR image has a square pixel size of about 5 cm × 5 cm, which enables the use of such a system even in complex environments.

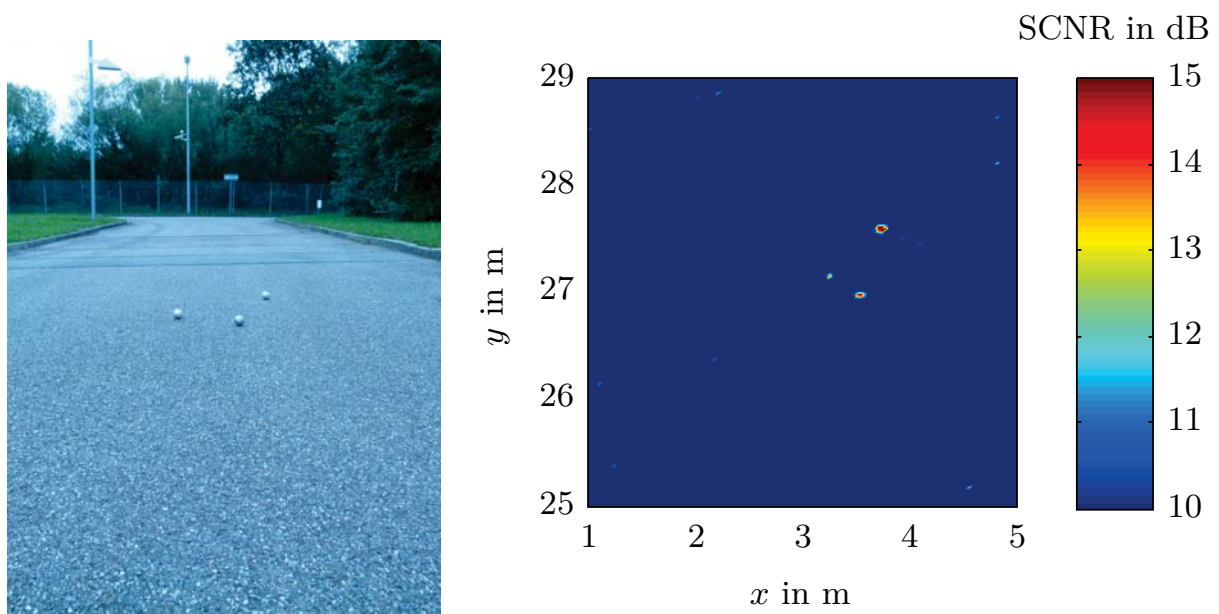


**Fig. 5.11:** Photograph of three objects arranged at a distance between 27 m and 28 m (left); result of the corresponding SAR measurement in stripmap mode after CFAR processing (right).

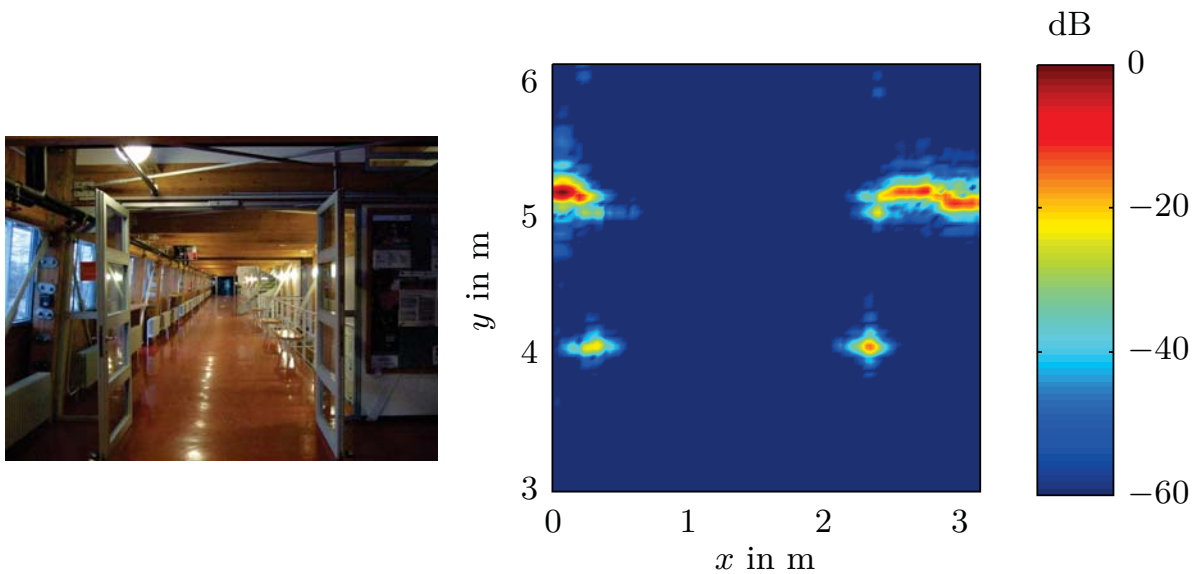


**Fig. 5.12:** Photograph of an open double wing door (left); result of the corresponding SAR measurement in stripmap mode (right); the right viewgraph shows the normalised amplitude after the SAR processing.

The following discussion will only concern the two DBF sensors. Of course they can be used for stripmap operation as well, but due to the switched array antenna, additional modes are possible.

#### 5.2.4 Spotlight Operation at 24 GHz

In the spotlight mode the beam steering capability of the 24 GHz imaging sensor is used to point the synthesised beam to the centre of the scene of interest. Again azimuth compression and range cell migration correction are performed in the range Doppler domain. Figure 5.13 shows the measurement result of two small corner reflector separated by 7 cm at a distance of 6.5 m for stripmap and spotlight operation. In stripmap mode the length of the synthetic aperture is limited by the azimuthal beamwidth of  $3^\circ$ . At 24 GHz this corresponds to a lateral resolution of more than 10 cm, which is not enough to resolve the reflectors. When using spotlight operation the reflectors can be clearly resolved. Due to the limited sweep bandwidth of the 24 GHz radar the azimuthal resolution is much better than the range resolution. However both values match with the theoretically expected results.

The advantage of using DBF compared to e.g. a phased array is that the scene of interest can be chosen in the postprocessing rather than in advance. That

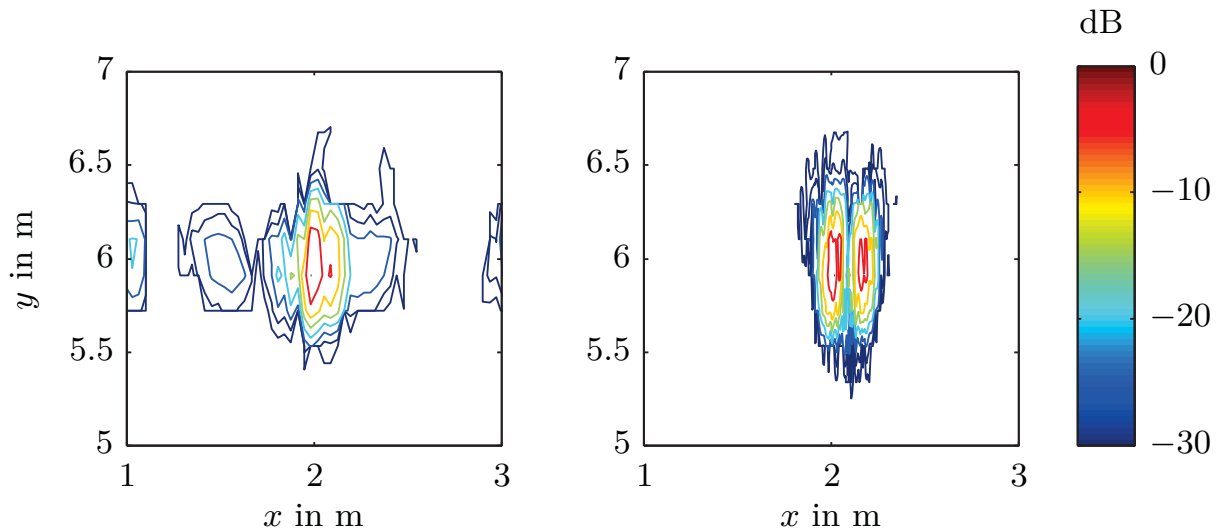


**Fig. 5.13:** Measurement results obtained with the 24 GHz sensor in stripmap (left) and spotlight mode (right); the viewgraphs show the normalised amplitude after the SAR processing.

means that after acquiring the data, any point can be mapped with the high resolution provided by spotlight SAR.

### 5.2.5 Three Dimensional Combined SAR and DBF Processing at 24 GHz and 77 GHz

A three dimensional image of the environment can be acquired by turning the imaging plane of the DBF radar perpendicular to the SAR trajectory. This enables the evaluation of the additional angular dimension in the elevation compared to the stripmap mode presented in Section 5.2.3. The respective resolution cell is depicted in Fig. 5.14. The dimensions  $\Delta R$ ,  $\Delta\theta$ , and  $\Delta x$  depend on the sweep bandwidth, the size of the DBF array in elevation and the azimuth beamwidth of the switched antenna elements.

#### Measurement of Discrete Scatterers Distributed in Space

A barrier on the university campus consisting of three metal posts served as a first scenario for the evaluation of the 3D-mode. The results obtained using the 24 GHz DBF sensor are shown in Fig. 5.15.

The position as well as the vertical extents of the posts can be obtained by the measurement. Of course there cannot be a photo-realistic image, because the radar return of these kind of posts contains the superposition of three major

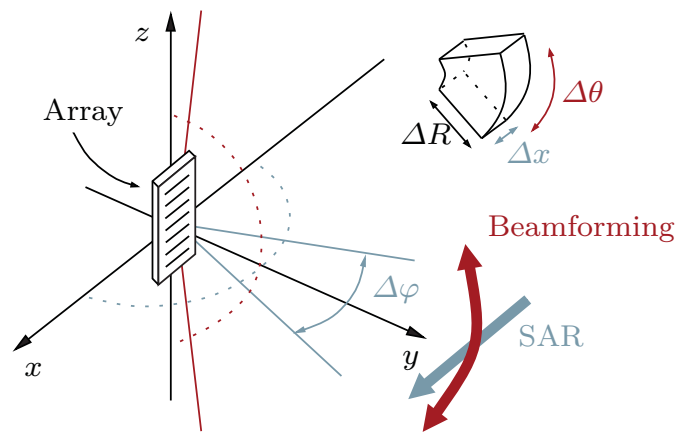


**Fig. 5.14:** Geometry and resolution cell of the 3D imaging mode.

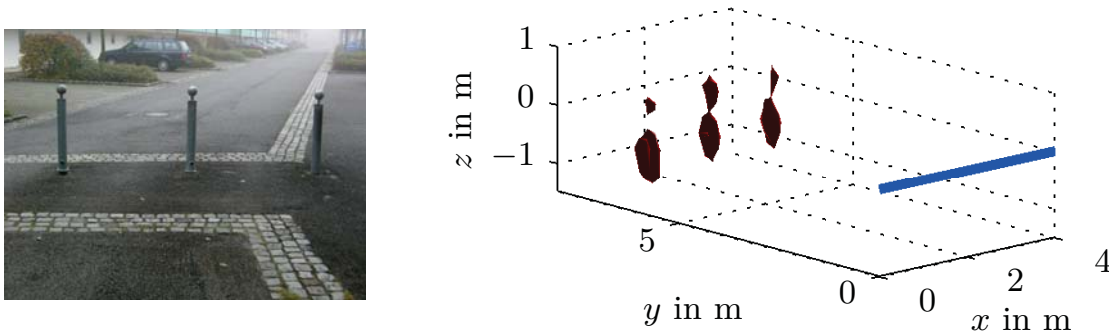


**Fig. 5.15:** Three metal posts (left) and respective 3D-SAR/DBF image (right); the blue line indicates the trajectory of the SAR sensor.

reflections: one caused by the sphere on top of the posts, one obtained for perpendicular incidence, and a twofold reflection between post and ground. However, such a measurement can help distinguishing objects lying on the ground and upright objects such as persons.

### High Resolution Terrain Measurements

Based on the three-dimensional imaging technique described above, terrain measurements have been performed using the 77 GHz sensor described in Chapter 4. The raw three-dimensional SAR data are available on a spatial grid as depicted in Fig. 5.16. To provide an adequate visual representation, they have to be processed further on. First of all, the three-dimensional reflectivity map has to be reduced to a reasonable number of significant scatterers. An intuitive approach

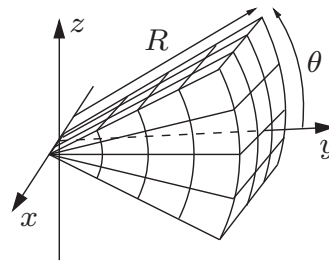


**Fig. 5.16:** Spatial grid for the representation of the raw data obtained by combined SAR and DBF processing.

is using thresholding. Of course, a static threshold with respect to the received power is not feasible, as the dynamic range of the data is very large and the absolute level depends on the distance. Even if there is a filter implemented in the FM-CW radar compensating for the range dependent decay of the received power, it cannot be designed to perfectly match all possible scenarios. The solution is generating a dynamic threshold by estimating the background noise or clutter as done for CFAR algorithms (cf. Section 5.1.2). Normalising the value within a three-dimensional resolution cell by such a dynamic threshold gives the SCNR (Signal-to-Clutter-and-Noise ratio) as a measure for the probability of a scatterer being situated within the cell under test. If no further a priori information of the environment is available, the data can be represented as a point cloud where the size and colour of the points are related to its SCNR. In many cases some additional knowledge of the environment is available. As an example, when mapping the ground surface with the sensor located in free space it can be assumed, that for each spatial direction the reflection with the largest SCNR occurs at the air-ground interface. After identifying these scattering centres, the ground surface can be interpolated.

This approach is applied to the measurement of a so-called “dolina” which is the geological term for a sinkhole generated by subsurface erosion [100]. In Fig. 5.17 the three-dimensional point cloud is combined with the estimated surface of the dolina. The SCNR obtained on this surface is colour-coded. To avoid reflections from isolated objects such as trees and bushes being incorporated in the calculation, the interpolation of the ground surface has been restricted to a certain area. The real shape and dimensions of the dolina match with the experimental results very well.

Some more information can be obtained, when looking at the top and side view of the point cloud consisting of the scatterers identified by the CFAR processing (Fig. 5.18). Here the main scatterers within the dolina, the trees

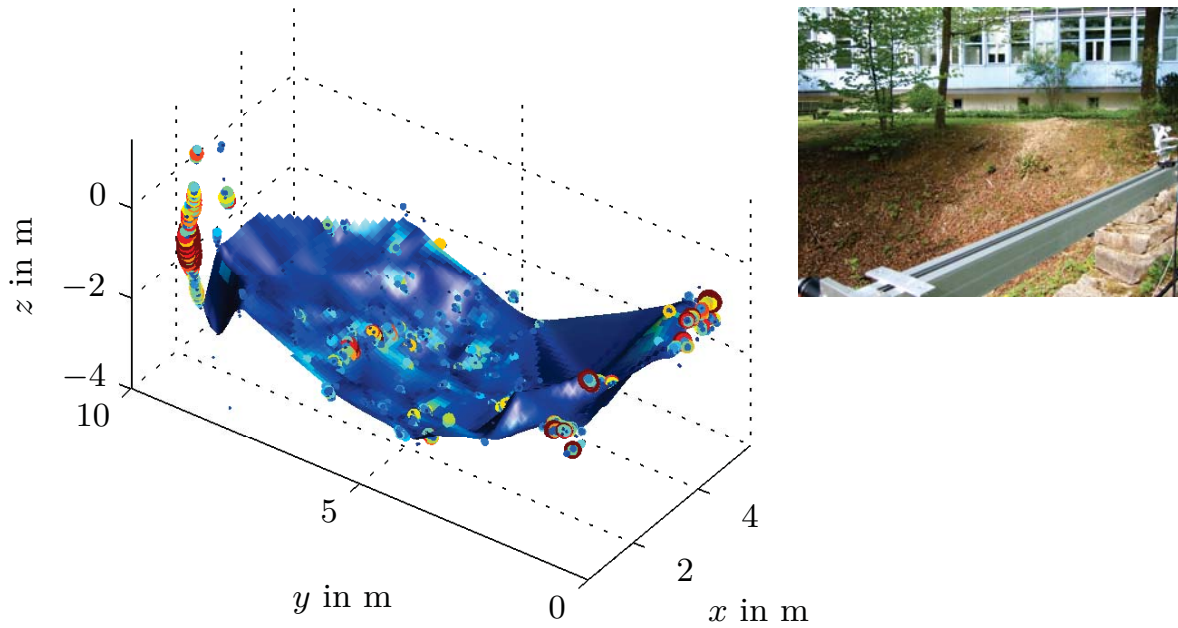


**Fig. 5.17:** Result of the three-dimensional SAR measurement of a dolina.

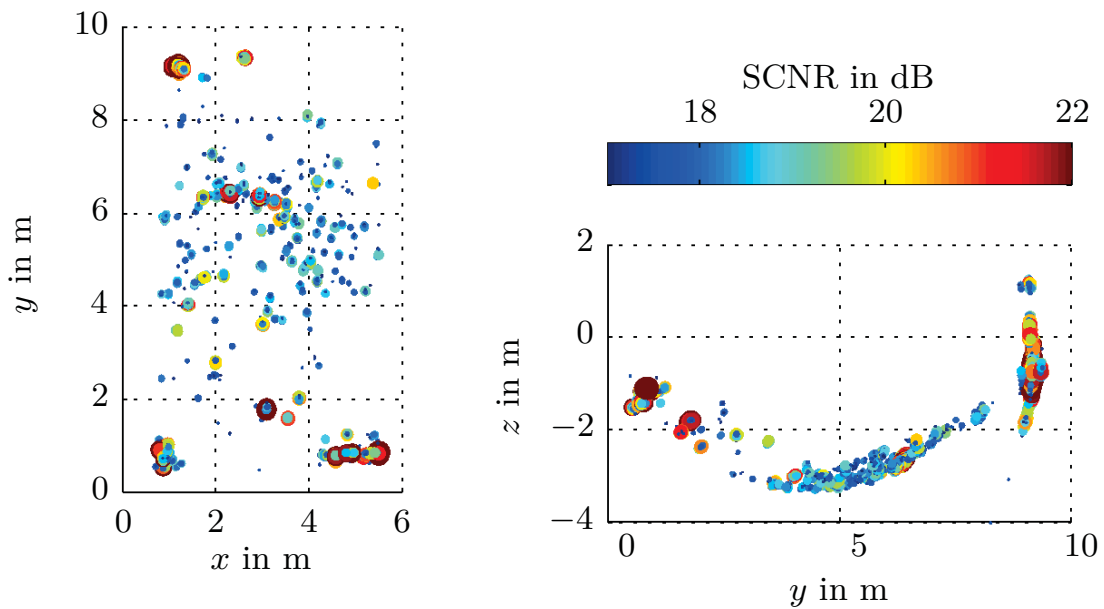


**Fig. 5.18:** Top view (left) and side view (right) of the point cloud assembled of CFAR detected scatterers

## 5 Applications Investigated with the Developed Sensors

in the background, and the opening of the little wall in the foreground can be identified.

The second scenario that has been acquired with the three-dimensional SAR is a stonewall situated on the university campus (cf. Fig. 5.19).

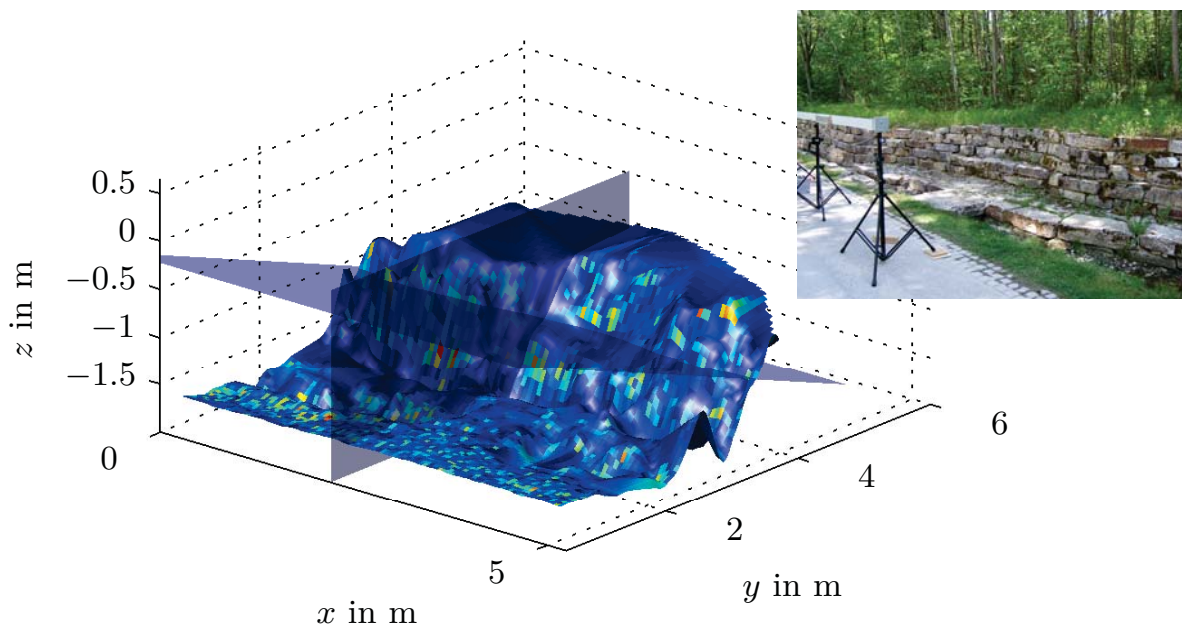


**Fig. 5.19:** Result of the three-dimensional SAR measurement of a stonewall.

The profile of the wall is mapped properly. The features in the foreground such as the trench, and the stone plate bridging it, are also observable in the viewgraph. To get an idea of the resolution in azimuth and range, the CFAR detected scatterers on the wall surface are depicted for an angular section and an azimuthal slice as depicted in Fig. 5.19; the results are shown in Fig. 5.20.

Again the results are normalised to present the local SCNR. As the width of a single azimuthal slice is less than 1 cm for the given antenna size, a number of 21 slices has been combined in order to obtain a quasi-continuous profile.

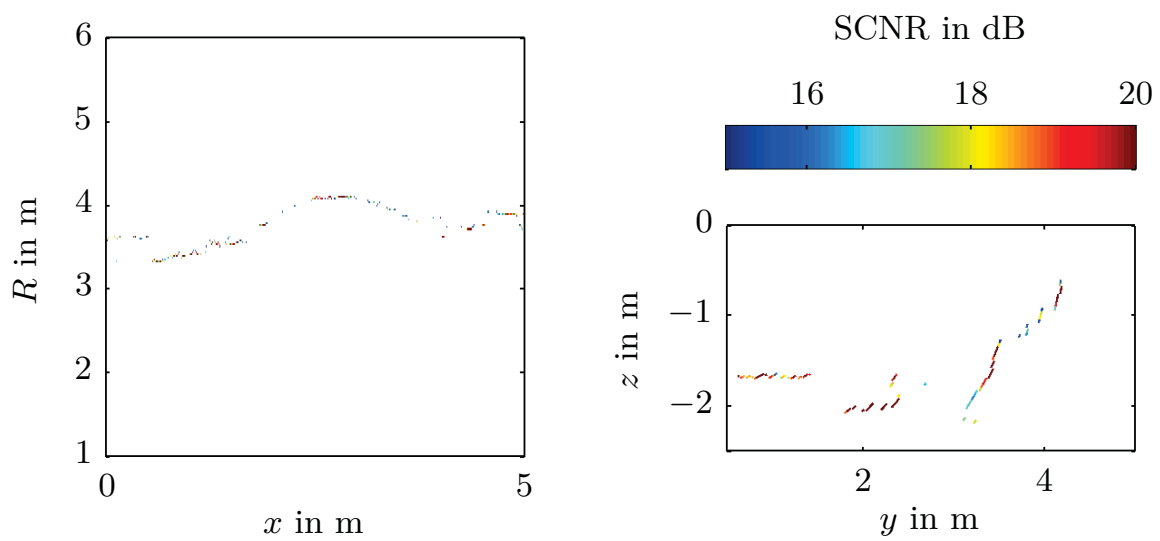


**Fig. 5.20:** Azimuthal (left) and elevation slice (right) of the three-dimensional SAR measurement in Fig. 5.19.

### 5.2.6 Further Applications

In addition to environmental monitoring, also some other applications are imaginable, e.g. the investigation of the backscatter properties of cars [101, 102]. And even if switched DBF sensors are used, the setup is not limited a to stop-and-go operation. As the SAR motion is perpendicular to the pointing direction of the antenna, the radial Doppler is typically small and can be accomplished using techniques as described in Section 4.5. Additionally, the inverse SAR (ISAR [12]) could be applied to map moving contours such as the load on trains or conveyor belts. And also applications requiring mapping capabilities at a farther distance can be addressed. Provided a sufficient length of the synthetic aperture, only the vertical resolution degrades with increasing range. Hence, an arrangement as shown here should be feasible at much larger scales. Possible applications are the monitoring of mining areas, buildings, or bridges. Of course, it must be noticed that the range is not only limited by the angular resolution, but also by the available transmit power, which is quite small using today's commercial components at mm-wave frequencies.

## 6 Summary and Conclusion

This thesis deals with the design, implementation, and application of wideband mm-wave FM-CW sensors at 79 GHz. Apart from one-dimensional monostatic and bistatic sensors, also a switched antenna array is presented to investigate digital beamforming techniques.

All theoretical considerations are based on a comprehensive wideband mathematical description of the FM-CW principle. On the one hand, this enables the development of techniques mitigating the effects of dispersion, that are inherent to wideband sensors. On the other hand the approach is applied to digital beamforming FM-CW sensors in terms of a true time delay. Both calibration and true time delay have been implemented in the digital intermediate frequency domain without the need of a wider bandwidth or higher sampling rate as compared to conventional processing techniques used with FM-CW sensors.

The modelling of the sensors is done on a system level using an instantaneous phase-based technique. With this approach many undesired effects such as clock and VCO phase noise, spurious lines of direct digital synthesisers, or the transient response of the synthesiser and the IF processing are covered. It is explained how to describe the sensor behaviour with a good accuracy even for less usual configurations such as the heterodyne operation. Further on, the model helps understanding the effects of perturbations and how to mitigate them, e.g. using a heterodyne or differential receiver architecture.

The hardware design of the frontend and the switched antenna array extension was done under the premise of a wide bandwidth, low cost fabrication, reliable integration, and reproducibility. This goal was met by restricting the actual mm-wave circuit to a single layer metal backed PCB while keeping the interface to the lower frequency part as simple as possible. This approach requires the development of adapted and newly developed structures such as microstrip-to-waveguide transitions. Despite this cost effective approach the sensor performance is shown to be limited by the MMICs and the signal generation in the baseband rather than the mm-wave circuit itself.

The antenna configuration used for the DBF extension is known to suffer from Doppler sensitivity due to the switched or sequential operation, and high side-lobes caused by the gapped equivalent aperture given by the physical antenna positions. Both aspects have been successfully addressed by means of digital signal processing. Apart from that, the most common conventional and adap-

tive beamforming techniques have been demonstrated with the developed sensor hardware.

Among the applications under consideration there is the detection of foreign object debris (FOD) on airport runways and several arrangements based on the synthetic aperture radar (SAR) principle. The latter one is not only restricted to two-dimensional SAR modes like stripmap and spotlight. Using DBF in the dimension perpendicular to the SAR motion a three-dimensional mapping of the environment was performed. With respect to the FOD detection a distributed sensor system is outlined, the detection capability of which is limited by the surface clutter in which the objects are embedded. Thereby, very small FOD down to a diameter of 25 mm has been detected up to a distance of 50 m.

During the progress of this work new technologies such as SiGe MMICs and MEMS have become more and more available. Based on the described sensor architectures those technologies will help to improve the performance e.g. by using MEMS switches with low insertion losses or by monolithically integrating several functions or sensor channels. Even though the processing power available at low cost will enable DBF sensors with a high number of parallel channels, the switched approach will still have its justification in case of strict requirements with respect to cost or power.

## A Appendix

### A.1 Noise Modelling Using Rice's Second Model

In [103] Rice's second model is proposed for the analysis and generation of coloured noise. This model represents the noise signal as a series of sinusoids

$$n(t) = \sum_{n=1}^N a_n \cos(\omega_n + \phi_n). \quad (\text{A.1})$$

The coefficients  $a_n$  are deterministic and derived from the desired power spectral density of the noise. To account for the stochastic nature of the signal the phase of the sinusoids is random and uniformly distributed. This method is very useful in order to generate coloured noise e.g. based on a measured power spectral density.

### A.2 Single Sideband Phase Noise Spectrum

Phase noise can be described analytically as the modulation of the instantaneous phase of a sinusoidal signal:

$$s(t) = A \cos(\omega_0 t + \phi_n(t)) \quad (\text{A.2})$$

For this exact formulation, no closed solution for the signal spectrum can be calculated. However, for small amplitudes of  $\phi_n(t)$  the following approximation can be applied using the truncated power series representation of the exponential function [104]

$$\begin{aligned} s(t) &= A \operatorname{Re} \left\{ e^{j\omega_0 t} \cdot e^{j\phi_n(t)} \right\} \\ &= A \operatorname{Re} \left\{ e^{j\omega_0 t \cdot (1 + j\phi_n(t))} \right\} \\ &= A \cos(\omega_0 t) - A \cdot \phi_n(t) \cdot \sin(\omega_0 t). \end{aligned} \quad (\text{A.3})$$

Representing the noise using Rice's second model gives

$$\begin{aligned}
 s(t) &= A \cos(\omega_0 t) + A \sin(\omega_0 t) \sum_{m=1}^m a_m \cos(\Delta\omega_m t + \phi_m) \\
 &= A \cos(\omega_0 t) + \frac{A}{2} \sum_{m=1}^m a_m \left[ \sin(\omega_0 - \Delta\omega_m t - \phi_m) \right. \\
 &\quad \left. + \sin(\omega_0 + \Delta\omega_m t + \phi_m) \right].
 \end{aligned} \tag{A.4}$$

Equation (A.4) shows that the phase modulation with  $\phi_n(t)$  leads to two symmetrical sidebands. Knowing the power spectral density of a single sideband with respect to the carrier (single sideband phase noise), the coefficients of Rice's second model can be easily obtained.

### A.3 Phase Noise Cancellation Factor

Applying a sinusoidal signal with phase noise  $s_{\text{LO}} = \cos(\omega_0 t + \phi_n(t))$  and its delayed replica  $s_{\text{RF}} = \cos(\omega_0(t - \Delta T) + \phi_n(t - \Delta T))$  to a mixer leads to a frequency dependent modification of the phase noise spectrum. Modelling the mixer as an ideal multiplier together with a low pass filter gives the following output signal:

$$\begin{aligned}
 s_{\text{IF}} &\propto \cos(\omega_0 t + \phi_n(t) - \omega_0(t - \Delta T) - \phi_n(t - \Delta T)) \\
 &\propto \cos(\omega_0 \Delta T + \phi_n(t) - \phi_n(t - \Delta T))
 \end{aligned} \tag{A.5}$$

Neglecting the constant term, the instantaneous phase is

$$\begin{aligned}
 \phi_{\text{IF}}(t) &= \phi_n(t) - \phi_n(t - \Delta T) \\
 &= \phi_n(t) \star (\delta(t) - \delta(t - \Delta T)),
 \end{aligned} \tag{A.6}$$

where  $\delta(t)$  is the Dirac function. Hence, the transfer function of the mixer with respect to the phase noise is obtained as

$$H_n(\omega) = \frac{\Phi_{\text{IF}}(\omega)}{\Phi_n(\omega)} = 1 - e^{-j\omega \Delta T}, \tag{A.7}$$

which basically can be understood as a comb filter. Calculating the squared magnitude of the filter response finally gives the noise cancellation factor

$$\begin{aligned}
 |H_n(\omega)|^2 &= |1 - \cos(-\omega\Delta T) - \sin(-\omega\Delta T)|^2 & (A.8) \\
 &= |1 - \cos(\omega\Delta T) + j\sin(\omega\Delta T)|^2 \\
 &= 1 - 2\cos(\omega\Delta T) + \cos^2(\omega\Delta T) + \sin^2(\omega\Delta T) \\
 &= 2 - 2\cos(\omega\Delta T) \\
 &= 4\sin^2\left(\frac{\omega}{2} \cdot \Delta T\right) = 4 \cdot \sin^2(\pi f \Delta T).
 \end{aligned}$$

Regarding to (A.8) the phase noise spectral density at the output of the mixer is shaped according to the delay  $\Delta T$ . For small delays and/or a small offset frequency this effect leads to a significant reduction of the phase noise.

## A.4 Correlation Sequence and Matrix

All the considerations in this sections are made for the autocorrelation of a single signal, but are applicable to the crosscorrelation of two signals in a similar manner. The autocorrelation sequence  $r_{xx}(m)$  of a time discrete signal  $x(k)$  is obtained by calculating the expectation [17]

$$r_{xx}(m) = \mathcal{E} \{x(n+m)x^*(n)\} \quad (A.9)$$

and only depends on the time difference  $m$ . Hence, the following relation is true for negative time indices:

$$\begin{aligned}
 r_{xx}(-m) &= \mathcal{E} \{x(n-m)x^*(n)\} & (A.10) \\
 &= \mathcal{E} \{x(n)x^*(n+m)\} \\
 &= \mathcal{E} \{x(n+m)x^*(n)\}^* \\
 &= r_{xx}^*(m)
 \end{aligned}$$

In a similar way the  $p \times p$  autocorrelation matrix is defined by combining  $p$  subsequent samples into a signal vector  $\mathbf{x}(k) = [x(k+1) x(k+2) \dots x(k+p-1)]^T$ :

$$\mathbf{R}_{xx} = \mathcal{E} \left\{ \mathbf{x} \cdot \mathbf{x}^H \right\} = \begin{bmatrix} r_{xx}(0) & r_{xx}^*(1) & \dots & r_{xx}^*(p-1) \\ r_{xx}(1) & r_{xx}(0) & \dots & r_{xx}^*(p-2) \\ \vdots & \vdots & \ddots & \vdots \\ r_{xx}(p-1) & r_{xx}^*(p-2) & \dots & r_{xx}(0) \end{bmatrix} \quad (A.11)$$

The autocorrelation matrix is a hermitian Toeplitz matrix, which enables a computationally efficient inversion using the Levinson-Durbin recursion [17]. In practical applications only a limited set of samples of the signal  $x(k)$  is known. Hence, the correlation sequence or the correlation matrix have to be estimated. With  $N$  being the number of known samples, a straight forward estimate of the positive autocorrelation lags is

$$\hat{r}_{xx}(m) = \frac{1}{N-m} \sum_{n=0}^{N-m-1} x(n+m) \cdot x^*(n). \quad (\text{A.12})$$

The negative index lags are the complex conjugate as shown before. Overall,  $2N - 1$  correlation lags are obtained out of  $N$  known samples. This kind of estimation is unbiased as the expectation value  $\mathcal{E} \{ \hat{r}_{xx}(m) \} = r_{xx}(m)$ . However, the statistical uncertainty increases for higher lag indices  $m$ , as there are fewer summation terms in (A.12). To reduce the influence of the higher index lags the following estimator is used in many applications:

$$\hat{r}_{xx}(m) = \begin{cases} \frac{1}{N} \sum_{n=0}^{N-m-1} x(n+m) x^*(n) & \text{for } 0 \leq m \leq N-1 \\ \frac{1}{N} \sum_{n=0}^{N-|m|-1} x^*(n+m) x^*(n) & \text{for } -(N-1) \leq m < 0 \end{cases} \quad (\text{A.13})$$

Basically, the estimator in (A.13) is obtained by multiplying (A.12) with a triangular window, which leads to a biased estimate. For large numbers  $N$  the bias tends to zero, which makes the estimator asymptotically unbiased.

In literature [17] several possibilities are discussed to estimate the  $p \times p$  correlation matrix out of  $N$  samples. Four of them can be summarised using the so-called data matrix

$$\mathbf{X}_p = \begin{bmatrix} x(1) & \dots & 0 \\ \vdots & \ddots & \vdots \\ x(p) & & 0 \\ \hline x(p+1) & & x(1) \\ \vdots & \ddots & \vdots \\ x(N) & & x(N-p) \\ \hline 0 & & x(N-p+1) \\ \vdots & \ddots & \vdots \\ 0 & \dots & x(N) \end{bmatrix} = \begin{bmatrix} \mathbf{L}_p \\ \mathbf{T}_p \\ \mathbf{U}_p \end{bmatrix}, \quad (\text{A.14})$$

in which the rows contain the shifted data values. Unavailable data are set to zero, which implies a windowing of the data. The following definitions of correlation matrix estimates can be derived from the data matrix:

$$\hat{\mathbf{R}}_{xx} = \begin{cases} \mathbf{X}_p^H \mathbf{X}_p, & \text{windowed (autocorrelation) case} \\ \mathbf{T}_p^H \mathbf{T}_p, & \text{non-windowed (covariance) case} \\ \begin{bmatrix} \mathbf{L}_p \\ \mathbf{T}_p \end{bmatrix}^H \begin{bmatrix} \mathbf{L}_p \\ \mathbf{T}_p \end{bmatrix} & \text{prewindowed case} \\ \begin{bmatrix} \mathbf{T}_p \\ \mathbf{U}_p \end{bmatrix}^H \begin{bmatrix} \mathbf{T}_p \\ \mathbf{U}_p \end{bmatrix} & \text{postwindowed case} \\ \begin{bmatrix} \mathbf{T}_p \\ \mathbf{T}_p^* \mathbf{J} \end{bmatrix}^H \begin{bmatrix} \mathbf{T}_p \\ \mathbf{T}_p^* \mathbf{J} \end{bmatrix} & \text{modified covariance case,} \end{cases} \quad (\text{A.15})$$

where the terms “autocorrelation” and “covariance” are chosen for historical reasons and do not refer to the different definition used in statistics (considering or not considering the mean value of the data). The matrix  $\mathbf{J}$  in the definition of the modified covariance case is a reflection matrix only containing ones on the secondary diagonal. Hence,  $\mathbf{T}_p^* \mathbf{J}$  is the mirrored, complex conjugate of  $\mathbf{T}$ . As a consequence the coefficients of the estimated correlation matrix are obtained as

$$\hat{r}_{xx}(i,j) = \sum_{n=p+1}^N [x^*(n-i)x(n-j) + x(n-p+i)x^*(n-p+j)] . \quad (\text{A.16})$$

which is equivalent to an averaging of the positive correlation lags and the complex conjugate negative lags obtained by the non-windowed method in (A.15).



## Bibliography

- [1] HÜLSMEYER, CHRISTIAN: *Verfahren zur Bestimmung der Entfernung von metallischen Gegenständen (Schiffen o. dgl.), deren Gegenwart durch das Verfahren nach Patent 165546 festgestellt wird.* DE169154, 1904.
- [2] MENZEL, W.: *50 Years of Millimeter-Waves: A Journey of Development.* Microwave Journal, 51(8), 2008.
- [3] NIENHAUS, K., R. WINKEL, W. MAYER, A. GRONAU and W. MENZEL: *An Experimental Study on Using Electronically Scanning Microwave Radar Systems on Surface Mining Machines.* In *Proc. IEEE Radar Conference*, pages 509–512, 2007.
- [4] BARBARESCO, F., A. JEANTET and U. MEIER: *Wake vortex X-band radar monitoring: Paris-CDG Airport 2008 campaign results; perspectives.* International Radar Conference (RADAR) – Surveillance for a Safer World, pages 1–6, Oct. 2009.
- [5] HALLDORSSON, THORSTEINN and VOLKER ZIEGLER: *Bordgestütztes Wirbelschleppen-Erkennungssystem (BoWES) – Schlussbericht zum Technologievorhaben.* Technical Report, BMBF, Förderkennzeichen 20A0301B, 2005.
- [6] MARSHALL, R.E. and T.J. MYERS: *Wingtip generated wake vortices as radar targets.* In *Proceedings of the 1996 IEEE National Radar Conference*, pages 184–189, May 1996.
- [7] BEASLEY, P. D. L., G. BINNS, R. D. HODGES and R. J. BADLEY: *Tarsier, a millimetre wave radar for airport runway debris detection.* In *Proc. First European Radar Conference (EURAD)*, pages 261–264, 2004.
- [8] MAYER, W., A. GRONAU, W. MENZEL and H. LEIER: *A Compact 24 GHz Sensor for Beam-Forming and Imaging.* In *Proc. 9th International Conference on Control, Automation, Robotics and Vision, ICARCV '06*, pages 1–6, 2006.

- [9] ASANO, Y., S. OHSHIMA, T. HARADA, M. OGAWA and K. NISHIKAWA: *Proposal of millimeter-wave holographic radar with antenna switching*. In *Proc. IEEE MTT-S International Microwave Symposium Digest*, volume 2, pages 1111–1114, 2001.
- [10] LEE, MOON-SIK and YONG-HOON KIM: *Design and Performance of a 24-GHz Switch-Antenna Array FMCW Radar System for Automotive Applications*. *IEEE Transactions on Vehicular Technology*, 59(5):2290–2297, Jun 2010.
- [11] LUDLOFF, ALBRECHT K.: *Handbuch Radar und Radarsignalverarbeitung*. Vieweg Verlag, 2002.
- [12] SKOLNIK, MERRILL IVAN: *Introduction to Radar Systems*. Mcgraw-Hill College, 1980.
- [13] STURM, C., E. PANCERA, T. ZWICK and W. WIESBECK: *A novel approach to OFDM radar processing*. In *IEEE Radar Conference*, pages 1–4, May 2009.
- [14] STURM, C., T. ZWICK, W. WIESBECK and M. BRAUN: *Performance verification of symbol-based OFDM radar processing*. In *IEEE Radar Conference, 2010*, pages 60–63, May 2010.
- [15] DETLEFSEN, J., A. DALLINGER, S. SCHELKSHORN and S. BERTL: *UWB Millimeter-Wave FMCW Radar using Hilbert Transform Methods*. In *Proc. IEEE Ninth International Symposium on Spread Spectrum Techniques and Applications*, pages 46–48, 2006.
- [16] HAUSCHILD, T. and R. KNOCHEL: *Calibration of short range FMCW-radars with network analyzer calibration techniques*. In *Proc. International Microwave Symposium Digest, IEEE MTT-S*, volume 2, pages 969–972, 1998.
- [17] MARPLE, S. LAWRENCE: *Digital Spectral Analysis: With Applications (Prentice Hall Signal Processing Series)*. Prentice Hall, 1987.
- [18] KAMMEYER, KARL DIRK, KRISTIAN KROSCHER, DIETER BOSS and ARMIN DEKORSKY: *Digitale Signalverarbeitung. Filterung und Spektralanalyse mit MATLAB-Übungen*. Teubner Verlag, 1998.
- [19] POULARIKAS, ALEXANDER D.: *Handbook of Formulas and Tables for Signal Processing (Electrical Engineering Handbook)*. CRC Press, 1998.

- 
- [20] MEYER, MARTIN: *Signalverarbeitung*. Vieweg Verlag, 2003.
- [21] VASEGHI, SAEED V.: *Advanced Signal Processing and Noise Reduction, 2nd Edition*. Wiley, 2000.
- [22] GECK, B., J. MARQUARDT and M. SAGEBIEL: *A homodyne network analyzer based on the FMCW method and digital signal processing*. In *Conference on Precision Electromagnetic Measurements Digest, 1996*, pages 530–531, 17-20 1996.
- [23] FEIL, PETER: *Kalibration einer Radareinheit mit gerätespezifischen Korrekturkurven*. Offenlegungsschriften DE 10 2008 050 117 A1, US 0 2011 018 1458 A1, 2008–2011.
- [24] OPPENHEIM, ALAN V., RONALD W. SCHAFER and JOHN R. BUCK: *Discrete-time Signal Processing*. Prentice Hall International Editions, 1999.
- [25] ROHLING, H. and M.-M. MEINECKE: *Waveform design principles for automotive radar systems*. In *Proc. CIE International Conference on Radar*, pages 1–4, 2001.
- [26] MEINECKE, MARC-MICHAEL, MARIAN ANDRZEJ OBOJSKI and JORN KNAUP: *Increasing vehicular safety at intersections by using LFMSK modulated radar sensors*. In *11th International Radar Symposium (IRS)*, pages 1–4, 2010.
- [27] WIRTH, WULF-DIETER: *Radar Techniques Using Array Antennas (FEE radar, sonar, navigation & avionics series)*. The Institution of Engineering and Technology, 2001.
- [28] KRIM, H. and M. VIBERG: *Two decades of array signal processing research: the parametric approach*. *IEEE Signal Processing Magazine*, 13(4):67–94, 1996.
- [29] SCHMIDT, R.: *Multiple emitter location and signal parameter estimation*. *IEEE Transactions on Antennas and Propagation*, 34(3):276–280, 1986.
- [30] ROY, R., A. PAULRAJ and T. KAILATH: *ESPRIT – A subspace rotation approach to estimation of parameters of cisoids in noise*. *IEEE Transactions on Acoustics, Speech and Signal Processing*, 34(5):1340–1342, 1986.
- [31] CAPON, J.: *High-resolution frequency-wavenumber spectrum analysis*. *Proceedings of the IEEE*, 57(8):1408–1418, 1969.



- [32] LI, JIAN and PETRE STOICA: *Robust Adaptive Beamforming (Wiley Series in Telecommunications and Signal Processing)*. Wiley-Interscience, 2005.
- [33] LI, J. and P. STOICA: *Versatile robust Capon beamforming: theory and applications*. In *Proc. Sensor Array and Multichannel Signal Processing Workshop*, pages 38–42, 2004.
- [34] LI, JIAN, P. STOICA and ZHISONG WANG: *On robust Capon beamforming and diagonal loading*. *IEEE Transactions on Signal Processing*, 51(7):1702–1715, 2003.
- [35] STOICA, P., ZHISONG WANG and JIAN LI: *Robust Capon beamforming*. *IEEE Signal Processing Letters*, 10(6):172–175, 2003.
- [36] LORENZ, R. G. and S. P. BOYD: *Robust minimum variance beamforming*. *IEEE Transactions on Signal Processing*, 53(5):1684–1696, 2005.
- [37] JOHNSON, D. and S. DEGRAAF: *Improving the resolution of bearing in passive sonar arrays by eigenvalue analysis*. *IEEE Transactions on Acoustics, Speech and Signal Processing*, 30(4):638–647, Aug 1982.
- [38] PAULRAJ, A., R. ROY and T. KAILATH: *Estimation Of Signal Parameters Via Rotational Invariance Techniques – Esprit*. In *Nineteenth Asilomar Conference on Circuits, Systems and Computers*, pages 83–89, 6-8 1985.
- [39] VAN VEEN, B.D. and K.M. BUCKLEY: *Beamforming: a versatile approach to spatial filtering*. *IEEE ASSP Magazine*, 5(2):4–24, april 1988.
- [40] ANALOG DEVICES: *RF PLL Frequency Synthesizers ADF4110 / ADF4111 / ADF4112 / ADF4113*. Datasheet Rev. C.
- [41] UNITED MONOLITHIC SEMICONDUCTORS: *CHV2270 – Fully Integrated Ku-band HBT VCO*. Datasheet.
- [42] UNITED MONOLITHIC SEMICONDUCTORS: *CHU3377 – W-band Multifunction: Multiplier/MPA*. Datasheet.
- [43] UNITED MONOLITHIC SEMICONDUCTORS: *CHM2378a – W-band Dual Channel Mixer*. Datasheet.
- [44] TACONIC ADVANCED DIELECTRIC DIVISION: *A New Low Loss, Laser Ablatable Substrate for Microwave Circuitry*. *Microwave Journal*, 47(7):104–110, 2004.

- 
- [45] VILLEGAS, F. J., D. I. STONES and H. A. HUNG: *A novel waveguide-to-microstrip transition for millimeter-wave module applications*. IEEE Transactions on Microwave Theory and Techniques, 47(1):48–55, 1999.
- [46] GRABHERR, W., W. G. B. HUDER and W. MENZEL: *Microstrip to waveguide transition compatible with MM-wave integrated circuits*. IEEE Transactions on Microwave Theory and Techniques, 42(9):1842–1843, 1994.
- [47] FEIL, P. and F. BAUER: *Two Right-Angle Microstrip to Waveguide Transitions Suitable for Metal Backed Substrates*. In *Proc. International Conference on Electromagnetics in Advanced Applications*, 2010.
- [48] WU, KE, D. DESLANDES and Y. CASSIVI: *The substrate integrated circuits – a new concept for high-frequency electronics and optoelectronics*. In *Proc. 6th International Conference on Telecommunications in Modern Satellite, Cable and Broadcasting Service TELSIKS*, volume 1, pages 3–10, 2003.
- [49] MENZEL, WOLFGANG and JAN MACHAC: *Shunt Post Loaded Waveguide Junctions and their Applications to a Novel Type of Bandpass Filter*. Journal of Electrical Engineering, 46:142–146, 1995.
- [50] MEINKE, H. H. and F. W. GUNDLACH: *Taschenbuch der Hochfrequenztechnik: Grundlagen, Band 1*. Springer-Verlag, 1992.
- [51] AGILENT: *Advanced Design System*. <http://www.agilent.com/find/eesof-ads>.
- [52] FEDERAL COMMUNICATIONS COMMISSION: *FCC 05-45 – Allocations and Service Rules for the 71–76 GHz, 81–86 GHz, and 92–95 GHz Bands*.
- [53] WINKLER, V.: *Novel Waveform Generation Principle for short-range FMCW-Radars*. German Microwave Conference, pages 1–4, 16-18 2009.
- [54] MAYER, W., M. MEILCHEN, W. GRABHERR, P. NÜCHTER and R. GUHL: *Eight-channel 77 GHz front-end module with high-performance synthesized signal generator for FM-CW sensor applications*. IEEE Transactions on Microwave Theory and Techniques, 52(3):993–1000, 2004.
- [55] ANALOG DEVICES: *A Technical Tutorial on Digital Signal Synthesis*. Application Note, 1999.
- [56] KROUPA, V. F.: *Phase and amplitude disturbances in direct digital frequency synthesizers*. IEEE Transactions on Ultrasonics, Ferroelectrics, and Frequency Control, 46(3):481–486, 1999.



- [57] KROUPA, V. F., V. CIZEK, J. STURSA and H. SVANDOVA: *Spurious signals in direct digital frequency synthesizers due to the phase truncation*. IEEE Transactions on Ultrasonics, Ferroelectrics, and Frequency Control, 47(5):1166–1172, 2000.
- [58] ANALOG DEVICES: *Phase-Locked Loops for High-Frequency Receivers and Transmitters*. Application Note, 1999.
- [59] WENKE, CLAUDIA: *Untersuchungen an einem mehrkanaligen 77 GHz-Radarmodul*. Diplomarbeit, Universität Ulm, 2005.
- [60] STOVE, A. G.: *Linear FMCW radar techniques*. IEE Proceedings-F, Radar and Signal Processing, 139(5):343–350, 1992.
- [61] LINEAR TECHNOLOGY: *LTSpice III*. <http://www.linear.com/designtools/software/>.
- [62] MAYER, WINFRIED: *Abbildender Radarsensor mit sendeseitig geschalteter Gruppenantenne*. Dissertation, Universität Ulm, 2008.
- [63] MATHWORKS: *Matlab R2010a*. <http://www.mathworks.de/products/matlab>.
- [64] M/A-COM: *MA4GC6773–77 GHz GaAs SP2T PIN Diode Switch*. Datasheet v2.00.
- [65] FEIL, PETER, SABINE DIETER, WINFRIED MAYER, WOLFGANG MENZEL and REIK WINKEL: *Erkennung von aktiven Radarzielen*. Patentanmeldung beim deutschen Patentamt, 2010.
- [66] SAITO, T., N. OKUBO, Y. KAWASAKI, O. ISAJI and H. SUZUKI: *An FM-CW radar module with front-end switching heterodyne receiver*. In *International Microwave Symposium Digest, IEEE MTT-S*, pages 713–716 vol.2, 1-5 1992.
- [67] FEIL, PETER and WINFRIED MAYER: *Empfangsmischer zur Verringerung von Überkopplungseffekten*. Offenlegungsschrift DE 10 2008 050 327 A1.
- [68] FEIL, P. and T. CHALOUN: *Active Switched Antenna Array for 77 GHz Digital Beamforming Radar*. In *Proc. 5th European Conference on Antennas and Propagation*, 2011.
- [69] HITTITE: *HMC-AUH320 – GaAs HEMT MMIC MEDIUM POWER AMPLIFIER, 71–86 GHz*. Datasheet v02.0408.

- 
- [70] KEES, N., E. SCHMIDHAMMER and J. ; DETLEFSEN: *Improvement of angular resolution of a millimeterwave imaging system by transmitter location multiplexing*. In *IEEE MTT-S International Microwave Symposium Digest*, 1995.
- [71] COMPUTER SIMULATION TECHNOLOGY: *CST Microwave Studio*. <http://www.cst.com>.
- [72] STEHLE, A., G. GEORGIEV, V. ZIEGLER, B. SCHOENLINNER, U. PRECHTEL, H. SEIDEL and U. SCHMID: *RF-MEMS Switch and Phase Shifter Optimized for W-Band*. In *Proc. 38th European Microwave Conference*, 2008.
- [73] GAUTIER, W., V. ZIEGLER, A. STEHLE, B. SCHOENLINNER, U. PRECHTEL and W. MENZEL: *RF-MEMS phased array antenna on low-loss LTCC substrate for Ka-band data link*. In *Proc. European Microwave Conference, EuMC 2009*, pages 914–917, 2009.
- [74] LINEBARGER, D.A.: *A fast method for computing the coarray of sparse linear arrays*. *IEEE Transactions on Antennas and Propagation*, 40:1109–1112, 1992.
- [75] LEE, MOON-SIK, V. KATKOVNIK and YONG-HOON KIM: *System modeling and signal processing for a switch antenna array radar*. *IEEE Transactions on Signal Processing*, 52(6):1513–1523, 2004.
- [76] YANG, LI, LIANG LIWAN, PAN WEIFENG, CHEN YAQIN and FENG ZHENGHE: *Signal processing method for switch antenna array of the FMCW radars*. In *Proc. IEEE Radar Conference*, pages 289–293, 2001.
- [77] FEIL, PETER: *Optimierung der Schaltreihenfolge bei geschalteten Antennenarrays*. Offenlegungsschrift DE 10 2009 027 003 A1.
- [78] FEIL, PETER: *Überwachung einer produktions- oder fördertechnischen Umgebung mittels Radar*. Patentanmeldung beim deutschen Patentamt, 2010.
- [79] CAMIADE, M., D. DOMNESQUE, Z. OUARCH and A. SION: *Fully MMIC-Based Front End for FMCW Automotive Radar at 77 GHz*. In *Proc. 30th European Microwave Conference*, 2000.
- [80] GOURDON, C., R. SEVIN, D. DOMNESQUE and M. CAMIADE: *A High Linearity, Low Phase Noise and High Operating Temperature Ku-band MMIC VCO-Prescaler, suitable for Complex Modulations ACC radar source*. In *Proc. 36th European Microwave Conference, EuMC*, 2006.

- [81] VENOT, Y. and W. WIESBECK: *Multipurpose 76,5 GHz Near Field Radar Sensor*. In *Proc. 31st European Microwave Conference*, 2001.
- [82] STRATECH SYSTEMS LIMITED: *iFerret, Intelligent Airfield/Runway Surveillance and FOD Detection Systems*. [http://www.stratechsystems.com/iv\\_iferret.asp](http://www.stratechsystems.com/iv_iferret.asp).
- [83] LASER OPTRONIX: *Airport related applications for electro optical sensors*. <http://www.laseroptronix.se/airpor/airport.html>.
- [84] NAVTECH RADAR LTD.: *Airport Surface Movement*. <http://www.navtechradar.com/Runway%20Surveillance.htm>.
- [85] XSIGHT SYSTEMS: *FODetect, Automated Foreign Object Debris Detection System*. <http://www.xsightsys.com/index.aspx?id=3287>.
- [86] FEIL, P., W. MENZEL, T. P. NGUYEN, C. PICHOT and C. MIGLIACCIO: *Foreign objects debris detection (FOD) on airport runways using a broadband 78 GHz sensor*. In *Proc. European Radar Conference EuRAD 2008*, pages 451–454, 2008.
- [87] FEIL, P., A. ZEITLER, T.P. NGUYEN, CH. PICHOT, C. MIGLIACCIO and W. MENZEL: *Foreign Object Debris Detection Using a 78 GHz Sensor with Cosec Antenna*. In *Proc. European Radar Conference EuRAD*, 2010.
- [88] MENZEL, W., D. PILZ and M. AL-TIKRITI: *Millimeter-wave folded reflector antennas with high gain, low loss, and low profile*. *IEEE Antennas and Propagation Magazine*, 44(3):24–29, Jun 2002.
- [89] PILZ, D. and W. MENZEL: *Printed MM-wave folded reflector antennas with high gain, low loss, and low profile*. In *Antennas and Propagation Society International Symposium, 2000. IEEE*, volume 2, pages 790–793, 2000.
- [90] ZEITLER, A., J. LANTERI, C. PICHOT, C. MIGLIACCIO, P. FEIL and W. MENZEL: *Folded Reflectarrays With Shaped Beam Pattern for Foreign Object Debris Detection on Runways*. *IEEE Transactions on Antennas and Propagation*, 58(99):3065, 2010.
- [91] LANTERI, J., A. ZEITLER, J. Y. DAUVIGNAC, C. PICHOT, C. MIGLIACCIO, P. FEIL and W. MENZEL: *Investigation of wideband millimetre-wave reflectarrays for radar applications operating in the W Band*. In *Proc. 3rd European Conference on Antennas and Propagation EuCAP*, pages 826–830, 2009.

- 
- [92] ROHLING, H.: *Radar CFAR Thresholding in Clutter and Multiple Target Situations*. IEEE Transactions on Aerospace and Electronic Systems, AES-19(4):608–621, 1983.
- [93] WINKLER, V.: *Range Doppler detection for automotive FMCW radars*. In *Proc. European Microwave Conference*, pages 1445–1448, 9–12 2007.
- [94] SCHNEIDER, ROBERT: *Wellenausbreitung für ein bildgebendes Radar zur Erfassung von Verkehrsszenen*. Dissertation, Universität Karlsruhe, 1998.
- [95] MOREIRA, ALBERTO: *Radar mit synthetischer Apertur*. Habilitationsschrift, Universität Karlsruhe, 2000.
- [96] KLAUSING, HELMUT and WOLFGANG HOLPP: *Radar mit realer und synthetischer Apertur. Konzeption und Realisierung*. Oldenbourg, 1999.
- [97] FEIL, P., T. KRAUS and W. MENZEL: *Short Range mm-Wave SAR for Surveillance and Security Applications*. In *Proc. 8th European Conference on Synthetic Aperture Radar*, 2010.
- [98] CUMMING, I.G. and F.H. WONG: *Digital Processing of Synthetic Aperture Radar Data*. Artech House Publishers, January 2005.
- [99] DIETER, S., C. FISCHER and W. MENZEL: *Design of a folded reflectarray antenna using Particle Swarm Optimization*. In *Proc. European Microwave Conference*, 2010.
- [100] WIKIPEDIA: *Sinkhole*. <http://en.wikipedia.org/wiki/Sinkhole>.
- [101] ANDRES, M., P. FEIL, W. MENZEL, H.-L. BLOECHER and J. DICKMANN: *Analysis of automobile scattering center locations by SAR measurements*. In *IEEE Radar Conference (RADAR)*, 2011.
- [102] ANDRES, M., P. FEIL and W. MENZEL: *3D-Scattering Center Detection of Automotive Targets Using 77 GHz UWB Radar Sensors*. In *Proc. European Conference on Antennas and Propagation, EuCAP*, 2012.
- [103] SANGHA, G. S. and M. H. W. HOFFMANN: *Analysis and design of a frequency synthesizer with internal and external noise sources*. In *Proceedings of 18th International Conference on Noise and Fluctuations*, 2005.
- [104] STEPHENS, DONALD R.: *Phase-Locked Loops for Wireless Communications: Digital, Analog and Optical Implementations*. Springer, 2001.

- [105] ASANO, YOSHIKAZU: *Millimeter-Wave Holographic Radar for Automotive Applications*. Technical Report, TOYOTA Central Research and Development Laboratories Inc., 2000.
- [106] BUOLI, CARLO, VITO MARCO GADALETA, TOMMASO TURILLO and ALESSANDRO ZINGIRIAN: *A broadband microstrip to waveguide transition for FR4 multilayer PCBs up to 50 GHz*. In *Proc. 32nd European Microwave Conference*, pages 1–4, 2002.
- [107] CAPON, J., R. J. GREENFIELD and R. J. KOLKER: *Multidimensional maximum-likelihood processing of a large aperture seismic array*. *Proceedings of the IEEE*, 55(2):192–211, 1967.
- [108] DAS, B. N., K. V. S. V. R. PRASAD and K. V. S. RAO: *Excitation of Waveguide by Stripline- and Microstrip-Line-Fed Slots*. *IEEE Transactions on Microwave Theory and Techniques*, 34(3):321–327, 1986.
- [109] GRESHAM, I., N. JAIN, T. BUDKA, A. ALEXANIAN, N. KINAYMAN, B. ZIEGNER, S. BROWN and P. STAECKER: *A compact manufacturable 76–77 GHz radar module for commercial ACC applications*. *IEEE Transactions on Microwave Theory and Techniques*, 49(1):44–58, Jan 2001.
- [110] GRESHAM, I., A. JENKINS, R. EGRI, C. ESWARAPPA, N. KINAYMAN, N. JAIN, R. ANDERSON, F. KOLAK, R. WOHLERT, S.P. BAWELL, J. BENNETT and J.-P. LANTERI: *Ultra-wideband radar sensors for short-range vehicular applications*. *IEEE Transactions on Microwave Theory and Techniques*, 52(9):2105–2122, Sept. 2004.
- [111] GRESHAM, I., A. JENKINS, N. KINAYMAN, R. POINT, YUMIN LU, R. ITO and A. STREET: *Si Based UWB Radar Sensors*. *IEEE Radar Conference*, 2007, pages 658–663, 2007.
- [112] HALL, LEONARD T., HEDLEY J. HANSEN and DEREK ABBOTT: *Rotman lens for mm-wavelengths*. In *Proceedings of SPIE*, volume 4935, pages 215–221, 2002.
- [113] HEUVEN, J. H. C. VAN: *A New Integrated Waveguide-Microstrip Transition (Short Papers)*. *IEEE Transactions on Microwave Theory and Techniques*, 24(3):144–147, 1976.
- [114] JAIN, N. and N. KINAYMAN: *A novel microstrip mode to waveguide mode transformer and its applications*. In *Proc. International Microwave Symposium Digest, IEEE MTT-S*, volume 2, pages 623–626 vol.2, 2001.

- 
- [115] KATKOVNIK, V., M. S. LEE and Y. H. KIM: *High-resolution signal processing for a switch antenna array FMCW radar with a single channel receiver*. In *Proc. Sensor Array and Multichannel Signal Processing Workshop*, pages 543–547, 2002.
- [116] KOLAK, F. and C. ESWARAPPA: *A low profile 77 GHz three beam antenna for automotive radar*. In *Proc. International Microwave Symposium Digest, IEEE MTT-S*, volume 2, pages 1107–1110, 2001.
- [117] KOMAROV, I.V. and S.M. SMOLSKIY: *Fundamentals of short-range FM radar*. Artech House Radar Library. Artech House, 2003.
- [118] KROUPA, V. F.: *Phase and amplitude disturbances in direct digital frequency synthesizers*. In *Proc. IEEE International Frequency Control Symposium*, pages 975–979, 1997.
- [119] KROUPA, V. F., V. CIZEK, J. STURSA and H. SVANDOVA: *Spurious signals in direct digital frequency synthesizers due to the phase truncation*. In *Proc. Joint Meeting of the European Frequency and Time Forum and the IEEE International Frequency Control Symposium*, volume 2, pages 1138–1141, 1999.
- [120] LI, ZHAOLONG and KE WU: *24 GHz FMCW Radar Front-End System on Substrate*. In *Proc. IEEE Radio and Wireless Symposium*, pages 233–236, 2007.
- [121] LORENZ, R. G. and S. P. BOYD: *Robust minimum variance beamforming*. In *Conference Record of the Thirty-Seventh Asilomar Conference on Signals, Systems and Computers*, volume 2, pages 1345–1352, 2003.
- [122] MENZEL, WOLFGANG and JAN MACHAC: *Waveguide bandpass filters with attenuation of higher-order passbands*. In *Proc. 23rd European Microwave Conference*, pages 606–607, 1993.
- [123] MENZEL, W., D. PILZ and R. LEBERER: *A 77-GHz FM/CW radar front-end with a low-profile low-loss printed antenna*. *IEEE Transactions on Microwave Theory and Techniques*, 47(12):2237–2241, Dec. 1999.
- [124] META, A., P. HOOGEBOOM and L.P. LIGTHART: *Signal Processing for FMCW SAR*. *IEEE Transactions on Geoscience and Remote Sensing*, 45(11):3519–3532, Nov. 2007.
- [125] METZ, CARSTEN, ERNST LISSEL and ARNE F. JACOB: *Planar Multiresolutional Antenna for Automotive Radar*. In *Proc. 31st European Microwave Conference*, pages 1–4, 2001.



- [126] METZ, C., L. C. STANGE, A. F. JACOB and E. LISSEL: *Performance of thinned antenna arrays using nonlinear processing in DBF radar applications*. In *Proc. International Microwave Symposium Digest IEEE MTT-S*, volume 1, pages 275–278, 2001.
- [127] NAM, HEE, TAE-SOON YUN, KI-BYOUNG KIM, KI-CHEOL YOON and JONG-CHUL LEE: *Ku-band transition between microstrip and substrate integrated waveguide (SIW)*. In *Proc. Asia-Pacific Microwave Conference, APMC 2005*, volume 1, page 4, 2005.
- [128] PAULRAJ, A., R. ROY and T. KAILATH: *A subspace rotation approach to signal parameter estimation*. *Proceedings of the IEEE*, 74(7):1044–1046, 1986.
- [129] ROY, R., A. PAULRAJ and T. KAILATH: *Direction-of-arrival estimation by subspace rotation methods – ESPRIT*. In *Proc. IEEE International Conference on ICASSP '86. Acoustics, Speech, and Signal Processing*, volume 11, pages 2495–2498, 1986.
- [130] SCHOENLINNER, B., XIDONG WU, J. P. EBLING, G. V. ELEFTHERI-  
ADES and G. M. REBEIZ: *Wide-scan spherical-lens antennas for auto-  
motive radars*. *IEEE Transactions on Microwave Theory and Techniques*, 50(9):2166–2175, 2002.
- [131] SHARIFF, KARIM and ALAN WRAY: *Analysis of the radar reflectivity of  
aircraft vortex wakes*. *Journal of Fluid Mechanics*, 463:121–161, 2002.
- [132] STOLLE, REINHARD and BURKHARD SCHIEK: *Precision ranging by phase  
processing of scalar homodyne FMCW raw data*. In *Microwave Conference.  
26th European*, volume 1, pages 143 –146, 6-13 1996.
- [133] STOVE, A. G.: *Modern FMCW radar – techniques and applications*. In  
*Proc. First European Radar Conference, EURAD*, pages 149–152, 2004.
- [134] STROHM, K. M., H. L. BLOECHER, R. SCHNEIDER and J. WENGER: *Deve-  
lopment of future short range radar technology*. In *Proc. European Radar  
Conference, EURAD*, pages 165–168, 2005.
- [135] SWINGLER, D., R. WALKER and G. LEWIS: *Linear prediction for aper-  
ture extrapolation in line array beamforming*. In *Proc. IEEE International  
Conference on Acoustics, Speech, and Signal Processing, ICASSP '86*, vol-  
ume 11, pages 2519–2522, 1986.

- 
- [136] SWINGLER, D. N. and R. S. WALKER: *Line-array beamforming using linear prediction for aperture interpolation and extrapolation*. IEEE Transactions on Acoustics, Speech and Signal Processing, 37(1):16–30, 1989.
- [137] TREES, HARRY L. VAN: *Optimum Array Processing (Detection, Estimation, and Modulation Theory, Part IV)*. Wiley-Interscience, 2002.
- [138] VOSSIEK, M. and P. GULDEN: *The Switched Injection-Locked Oscillator: A Novel Versatile Concept for Wireless Transponder and Localization Systems*. IEEE Transactions on Microwave Theory and Techniques, 56(4):859–866, 2008.
- [139] VOSSIEK, M., T. v. KERSENBRÖCK and P. HEIDE: *Signal Processing Methods for Millimetrewave FMCW Radar with High Distance and Doppler Resolution*. In *Proc. 27th European Microwave Conference, 1997*, volume 2, pages 1127–1132, 8–12 1997.
- [140] WEHRLI, S., D. BARRAS, F. ELLINGER and H. JACKEL: *Integrated Active Pulsed Reflector for FMCW Radar Localization*. In *International Microwave Symposium Digest, IEEE MTT-S*, pages 81–84, 2009.
- [141] WEHRLI, S., R. GIERLICH, J. HUTTNER, D. BARRAS, F. ELLINGER and H. JACKEL: *Integrated Active Pulsed Reflector for an Indoor Local Positioning System*. IEEE Transactions on Microwave Theory and Techniques, 58(2):267–276, 2010.
- [142] ANDRES, MARKUS, PETER FEIL, WOLFGANG MENZEL, HANS-LUDWIG BLOECHER and JÜRGEN DICKMANN: *3D-Detection of Automobile Scattering Centers using UWB Radar Sensors at 24/77 GHz*. accepted for publication in the IEEE AESS Magazine.
- [143] FEIL, PETER: *Abgewinkelter Übergang von Mikrostreifenleitung auf Rechteckhohlleiter*. Deutsches Patent DE 10 2008 026 579, April 2010.
- [144] FEIL, PETER, WINFRIED MAYER, THOMAS KRAUS, CLAIRE MIGLIACCIO and WOLFGANG MENZEL: *Industrial and Security Applications of Imaging Millimeter Wave Sensors*. tm - Technisches Messen, 77(7-8):373–380, August 2010.
- [145] FEIL, P., W. MAYER and W. MENZEL: *A 77 GHz eight-channel shaped beam planar reflector antenna*. In *Proc. 3rd European Conference on Antennas and Propagation, EuCAP*, pages 1320–1323, 2009.

- [146] FEIL, P., W. MAYER and W. MENZEL: *Various cross-range resolution techniques applied to an eight-channel 77 GHz sensor*. In *Proc. European Radar Conference, EuRAD*, pages 59–62, 2007.
- [147] FEIL, P., C. MIGLIACCIO, T. KRAUS and W. MENZEL: *Short Range mm-Wave Imaging and Applications*. In *ITG Topical Meeting "New Materials and Non-Destructive Testing"*, 2009.
- [148] GOPPELT, MARKUS, PETER FEIL and WINFRIED MAYER: *Digital-Beam-Forming Extension for a 2-Channel E-Band FMCW-Sensor*. accepted for publication in the International Journal of Microwave and Wireless Technologies.
- [149] MENZEL, W. and P. FEIL: *Ultra-Wideband (UWB) Filter With WLAN Notch*. In *Proc. 36th European Microwave Conference*, pages 595–598, 2006.
- [150] MULTARI, M., J. LANTERI, J. L. LE SONN, L. BROCHIER, C. PICHOT, C. MIGLIACCIO, J. L. DESVILLES and P. FEIL: *77 GHz Stepped Lens With Sectorial Radiation Pattern as Primary Feed of a Lens Based CATR*. *IEEE Transactions on Antennas and Propagation*, 58(1):207–211, 2010.
- [151] NGUYEN, T.P., C. MIGLIACCIO, C PICHOT, W. MENZEL and P. FEIL: *Étude d'une antenne en cosécante carrée pour la détection de débris sur pistes d'aéroport*. In *16èmes Journées Nationales Microondes*, 2009.
- [152] ZEITLER, A., T.P. NGUYEN, P. FEIL and C. MIGLIACCIO: *Antennes Réseaux Reflecteurs en Cosecante Carrée Pour Application FOD dans la Bande 76–81 GHz*. In *GDR ONDES*, 2009.



